University of Southampton

Active Control of Low Frequency Buzz-Saw Tones

Matthew Jon Wilkinson

A thesis submitted for the award of Doctor of Philosophy

Institute of Sound and Vibration Research

October 2004

UNIVERSITY OF SOUTHAMPTON

ABSTRACT

FACULTY OF ENGINEERING, SCIENCE AND MATHEMATICS

INSTITUTE OF SOUND AND VIBRATION RESEARCH

Doctor of Philosophy

ACTIVE CONTROL OF LOW FREQUENCY BUZZ-SAW TONES

by Matthew Jon Wilkinson

This thesis details a feasibility study into the use of active control for the attentuation of the low frequency components of the 'buzz-saw' sound field radiated from an aircraft engine on take off. Passive liner sections are currently used to attenuate the sound field, however, they have insufficient thickness to attenuate sufficiently the very low frequency components of the sound field. An active control system positioned after the liner section could be used to further attenuate the sound field.

This thesis shows that due to the simple modal structure of the buzz-saw noise, effective control of the sound field can be achieved by minimising the sum of the square pressures at a single ring of error sensors using a single ring of control actuators. In the absence of noise and extraneous modes, the level of control performance is fundamentally limited by the level of the evanescent modes at the error sensor array. An analytic model is developed which predicts the sound power reduction. Reflections are shown to be important in the control mechanism with standing wave regions identified between the secondary source array and the exhaust termination and between the inlet termination and the error sensor array.

The effect of extraneous modes and 'local' noise at the error sensor array on control performance is quantified. The relevant control mechanisms in the two cases are examined.

A modal control strategy which seeks to minimise the sum of the weighted spinning mode amplitudes at the duct wall is discussed. It is shown that if the spinning mode amplitudes are uniformly weighted, control performance is identical to that achieved by the minimisation of the sum of the square pressures. However, in the presence of noise, control is shown to be improved when the cost function is weighted such that control is focussed solely on the buzz-saw mode.

The thesis concludes with the results from an experimental rig. A real-time FXLMS algorithm is used to control a synthesised low order spinning mode by minimising the sum of the squared pressures measured at a single ring of 7 sensors using a single ring of 7 control actuators. The relationship between sound pressure reduction at the error sensors and the transmitted sound power reduction is investigated. Sound power reductions of up to 14.5dB are achieved. The control mechanism is identified from computer simulation.

Contents

List of Figures

List of Symbols

α	convergence parameter
$\alpha_{m,n}$	$\sqrt{1-\zeta_{m,n}^2}$
β	regularisation parameter
$\beta_{m,n}$	modal admittance ratio
Δx	separation distance $(x_e - x_s)$
$\gamma_{m,n}$	Power Factor
$\hat{a}_m$	spinning mode amplitude at the duct wall
$\hat{p}_m$	transformed primary pressure
κ	condition number
λ	eigenvalue
Ω	shaft rotational frequency
ω	angular frequency
$\Omega_{m,n}$	Cut-off ratio, as defined by Zorumski [63]
ϕ	phase
$\phi^+_{m,n}, \phi^-_{m,n}$	complex reflection phase factors
$\Psi_{m,n}$	radial mode shape function

$\psi_{m,n}$ Mode Shape function

ρ density

σ singular value

θ circumferential position in the duct

θ_s circumferential position of the secondary source

$\zeta_{m,n}$ cut-off ratio

a duct radius

$A_{m,n}$ Modal Pressure Amplitude

$a_{m,n}$ modal amplitude

$a_{p_{0_{m,n}}}$ amplitude of the primary mode at the fan face

$a_{s_{0_{m,n}}}$ Modal amplitude due to a point source in an infinite duct

B Number of Rotor Blades

c_0 speed of sound $= 343ms^{-1}$

C_m Complex Fourier Coefficient

c_p circumferential phase velocity

$d(n)$ disturbance signal

$D_{m,n}$ Modal directivity function

$e(n)$ error signal at the nth sample

f frequency

$G(z)$ acoustic plant response

$H(f)$ Frequency response function

I acoustic intensity

i	$\sqrt{-1}$
J	cost function
J_m	Bessel Function of the First Order
J_{min}	minimum value of the cost function
k	acoustic wavenumber ω/c_0
$k_{r_{m,n}}$	radial component of the acoustic wavenumber
$k_{x_{m,n}}$	axial component of the acoustic wavenumber
L	length of duct
m	spinning mode order
m_B	spinning mode order of buzz-saw mode
M_t	Tip speed Mach number
M_x	axial flow Mach number
m_{max}	maximum propagating spinning mode order
n	radial mode order
n_p	'Local' noise at the error sensors
$N_{m,n}$	Normalisation constant
p	acoustic pressure
p_p	primary acoustic pressure
p_s	secondary acoustic pressure
$p_{m,n}$	modal pressure
Q_m	modal source strength
q_s	secondary source strength

$q_{m,n}$ Morfey's[43] energy transmission coefficient

r radial position

$r(n)$ filtered reference signal at the nth sample

$R^{+}_{m,n}, R^{-}_{m,n}$ Modal reflection coefficients at the terminations

r_s radial position of the secondary source

S duct cross-sectional area

$S_{xx}(f)$ Power Spectrum

$S_{xy}(f)$ Cross-spectrum

SNR_{em} 'Signal to Noise Ratio' for extraneous modes in the primary field

SNR_{ln} 'Signal to Noise Ratio' for locally generated noise

T Non-dimensional time (defined in [42])

t time

$u(n)$ control signal at the nth sample

V Number of Stator Vanes

$W(z)$ response of the adaptive FIR filter

$W^{+}_{m,n}$ modal sound power fiowing toward the duct termination

w_i ith adaptive filter coefficient

w_m modal weighting coefficient

$W_{m,n}$ modal acoustic power

X Non-dimensional distance (defined in [42])

x axial position

$x(t)$ time series

$x(n)$ reference signal at the nth sample

x_f axial position of the fan plane

x_s axial position of the actuator array

Z_{mnl} generalized modal termination impedance

n sample number

$\hat{\mathbf{a}}_{\mathbf{m_p}}$ vector of primary amplitudes at the error sensor array

$\hat{\mathbf{a}}_{\mathbf{m_s}}$ vector of secondary amplitudes at the error sensor array

$\hat{\mathbf{a}}_m$ vector of spinning mode amplitudes at the error sensor array after control

$\hat{\mathbf{p}}$ transformed primary pressure matrix

$\hat{\mathbf{p}}$ transformed primary pressure signals

$\hat{\mathbf{Z}}_m$ 'modal' transfer impedance

$\mathbf{\Sigma}$ matrix of singular values

$\mathbf{g}$ complex gradient vector

$\mathbf{I}$ Identity matrix

$\mathbf{p_p}$ vector of primary pressures measured at the error sensors

$\mathbf{p_s}$ vector of secondary pressures measured at the error sensors

$\mathbf{p}$ vector of pressures measured at the error sensors after control

$\mathbf{R_{mnl}}$ matrix of modal reflection coefficients

$\mathbf{U}$ left-hand eigenvectors of a matrix

$\mathbf{V}$ right-hand eigenvectors of a matrix

$\mathbf{v}$ transformed source strengths

$\mathbf{W}$ matrix of modal weighting coefficients

$\mathbf{y}$ transformed error signals

$\mathbf{Z}_{\mathbf{mnl}}$ Matrix of modal scattering impedances

$\mathbf{Z}$ Transfer impedance matrix

Acknowledgements

The research presented in this thesis is funded by the European Union SILENCE(R) project.

I would like to thank Dr P.F.Joseph for his excellent supervision and invaluable help over the course of my PhD.

I would also like to thank Rob Stansbridge and the technicians for their help in designing my experimental rig.

Finally I would like to thank everyone with whom I have shared a coffee or a beer over the last three years for helping to keep me sane.

Chapter 1

Introduction

Associated with the vast magnitude of energy required to generate the thrust force in a modern aircraft engine and the inefficiencies inherent in any mechanical system are large energy losses as heat and, of more concern to the community, the generation of acoustic energy. In recent years, aircraft noise has become a very important environmental concern and large sums of money are being invested in research to combat the problem. The most recent research initiative by the EU is a project called SILENCE(R)(Significantly lower community exposure to aircraft noise) aimed at investigating technologies for the reduction of aircraft noise. In excess of 110 million Euros have been invested into research into novel technologies, with a view to reducing the EPNL (Effective Perceived Noise Level, the ISO standard subjective measure of aircraft noise) by 6dB by the year 2008. The research presented in this thesis is part of work package 1.4 of the SILENCE(R) project which seeks to investigate active noise control (ANC) strategies for the control of tonal fan noise.

Noise from a turbofan engine can be broadly categorised as originating from two main sources, jet noise from the exhaust of the engine and fan noise radiated forward of the engine. Originally, jet noise was the dominant noise source. However, over the past twenty years, engine designers have increased the bypass ratio of engines meaning that more air bypasses the core of the engine leading to less gas flow to the exhaust. This has resulted in a shift toward fan noise being the dominant noise source in most modern engines. Fan

noise is particularly problematic at take-off where the fan tip speed is often supersonic.

At supersonic fan tip speeds a shock wave system is produced at the fan tip resulting in sound radiated forward of the fan. This noise is tonal in character, with all harmonics of the shaft rotational frequency being present, and is commonly referred to as "buzz-saw" noise due to its similarity to the noise produced by a circular buzz-saw. Passive liners are currently used to attenuate this sound field, but they do not have sufficient thickness to attenuate the very low frequency components which are characteristic of this sound field. With inlets on modern engines becoming shorter, alternative technologies to passive liners to attenuate these low frequency components are becoming more important. This is the motivation behind work package 1.4 of the EU SILENCE(R) project. Previously, active control to control fan tones in aircraft engines has only been applied to rotor-stator interaction noise, which is produced by the interaction between the mean rotor wakes and the stator. This noise occurs at multiples of the blade passing frequency (BPF). At the BPF of a turbofan engine and its harmonics, a large number of modes may be excited and thus need to be controlled. This requires the use of a large and complex control system. By contrast, the control of the buzz-saw field appears more straightforward. It is dominated by low frequency tones for which the number of propagating modes in the duct is small. Control should be therefore be achievable using far fewer sources and sensors compared with that required for the control of rotor stator interaction tones. Research is being undertaken in the SILENCE(R) workpackage 1.4 into the feasibility of applying active noise control techniques in aircraft engines in order to control the low frequency tonal sound fields due to buzz-saw noise. The research presented in this thesis forms the ISVR contribution to this work package.

The following section outlines the previous work related to the active control of aircraft engine noise and active control of noise in other large ducted systems, such as chimney stacks.

1.1 Literature Review - Active Control of Aircraft Noise

1.1.1 Active control of cabin noise in propeller driven aircraft

Active noise control techniques have been successfully applied to control the tonal noise in the cabin of propeller driven aircraft. This application was studied both theoretically by Bullmore, Nelson and Elliott [9] and experimentally by Elliott, Nelson, Stothers and Boucher [16]. They showed that one could obtain good control of the sound field excited in the cabin at the first blade-passing frequency (BPF) of the propeller fan at 88Hz and its harmonics. In order to achieve this control they sought to minimise the sum of the squared pressure at an array of 32 sensor microphones using an array of 16 speakers mounted within the aircraft cabin. Sound pressure level reductions were measured throughout the cabin as well as investigations made into the localised control region of the sound field at higher frequencies around passengers' heads. At some locations in the cabin the A-weighted sound levels were reduced by up to 7dB(A).

The research on propeller-driven aircraft has led to the development and manufacture of commercial ANC systems for such aircraft and many systems are in operation today. However, the majority of civil aircraft in service are powered by turbofan engines. Over the last ten years a great deal of research has been published with regard to applying active control techniques to tonal noise from these engines. Surprisingly, however, none of these has dealt with the active control of buzz-saw noise, which dominates at take off.

1.1.2 Active control of turbofan engine noise

The sound field in an engine duct can be described as a summation of azimuthal spinning modes of order m (so-called because points on the wave front propagate in a helical pattern down the duct), each of which has an associated set of radial mode orders n. In the absence of reflections, equation 1.1 below describes the total pressure at a time t at a position (x, r, θ) in the duct.

$$p(x,r,\theta,t) = \sum_{l=1}^{\infty} \sum_{m=-\infty}^{\infty} \sum_{n=1}^{\infty} A_{m,n,l}\psi_{m,n}(r)e^{i(m\theta+k_{x_{m,n}}x-\omega_l t)} \tag{1.1}$$

where $A_{m,n,l}$ is the amplitude of the mode and $\psi_{m,n}$ describes the radial pressure variation of the mode. If one can independently control each of these modal components then one can achieve 'global' control of the sound field, in which the radiated sound field is reduced everywhere.

Rotor-stator interaction tones are produced at multiples of BPF, $\omega = lB\Omega$, where Ω is the shaft rotation frequency in radians, and are generated by the interaction of the wake produced by the rotor blade and the stationary stator blade. In a classic paper by Tyler and Sofrin [29], they show that m is given by

$$m = lB + KV \tag{1.2}$$

where K is any integer, B is the number of rotor blades and V is the number of stator vanes. Once the spinning mode orders m have been determined using equation 1.2 the number of associated radial orders n can be found by determining which radial modes will propagate in the duct at the lth multiple of the BPF. However, at any particular frequency ω_l, only a limited number of modes (m,n) can propagate with the rest being cut-off and therefore radiating weakly to the far-field.

One of the first papers to address the feasibility of using active noise control to control tonal noise from aircraft engines was Berge et al [6] in 1993 who used boundary elements to evaluate a control system with actuators mounted on the walls of the duct and sensors in the far field. Eight piston sources were used to reduce the levels of the sound field at control sources in the far field. The goal was not global control but to minimise radiation in the direction of the cabin and towards the ground. In their simulations, the field to be controlled (primary field) consisted of all modes which can propagate in the inlet duct at a frequency of 1000Hz. Reductions of 5-10dB were achieved at angles of $\theta = 45°$ and $315°$ in the far-field. However, it was noted that further studies were needed into the dependence

of control performance on frequency. Further investigation into the optimal positioning of the control actuators was also required.

Also in 1993, an analytic feasibility study was performed by Kraft and Kontos [37] who investigated the extent to which a wall mounted array of sources in a duct can couple into the circumferential and radial modes and hence control the sound field. They discuss the performance of such an array in the control of rotor-stator interaction modes in the inlet duct. They also discuss the source strengths required for effective control.

The control objective suggested by Kraft and Kontos [37] consisted of minimising the sound field on the ground as the aircraft flies overhead. However, they also mention that research into more practical inlet mounted error sensors was underway by the authors. The conclusion drawn from their study was that spinning modes m could be successfully excited by the array, but they were unclear as to how such an array could be used to excite the higher radial mode orders needed for effective control.

As well as the control of the sound field generated in the duct through the use of a distributed actuator and sensor array, other methods were suggested to control rotor-stator interaction tones 'at source'. Kousen and Verdon [36] in 1994 suggested that this could be achieved by mounting small actuators on the stator blades themselves. They suggested that by mounting as many actuators as there were propagating modes one could achieve global control of the sound field. They also indicated that the sound field could be reduced even when the number of propagating modes exceeded the number of control actuators. Further research into this approach includes a review by Simonich [53] of actuators for this purpose. This control approach is currently being studied experimentally as part of the EU SILENCE(R) project, but will not be discussed in this thesis.

1.1.3 Control of higher order modes in a chimney stack

Laugesen [40] has undertaken work detailing the active control of tonal noise in a chimney stack with a diameter of 4m. Although the geometry is different from that of the inlet duct, his work contains insight into the problem of controlling many duct modes

simultaneously. He describes theoretically and experimentally the control of tonal components from fans used in industrial chimney stacks. Piston-like sources are used to control the modes in a finite length hard walled rectangular duct. The minimisation of both sound power in the duct and sound pressure attempted at an array of microphones are investigated. He noted that in a real-time control system there is no practical way of measuring power and so power minimisation was only investigated hypothetically in order to establish the maximum possible global control obtained through power reduction. His large-scale experiments on a quarter section of a disused chimney section used 30 source and 32 sensors to control the first 30 modes which could propagate in the duct. Sound power reductions of 20-30dB where observed up to frequencies of 350Hz (corresponding to a non-dimensioanal frequency of $ka \approx 13$) and approximately 10dB of sound power reduction was measured at higher frequencies as the number of modes approached the number of control sources. An important finding was that using error sensors in the duct mounted close to the control actuators deteriorates control performance since evanescent modes are detected by the error sensors. Control effort is therefore wasted in trying to control these modes, which contain comparatively little sound power. He suggested that in order to avoid this problem, the source and sensor array should be positioned as far apart as possible. This finding is confirmed in this thesis.

1.1.4 Experimental results from the Pratt and Whitney JT15D Engine

A series of papers were produced by researchers at Virginia Tech that present the results of active noise control experiments on a Pratt and Whitney JT15D engine. Thomas et al [58] in 1993, performed some early experiments on this engine using a very simple control system consisting of an array of inlet mounted control sources to control the BPF tone at a single far-field error microphone. Control at the microphone gave local reductions of approximately 20dB. However, the control was limited to a small zone surrounding the microphone. It was suggested that global control of the entire sound field could be achieved by the use of a multi-channel control system. Thomas et al [58] also showed that control of multiple harmonics of BPF was possible. By using two independent controllers they controlled the first and second harmonics of BPF, yielding reductions of 17dB and

10dB at the error sensors.

A larger scale experiment was reported by Burdisso et al [10] who used a multi-channel control system to control an artificially generated rotor-stator interaction tonal sound field. This field was generated using exciter rods in order to generate the first order $m = 1$ spinning mode and the first four associated radial modes at the first BPF of $2450Hz$ ($ka \approx 12$). A system comprising 12 control actuators and 3 error sensors was used, and the controller consisted of 3 input channels from 3 error sensors and 3 output channels, with each output channel driving 4 actuators. The use of far field error microphones and in-duct microphone arrays were compared to control the radiated sound field. Using the three far field error sensors yielded reductions in sound pressure levels at almost all far-field angles. A sound power reduction of 5.1dB was achieved. A control strategy was then implemented whereby error sensors were mounted in the engine inlet duct. The aim of this experiment was not to drive the pressure at the error sensors in the duct to zero. Far field error sensors were mounted *outside* the duct and the sound field at these far-field error sensors was driven to zero. The levels measured at the error sensors were recorded and the far-field error sensors were removed. Once this model had been deduced, the control system could simply seek to reproduce the response at the error sensor which would result in the levels at the positions outside the duct being driven to zero. Using this technique, the sound pressure levels were reduced in some directions and the sound power reduction was 1.3dB suggesting that the use of inlet mounted error sensors had potential for further development.

1.1.5 Studies using alternative active control techniques

The previous studies in references [6, 10, 36, 40, 58] all address the control objective of minimising the pressure at error sensors using an array of control actuators. In the process of generating the control sound field (secondary field) the actuator array may generate modes which are not present in the primary sound field and thus these modes will degrade control performance. This is known as modal spillover. One way of dealing with this problem is to attempt to determine the original modal content of the sound

field and then reproduce this modal content exactly in the secondary sound field. To avoid modal spillover, a sufficient number of correctly positioned sources and sensors are needed.

An active control system was demonstrated experimentally in 1997 by Gerhold [22] which sought to exactly reproduce a single mode primary sound field to reduce the modal spillover effect. These experiments used inlet mounted error sensors to control the sound field. His control system used 2 error sensors to determine the modal content of the sound field. This mode was synthesised using 12 control actuators in order to cancel the field without exciting extraneous modes. He demonstrated that single low order modes could be sucessfully controlled using this approach. However, when multiple higher order modes were present, control performance was degraded.

A similar approach was applied to the control of higher order modes in an engine by Ishii et al [28]. Their study examined the development of a mode generation and mode detection system which could be mounted in the inlet of the engine. It was shown that modes of spinning mode order $m = 1 - 7$ could be detected and generated by an actuator array consisting of 16 actuators and that with the error sensor mounted in the inlet duct the sound pressure level could be reduced in all directions outside the duct. Reductions in the BPF tone varied between 2 and 10dB depending on the directivity angle. This study shows that this modal technique is a feasible approach in order to limit the degradation caused by modal spillover when simply reducing the pressure at a number of error sensors.

A study in 1997 by Chan [11] details a comparison of different control approaches when controlling higher order modes in both rectangular and circular ducts. Both the minimisation of the sum of the squared pressures at the error sensors and an approach whereby the individual mode amplitudes are minimised are compared. A similar comparison is made in this thesis in chapters 5 and 7. It is shown by Chan [11] that for multi-modal control in a circular duct minimising the sum of the squared pressures is more successful. This is thought to be due to the fact that in the circular duct there is strong coupling between the separate acoustic modes. Some other important insights are made in the study. Firstly, that the control performance measured at the error sensors may give a misleading

indication of the control performance elsewhere in the duct. Secondly, it is shown that the number of sensors required for control in the circular duct section is greater than in a rectangular duct and that these need to be properly postioned in order to obtain effective control.

In the same year Zander and Hansen [62] published a theoretical study into the use of various different control strategies to control both plane wave and higher order modes in a hard-walled rectangular duct. Four active control strategies were considered. Firstly, the minimisation of the sum of the squared pressures at the duct walls, which was used in the studies in sections 1.1.2 to 1.1.4. Secondly the minimisation of the acoustic potential energy in the duct was investigated. The acoustic potential energy can be estimated from the pressure measurements at an array of error sensors. The final practical control strategy was the minimisation of downstream sound power flow. This strategy requires two axially spaced arrays of microphones which are used to perform a modal decomposition to obtain the forward and backward flowing mode amplitudes. Using these one can minimise the downstream power flow. Also investigated was the minimisation of total acoustic power in the duct, however, as mentioned by Laugesen [40], this quantity is not easily measured in practice, thus results were only presented as a theoretical comparison.

It was found that significant benefits over the minimisation of the sum of the squared pressures could be gained by minimising the downstream power flow. The modal decomposition strategy was found to be able to eliminate the effect of dominant evanescent modes at the error sensors predicting aproximately 30dB improvement in downstream sound power reduction over the pressure minimisation control strategy. However, in order achieve this improvement, the number of sensors required was equal to the two times the number of propagating and the significant evanescent modes. At the higher frequencies associated with aircraft engine noise it is likely that a large number of sensors would be required for this control strategy.

1.1.6 Theoretical studies of the control of higher order modes and far-field directivity

An analytical study by Risi et al [52] in 1996 suggested an approach which could be used to control higher order radial modes. His model was of an engine inlet of finite length with no mean flow. The model control system consisted originally of 12 actuators, which were used to minimise the mean square errors at a number of far field error sensors. The primary sound field was modelled as the sound field excited by rotor-stator interaction at a BPF of 2400Hz. At this frequency only the spinning mode $m = 1$ is excited and only the first three radial mode orders propagate in the duct. Using a single array of control sources to minimise the error at 6 far-field sensors gave a predicted sound power reduction of 6.4dB. However, if one were to use a second axially spaced array of sources, a reduction of 28dB was predicted. This suggested that multiple axial arrays could be used to independently control higher order radial modes. This analytical result was later verified experimentally in a full scale experiment performed by Smith et al [55]. They showed that two axially spaced control arrays could reduce sound power reductions by 4dB using 2 arrays, whereas with a single array the sound power was reduced by only 1.7dB.

Further investigation into the merits of using inlet mounted sensor arrays was provided in a set of papers by Joseph et al [32, 33, 34]. The first of these papers was a preliminary theoretical study into the control of the first spinning mode order $m = 1$ using an axial line array of inlet mounted error sensors. A comparison is made between the control system using far-field sensors and a control system using a single axial line array of ten sensors. Good agreement is predicted between the sound power reduction yielded by each approach. A more detailed study was reported in references [33] and [34]. A model of the sound field at BPF produced due to rotor-stator interaction is predicted using a ring of axial dipoles which produce spinning modes associated with $m = 1$ and $m = 5$. Two source rings were used to control the sound field at far-field error sensors assuming perfect knowledge of the sound field. Two control objectives were investigated. One is the minimisation of total acoustic power, the second is the minimisation of the sum of the squared pressures at the error sensors in the far field. A control system consisting of several axially spaced rings

of error sensors within the engine inlet duct was compared with the far field results. It was seen that a degradation in control performance of only 6dB was predicted, suggesting that in-duct error sensors could be used for efficient control. Criteria were also suggested for the numbers of sources necessary for effective control. It was suggested that:

- the number of sources in a single ring needs to be at least equal to the highest spinning mode order m.
- the number of rings of sources needs to be equal to at least half the number of propagating radial mode order n associated with the axisymmetric spinning mode order $m = 0$.

The problem of cut-off modes 'contaminating' the sampled sound field is also briefly mentioned where it is suggested that the sources and sensors are placed as far apart as is possible to reduce this effect.

A further control objective is also suggested in the second paper [34] in which control effort is concentrated on the modes which radiate most strongly at the highest angles to the duct axis, thus reducing the sound field which is radiated toward the ground. This control objective is achieved by focusing the control effort on modes with the smallest axial wavenumber and hence which are least cuton. this was achieved by the use of an in-duct beamformer to estimate the far-field directivity. This approach was also investigated experimentally by Smith and Burdisso [54]. Ten pressure sensors were mounted in the inlet in an axial array and were used to attack radiation in the sector between 50° and 90°. Sound power reductions of 5.6dB were observed in this arc. A further theoretical study using boundary elements by Hutcheson et al [26] confirmed the merits of this control approach and suggested that it could be made more effective by using it in a hybrid active/passive system, where the control system is embedded in a passive liner section.

1.1.7 Recent studies on source and sensor requirements for ANC in ducts

Recent papers have suggested further criteria for the numbers and geometries required for the effective control of engine noise. Walker [60] suggests that the minimum number of sources used must be equal to the sum of the targeted mode spinning mode order and the maximum spinning mode order which can propagate in the duct. The minimum number of sensors should be the same as this number or greater. His paper also addresses several other issues which can affect active control performance. The contamination of the control by cut-off modes, as was mentioned earlier by Laugesen [40] and Joseph et al [34], and the inadvertent excitation of extraneous modes by the control actuators.

A paper presenting some theoretical findings of the EU RANNTAC (Reduction of Aircraft Noise by Nacelle Treatment and Active Control) project by Joseph, Fruteau and Nelson [31] gives clear criteria for the number of sources and sensors and the number of axially spaced arrays required for effective control. They suggest that the number of rings should be equal to the number of radial modes which one wishes to control and each of these rings should contain a number of sources or sensors equal to $2m_{max}+1$ where m_{max} is the maximum spinning mode order which can propagate in the duct. The paper concludes that in a practical system there will be only limited space in the inlet. For the limited amount of space one has in the inlet they suggest that the non-dimensional frequency limit below which control will be practically possible is approximately $ka = 16$. The experimental work associated with the RANNTAC projected was reported by Maier et al [41]. A control system consisting of 3 rows of 16 actuators and 5 rows of 36 error sensors mounted in the inlet were used to cancel a BPF tone consisting of the spinning mode $m = 3$. The report concluded that active noise control was best suited to low frequencies. At realistic ka values $15 \leq ka \leq 30$ an excessive number of sources and sensors would be required. Thus it was suggested that it could only be realistically implemented at low engine speeds.

Much research has focused on the active control of tonal components of the BPF components generated through rotor-stator interaction. It has been shown that discrete tone fan

noise is a feasible target for active noise control techniques. This research has identified some important guidelines for effective ANC in ducts. Control is most successful at low frequencies where few modes are excited in the duct. Criteria have been suggested for the numbers and arrangements of sources and sensors. It has also been shown that global control of the radiated sound field can be achieved in principle by mounting the entire control system within the duct inlet.

It is interesting to note that no work has been undertaken aimed at the active control of buzz-saw modes. This is surprising, as we shall show in the next section ANC seems to be well suited for reducing this component of aircraft engine noise. This thesis therefore will be the first published work to assess the performance of active control in attenuating low order buzz-saw tones. Several authors [32, 40, 60, 62] have noted that evanescent modes can contaminate the sound field in the engine inlet, however, the effect of these modes on the control mechanism will be investigated in further detail in this thesis. The thesis will conclude with the results from an experimental rig designed to control a single spinning mode with similar characteristics as the buzz-saw mode. Previous small and large scale experiments have focussed on simulating and controlling rotor-stator interaction tones.

1.2 Conclusions

- Active control has been successfully implemented in aircraft engines and large ducted systems. However, the research in aircraft engines has focussed on the control of the sound field generated by rotor/stator interaction. This occurs at frequencies where large numbers of modes can propagate in the duct section, thus large numbers of sources and sensors are required.

- No research has been published to date on the control of the lower frequency buzz-saw sound field.

- This thesis is the first study to detail the feasibility of using active control to attenuate the low frequency buzz-saw tones, which have a simpler modal structure than tones excited by rotor-stator interactions.

- The effect of evanescent modes will be investigated in detail in the thesis by examining the control mechanisms.
- The design and implementation of an original small-scale real-time active control experiment will be detailed which will simulate and control a single spinning mode with similar characteristics as a buzz-saw mode.

Chapter 2

Buzz-saw Noise - Its Generation and Propagation

2.1 Introduction

Noise radiated from aircraft engines by the fan can be divided into three different categories. These are:

- Tones occurring at frequencies of multiples of the blade-passing frequency (BPF)
- Tones occurring at frequencies of multiples of the shaft-rotational frequency.
- Broadband noise

Details on the characteristics of these sound fields and their generation can be found in reference [1].

In the previous chapter a review of the research into the active control of rotor-stator interaction tones was presented. This noise source falls into the first category. In this chapter we shall focus on a noise generating mechanism which occurs at harmonics of the shaft-rotational frequency. This is commonly referred to as "Buzz-saw" noise.

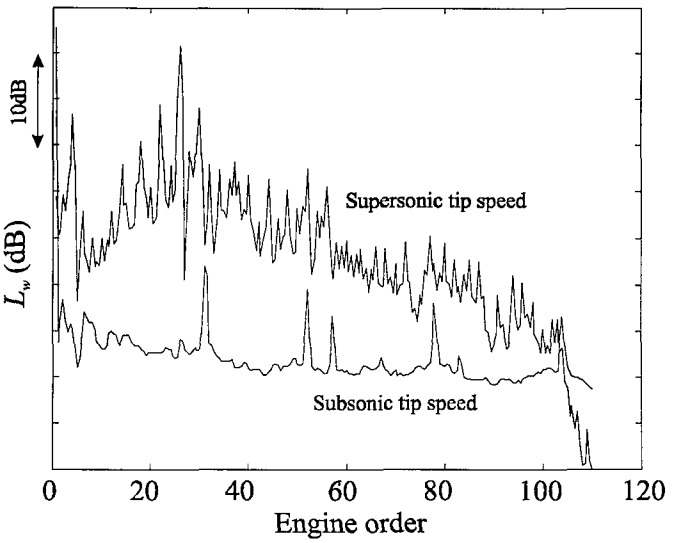

Figure 2.1: *A measured fan noise power spectrum for subsonic and supersonic fan tip speed conditions*

Figure 2.1 shows the measured sound power spectrum of the radiated noise from with the fan at supersonic and subsonic tip speed. At subsonic tip speeds, the sound field comprises a broadband noise floor plus tonal contributions at multiples of the fan BPF. At supersonic tip speeds associated with take-off conditions, the sound power level is significantly higher and markedly different in spectrum. There now exist tonal contributions at each Engine Order (multiples of the shaft rotational frequency) and the highest levels occur at Engine Orders (EOs) which are less than the first blade passing frequency of the fan. This tonal field is a characteristic of the buzz-saw sound field. Its generation and propagation will be discussed in the following sections.

2.2 Historical review

Research into buzz-saw noise in the early 1970's accompanied the development of high tip speed turbofan engines. Experimental studies of buzz-saw noise were undertaken by Benzakein et al [5], Kester [35] and Philpot [48]. Descriptions of the sound pressure levels and frequency content of buzz-saw noise measured from a supersonic tip speed fan were reported. It was shown by Philpot [48] in 1971 that as the tip speed Mach number of the

fan exceeded unity, the overall sound pressure level rose sharply, proving that supersonic tip speeds are required for buzz-saw noise to be present.[1] Buzz-saw noise was shown to be composed of discrete tonal contributions at each multiple of the shaft rotational frequency. Philpot [48] concludes that the buzz-saw noise field is radiated forward of the fan when the tip speed becomes supersonic. The field itself takes the form of " ...a steady rotating pressure field associated with the rotor" [48]. He suggests that the distinct frequency content of the buzz-saw noise is due to small imperfections between blades.

2.3 Physical mechanisms

Buzz-saw tones are usually only radiated at take off. At this supersonic tip speed, shock waves are produced at the blade tips, which gradually dissipate as they propagate down the duct due to viscous effects and heat conduction [59]. For a hypothetical perfect fan in which the fan blades are identical, a regular shock or "N" wave is produced at the fan face. This will travel down the inlet duct and will result in a sound field being radiated from the engine inlet comprising harmonics of the BPF. Morfey and Fisher [44] present a theoretical analysis of the shock wave propagation due to a fan operating at supersonic tip speed. They focus on the radiation from a perfect fan with identical blades and note that only harmonics of the blade-passing frequency will be radiated in this case. They also suggest that blade imperfections will lead to the frequency characteristics associated with buzz-saw noise, i.e. that tones are present at each EO.

The precise mechanism of buzz-saw noise generation is now well understood. Small imperfections between blades produce small differences in the shocks formed on each blade. The midpoint pressure is equal to the average of the pressures on each side of the shock wave. In the case of a perfect fan the average pressure of each shock will be equal. For imperfect blades the shock waves which form at the tips have slightly different mid-point pressures. The speed at which each shock wave propagates along the duct is dependent

[1] Buzz-saw tones have been artificially generated at subsonic speeds by using a fan with very large and impractical blade irregularities [35], however, in a real fan buzz-saw tones only dominate the spectrum at supersonic tip speeds

on the mid-point pressure [42]. The higher the mid-point pressure the faster the speed of propagation. Some faster moving shocks will merge with the slower shocks to form a new single shock wave. At the duct inlet a more irregular shock wave pattern will result. The frequency content of such a shock wave obtained through Fourier analysis, show that it is made up of discrete frequencies at multiples of the shaft rotational frequency. Buzz-saw noise is therefore sometimes known as "multiple pure tone" (MPT) noise. Kurosaka [39] further develops the Morfey and Fisher [44] theory to include the effects of blade non-uniformities. He investigates the effect of both blade spacing and differences in blade stagger angle on the generation of buzz-saw, or MPTs, and concludes that spacing has a negligible effect whereas the stagger angle is very significant with respect to tone generation. He also notes that errors in the blade contour angles can have a large effect on the generation of MPTs. Similar studies were undertaken by Hawkings [24] and Pickett [49]. However, the analysis of Kurosaka [39] does not rely on an estimate of the pressure signature at the fan face. The levels of the MPTs at the fan face are based on realistic blade irregularities. Hawkings [24] focuses on the propagation of an estimated shock wave which has an exaggerated irregularity. Pickett [49] assumes that the shock wave pattern at the fan face can be estimated from the statistics of the shock wave distribution from an average fan.

2.3.1 Non-linear, one-dimensional theory

Figure 2.2 shows the predicted pressure variation of the buzz-saw noise around a helical path in the inlet duct, both at the fan face and at the duct inlet termination. Below it is the associated frequency spectrum. These results were obtained using the FDNS (Frequency Domain Numerical Solution) model developed by McAlpine and Fisher [42], which predicts the propagation of buzz-saw noise in an aircraft engine inlet duct based on measured sound pressure data at the fan plane.

The FDNS method is a one-dimensional propagation model. The pressure is modelled by a Fourier series expansion with complex coefficients C_m corresponding to each spinning mode order m. These Fourier coefficients are approximately deduced from measurements

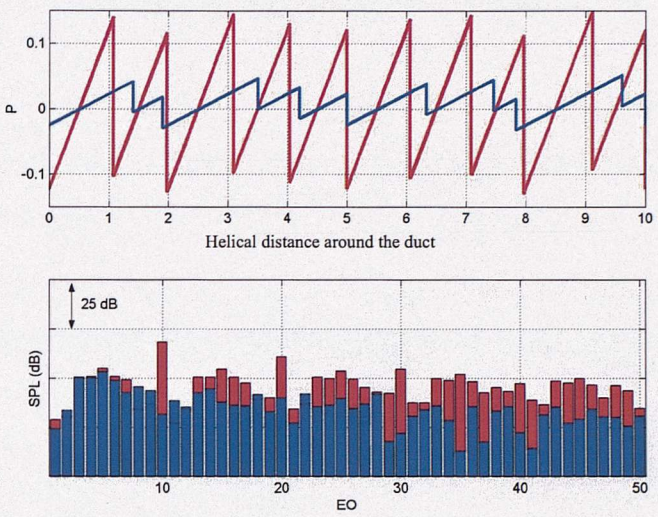

Figure 2.2: *Helical Pressure Variation and Frequency Spectrum at the fan face (red) and the duct inlet termination (blue) for "Buzz-saw" noise, predictions using the FDNS model by McAlpine and Fisher for a ten bladed fan. The top graph shows the pressure variation along a helical path in the duct, the lower graph shows the frequency spectrum.*

of the sound field close to the fan.

The pressure field is described in terms of a non-dimensional helical propagation distance X and as a function of non-dimensional time T. The shock wave pressure $P(X,T)$ at any point in the duct can therefore be expressed [42] as

$$p(X,T) = \sum_{m=-\infty}^{\infty} C_m(T) e^{imX} \tag{2.1}$$

The form of the solution of equation 2.1 is made to satisfy the non-linear wave equation known as Burgers equation and hence the values of C_m can be determined. The equation is slightly modified to account for liner attenuation. From McAlpine et al [42],

$$\frac{\partial p}{\partial T} + \underbrace{\frac{2\pi}{B} p \frac{\partial p}{\partial X}}_{(i)} = \underbrace{\frac{\epsilon}{B^2} \frac{\partial^2 p}{\partial X^2}}_{(ii)} - \underbrace{\sigma(m)\, p}_{(iii)} \tag{2.2}$$

Equation 2.2 contains three separate propagation terms, whose physical interpretation is as follows:

(i) A term to account for energy transfer between the modes, which is characteristic of non-linear propagation.

(ii) A dissipative term for the dissipation of energy by the shock waves due to viscous and heat conduction effects. This effect becomes more significant at the higher engine orders.

(iii) A linear attenuation term which has been added to Burgers equation to approximate the attenuation due to the presence of a acoustic liner section.

In order to determine the levels of the shock wave system at positions down the duct, equation 2.2 is integrated numerically to find the a new set of complex Fourier coefficients C_m at each axial position.

A typical pressure distribution is presented in figure 2.2 which shows the pressure distribution as a function of the helical distance around the duct for a fan with ten rotor blades in an inlet duct with rigid walls. The red line shows the helical pressure variation at the fan face and the blue line shows the predicted helical pressure distribution after the field has been propagated down the duct.

The pressure signature at the fan face (red line) resembles that of a regular shock wave. However, the mid-point pressures are slightly different across the shock system. As was mentioned earlier in this chapter, the differences in the mid-point pressures causes the shock waves to travel at slightly different speeds down the duct. Some shocks will meet and merge into a single shock resulting in a more irregular shock system at the end of the inlet duct (blue line). The pressure signature (red) close to the fan resembles a regular shock wave and thus the frequency content will be dominated by the BPF tonal components. For this ten-bladed fan, BPF corresponds to $EO = 10$. However, one can see that as the shocks travel down the duct and become more irregular the BPF tones no longer dominate the frequency spectrum. This energy exchange between different frequency components is

a consequence of the non-linear propagation of buzz-saw tones.

2.3.2 Linear, modal theory

It has been shown experimentally in a study by Rademaker, Sijtsma and Tester [51] that at 1BPF, for a supersonic fan with 26 blades, the dominant tone is dominated by the $m = 26$ mode. This is the mode $m = EO$ at 1BPF. Thus, at supersonic tip speeds the field is composed predominantly of modes with spinning mode order $m = EO$, otherwise referred to as 'rotor-alone' tones. A single-frequency buzz-saw tone is made up of contributions from all propagating modes at that frequency, however it is the 'rotor-alone' mode which will dominate.

The pressure due to buzz-saw noise can be expressed in a similar way to equation 1.1, however, all multiples of the shaft rotational frequency $w_l = l\Omega$ are now included.

$$p(x, r, \theta, t) = \sum_{l=1}^{\infty} \sum_{m=-\infty}^{\infty} \sum_{n=1}^{\infty} A_{m,n,l} \psi_{m,n}(r) e^{i(m\theta + k_{x_{m,n}} x - \omega_l t)} \tag{2.3}$$

where $\psi_{m,n}(r)$ is the modal shape function. This dominance of the $m = m_B = EO$ mode at each EO can be explained very simply. From the modal representation of the in-duct sound field in equation 2.3, a point of constant phase $\phi(\theta, t)$ on the modal wavefront, at fixed axial position along the duct x, can be written as

$$\phi(\theta, t) = \omega t - m\theta \tag{2.4}$$

Thus,

$$\theta = \frac{\phi}{m} - \frac{\omega t}{m} \tag{2.5}$$

The circumferential phase velocity of the mode of order m at frequency ω at the wall is

therefore

$$c_p = \frac{d\theta}{dt} = \frac{-\omega}{m} \tag{2.6}$$

The buzz-saw noise mode is phase-locked with the rotor and hence only occurs at supersonic tip speeds (since $c_p > c$ is a requisite for modal propagation, where c is the sound speed). The circumferential phase velocity is therefore equal to the shaft rotational frequency $c_p = \Omega$.

$$\frac{\omega}{m} = \Omega \tag{2.7}$$

and hence

$$m_B = \frac{\omega}{\Omega} = EO \tag{2.8}$$

Associated with each propagating spinning mode order m there are a number of radial modes with mode indices n. For the fan speeds and frequencies associated with buzz-saw tones, at spinning mode order $m = m_B = EO$, only the first radial order $n = 1$ is usually cut-on. In this thesis $n = 1$ is defined to be the lowest radial mode order.

An important non-dimensional quantity associated with each mode is the cut-off ratio $\zeta_{m,n}$. Different modes with the same cut-off ratio have very similar transmission and radiation characteristics.

The cut-off ratios of the dominant buzz-saw $(m_B, 1)$ modes at each EO are very similar. The cut-off ratio $\zeta_{m,n}$ is defined as the ratio of the non-dimensional frequency ka of excitation to the value of the non-dimensional frequency at which the mode begins to propagate. Thus modes will begin to propagate in the duct at frequencies corresponding to a cut-off ratio equal to 1. Cut-off modes have values of $\zeta_{m,n}$ less than 1 and decay in amplitude as they travel down the duct, thus will radiate weakly to the far-field. Well cut-on modes

will take values much greater than 1. In a duct with an axial flow speed of Mach number M_x the cut-off ratio $\zeta_{m,n}$ is defined as

$$\zeta_{m,n} = \frac{ka}{k_{r_{m,n}} a(1 - M_x^2)^{\frac{1}{2}}} \tag{2.9}$$

where $k_{r_{m,n}}$ is the transverse component of the acoustic wavenumber defined more clearly in chapter 3. Equation 2.9 can be written in terms of the blade tip Mach number M_t and the modal index m_B, which gives a better insight into the reasons why buzz-saw modes at different EOs have similar cut-on ratios. Putting $\omega = m_B\Omega$ into equation 2.9 gives

$$\zeta_{m,n} = \frac{\frac{m_B \Omega a}{c}}{k_{r_{m,n}} a(1 - M_x^2)^{\frac{1}{2}}} \tag{2.10}$$

Recognising that $\Omega a/c$ is the blade tip Mach number M_t gives

$$\zeta_{m,n} = \frac{m_B M_t}{k_{r_{m,n}} a(1 - M_x^2)^{\frac{1}{2}}} \tag{2.11}$$

Equation 2.11 shows that if the tip speed Mach number M_t, and hence the axial flow speed Mach number M_x, both remain constant, the cut-on ratios for each m_B mode will depend on the ratio $m_B/k_{r_{m,n}}$. For low frequency 'rotor alone' spinning mode orders m_B, this ratio is very similar. To a reasonable approximation, $k_{r_{m,1}} a \approx m + 1$. As the engine order increases the cut-off ratio $\zeta_{m,n}$ and $\frac{m}{m+1}$ become increasingly similar in value. Figure 2.3, below, shows the variation of $\zeta_{m,n}$ with varying tip speed mach number M_t, for various EOs, assuming $M_x = -0.52M_t$. This relationship is determined from the ratio of the Mach numbers specified for the SILENCE(R) RACE rig. Also illustrated in figure 2.3 are the tip speeds associated with 75%,85% and 95% of the design speed of a typical fan.

At a given tip speed, the cut-off ratios of the buzz-saw modes associated with $EO = 3$ to 14 have similar cut-off ratios. The cut-off ratio increases approximately linearly with increasing M_t, since M_x is usually small. At 75% of the fan design speed, all buzz-saw

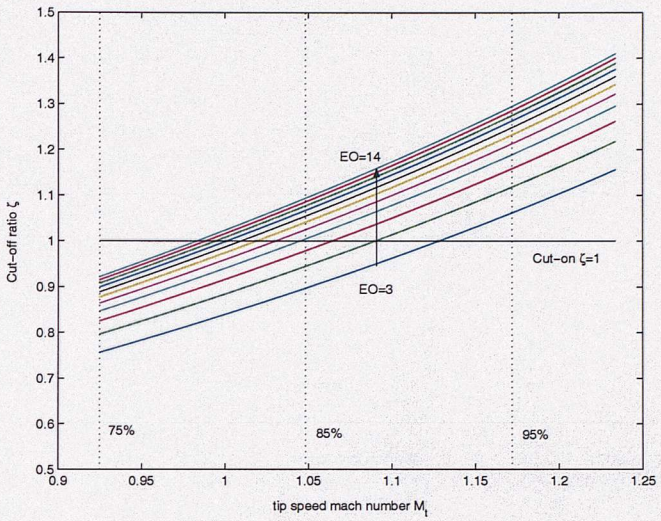

Figure 2.3: *Variation of cut-off ratio ζ of the 'rotor alone' modes for different fan speeds*

modes are cut-off. The tones cut on as the fan becomes transonic ($M_t \approx 1 - 1.1$). All of these modes are cut-on for M_t above 1.14.

In a hardwalled duct the mode shape function $\psi_{m,n}(r)$ take the form of a Bessel function, $J_m(k_{r_{m,n}} r)$, where $k_{r_{m,n}} = j'_{m,n}/a$, where $j'_{m,n}$ is the inflection point of the Bessel function where the gradient with the respect to the argument is equal to zero. Plotted in figure 2.4 are the Bessel functions corresponding to the buzz-saw mode for different m values at $n = 1$, as a function of radial distance r.

This graph demonstrates that as the spinning mode order of the buzz-saw mode m_B increases the modal pressure becomes increasingly concentrated along the duct wall and hence are more easily excited by the tip region of the fan in which the relative flow velocity is supersonic.

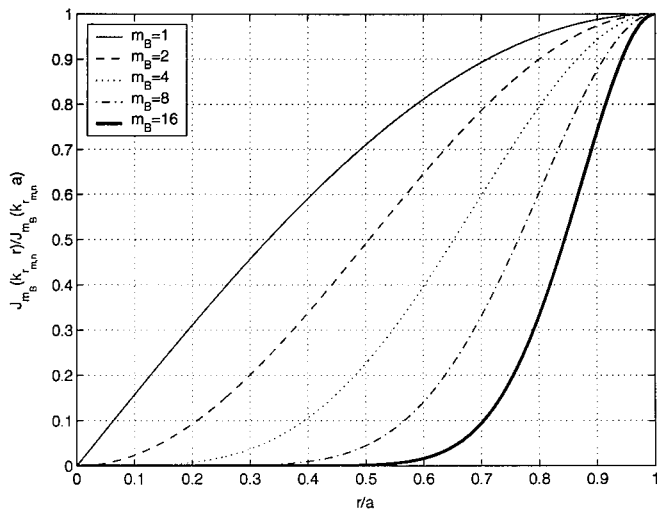

Figure 2.4: *Mode Shape Functions for the first radial modes at various buzz-saw spinning mode orders* $(m_B, n = 1)$

2.4 Suitability of buzz-saw noise for active noise control

Of the numerous tonal components present in the buzz-saw noise spectrum it is usually the tones below 1BPF which dominate the overall sound pressure level. This can be seen from the measured frequency spectra in Pickett [49], Vaidya [59] and Ehrich [14], for example. It is therefore predominantly tones much lower in frequency than 1BPF which we wish to control.

Presently, passive liner sections are introduced in modern engine inlets in order to control buzz-saw noise. However, these liners do not effectively attenuate the very low frequency components of buzz-saw noise. This is illustrated in figure 2.5 below. The theory developed by McAlpine and Fisher [42] was used to predict the buzz-saw spectrum at an aircraft engine inlet containing a liner section of 0.345m in length, located after the fan. The initial EO buzz-saw spectrum shown in Figure 2.5(a), is only an estimate of a typical buzz-saw spectrum. Using this estimate, the predicted buzz-saw spectrum at the end of the lined section (length 0.345m) is shown in Figure 2.5(b). Also shown is the predicted spectrum at this position with the liner is removed.

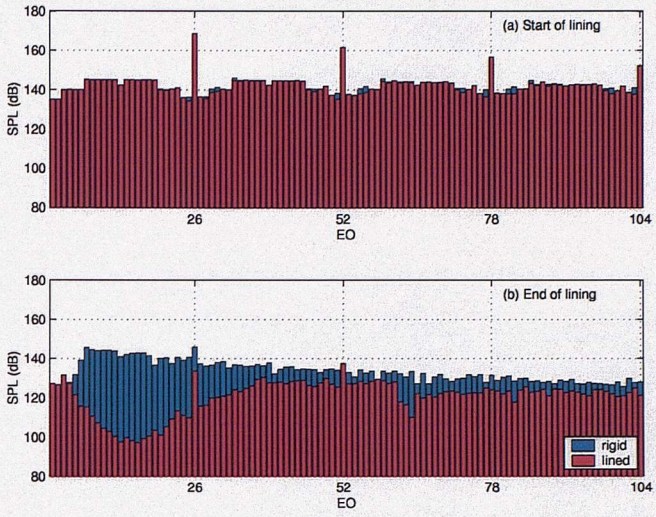

Figure 2.5: *Frequency spectrum for typical buzz-saw noise before and after a liner section of 0.345m in length. The spectrum before the liner is an estimate and the spectrum at the end of the liner section is predicted using the FDNS code developed by McAlpine and Fisher [42]*

Comparison between the two predicted spectra in the hard and soft wall cases suggests that the liner has been effective in attenuating most buzz-saw tones. At EO$<$ 7, however, there is comparatively little attenuation of the buzz-saw tones. An alternative treatment is therefore needed to suppress these low frequency components which will now dominate the overall sound pressure level.

The predicted sound pressure level spectrum in figure 2.5 is qualitatively similar to the measured spectra presented by Rademaker et al [51]. The test engine used in their experiments included a passive liner section in the inlet. Very low frequency engine order tones are still present at very high levels despite the presence of the liner. It should also be noted that the BPF tones in their data are still at very high level. One explanation for this is proposed by Vaidya [59]. He suggests that the role of the liner with respect to buzz-saw tones is to limit the amount of transfer of energy from the BPF tones to the buzz-saw tones.

An active noise control approach, implemented either after the liner section or built into the passive liner, may be used to form a hybrid active-passive noise control strategy in order to control these dominant low frequency tones. The design and effectiveness of an active control system positioned *after* a passive liner section will be the focus of this PhD thesis. The performance of the liner section is not investigated, however.

Conventional active control relies on the assumption that the propagation of the sound field is linear and that superposition applies. It is therefore important that active noise control system is applied in a region where the sound field can be assumed to propagate linearly. It is for this reason that the presence of passive treatment is essential. The levels of the buzz-saw tones must be attenuated from their initial levels of around 160dB (the level of the BPF tones shown in figure 2.5) to levels below approximately 130-140dB in order for a linear assumption to be valid.

2.5 Conclusions

- Buzz-saw noise is radiated forward of the fan on take-off and is caused by small imperfections between the fan blades.
- Buzz-saw modes occur at multiples of the shaft rotation frequency or engine orders (EO). At each engine order, a single mode dominates. This mode is equal to $(m = EO, 1)$.
- Passive liners are currently used to attenuate buzz-saw noise, however, the liner sections cannot attenuate the very low frequency buzz-saw tones and therefore it is these which will dominate the sound field and which will require further attenutation using active control.
- Active control relies on the assumption of linearity, and therefore a passive liner section will be required before the active control system such that the buzz-saw tones are at levels where they can be assumed to propagate linearly in the duct.

Chapter 3

Model of buzz-saw noise propagation in a finite-length duct with flow

In this chapter a numerical model of the sound field due to buzz-saw noise and the secondary sources is presented.

The duct model comprises the following simplifying assumptions:

- The engine inlet is a finite length axisymmetric circular duct with rigid walls. The flow is assumed to be uniform and in the axial direction.
- The ends of the duct are terminated in a rigid baffle
- The buzz-saw sound field at the sensor array microphones propagates linearly along the duct.
- The secondary sources are mounted flush with the duct walls and behave as point monopoles.
- The buzz-saw noise at each engine order (EO) comprises a single dominant propa-

gating primary mode ($m = EO, n = 1$) as discussed in Chapter 2.

3.1 Finite-length duct model

Figure 3.1 shows a circular duct of length L. Also shown are the positions of the actuator and sensor arrays and the approximate position of the fan in the EU SILENCE(R) RACE test rig. The direction of the uniform mean flow is also indicated, which is opposite to the direction of acoustic propagation in the duct inlet.

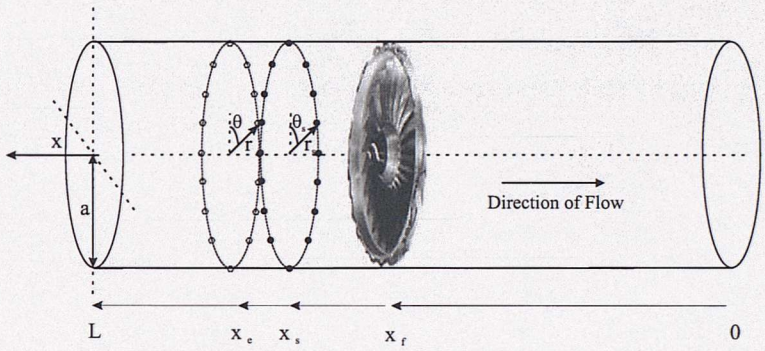

Figure 3.1: *Schematic diagram of the duct model, including a single ring of sources and sensors.*

3.1.1 The primary sound field due to buzz-saw noise

The buzz-saw sound field is only initially radiated forward of the fan, but then reflects repeatedly between the duct inlet and exhaust. Blockage by the rotor and stator, and other components of the engine, are not included in this simple model. We shall therefore formulate an expression of the in-duct sound field by launching a mode with an amplitude a_{p0} forward of the fan plane and summing subsequent reflections. The sound pressure $p(x, r, \theta)$ due to a single mode can be determined by the summation of all the incident and reflected waves due to this single forward propagating mode. At a single frequency summing reflected waves as shown in figure 3.2 gives

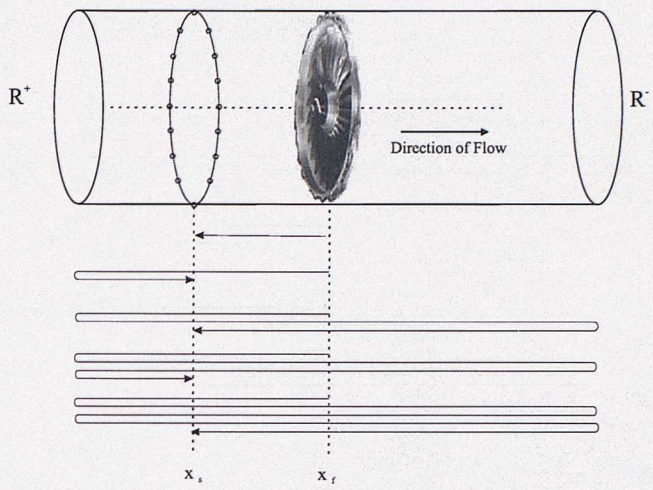

Figure 3.2: *Paths of the reflected waves launched from the fan face* x_f

$$
\begin{aligned}
p_{m,n}(x,r,\theta) \;=\; & a_{p_0}[e^{ik^+_{x_{m,n}}(x-x_f)} + R^+_{m,n}e^{ik^+_{x_{m,n}}(L-x_f)-ik^-_{x_{m,n}}(L-x)} \\
& + R^+_{m,n}R^-_{m,n}e^{ik^+_{x_{m,n}}(L-x_f)-ik^-_{x_{m,n}}L+ik^+_{x_{m,n}}x} \\
& + (R^+_{m,n})^2R^-_{m,n}e^{ik^+_{x_{m,n}}(L-x_f)-ik^-_{x_{m,n}}L+ik^+_{x_{m,n}}L-ik^-_{x_{m,n}}(L-x)} \\
& + (R^+_{m,n})^2(R^-_{m,n})^2e^{ik^+_{x_{m,n}}(L-x_f)-ik^-_{x_{m,n}}L+ik^+_{x_{m,n}}L-ik^-_{x_{m,n}}L+ik^+_{x_{m,n}}x} \\
& + \ldots]\psi_{m,n}(r,\theta) \qquad (3.1) \\
& x \geq x_f \quad (\textit{duct inlet}) \qquad (3.2)
\end{aligned}
$$

Here $\psi_{m,n}(r,\theta)$ is the normalised shape function of the mode (m,n) given by

$$\psi_{m,n}(r,\theta) = \frac{J_m(k_{r_{m,n}}r)e^{im\theta}}{N_{m,n}} \qquad (3.3)$$

where $N_{m,n}$ is a normalisation constant $N_{m,n}$ chosen to satisfy the normalisation condition $S^{-1}\int_S |\psi_{m,n}|^2 dS = 1$ where S is the cross-sectional area of the duct. For $m \neq 0$, it is given by

$$N_{m,n} = J_m(k_{r_{m,n}}a)\sqrt{1-\left(\frac{m}{k_{r_{m,n}}a}\right)^2} \qquad (3.4)$$

where J_m is the Bessel function of order m.

In equation 3.3, $k_{r_{m,n}}$ is the radial wavenumber that is chosen to satisfy the hard-walled boundary condition, $J'_m(k_{r_{m,n}}a) = 0$, where the prime denotes differentiation with respect to the argument.

Equation 3.1 can be written as the geometric series

$$\begin{aligned} p_{m,n}(x,r,\theta) &= \sum_{l=0}^{\infty} a_{p_0}[e^{ik^+_{x_{m,n}}(x-x_f)} + R^+_{m,n}e^{i(k^+_{x_{m,n}}-k^-_{x_{m,n}})L - ik^+_{x_{m,n}}x_f + ik^-_{x_{m,n}}x}] \\ &\quad \times \left(R^+_{m,n}R^-_{m,n}e^{i(k^+_{x_{m,n}}-k^-_{x_{m,n}})L}\right)^l \psi_{m,n}(r,\theta) \end{aligned} \tag{3.5}$$

whose sum to infinity reduces to

$$p_{m,n}(x,r,\theta) = \frac{a_{p_0}[e^{ik^+_{x_{m,n}}(x-x_f)} + R^+_{m,n}e^{i(k^+_{x_{m,n}}-k^-_{x_{m,n}})L - ik^+_{x_{m,n}}x_f + ik^-_{x_{m,n}}x}]\psi_{m,n}(r,\theta)}{1 - R^+_{m,n}R^-_{m,n}e^{i(k^+_{x_{m,n}}-k^-_{x_{m,n}})L}} \tag{3.6}$$

This assumption is valid as long as $|R^+_{m,n}R^-_{m,n}e^{i(k^+_{x_{m,n}}-k^-_{x_{m,n}})L}| < 1$. This will always be the case as the modulus of the reflection coefficients $R^+_{m,n}$ and $R^-_{m,n}$ will always be less than 1 apart from at $\zeta = 1$. However, the exponential term will always provide some dissipation.

For convenience, and to enable comparison with the previous results [43] the modal reflection coefficients evaluated at the duct terminations $R^{\pm}_{m,n}$ can be expressed in terms of a set of complex reflectivity phase factors $\phi^{\pm}_{m,n}$ [43],

$$R^+_{m,n} = e^{2i\phi^+_{m,n}(L)} = e^{2i\left(\phi^+_{0_{m,n}} - \frac{\alpha_{m,n}kL}{1-M_x^2}\right)} \tag{3.7}$$

$$R^-_{m,n} = e^{-2i\phi^-_{m,n}(0)} = e^{-2i(\phi^-_{0_{m,n}})} \tag{3.8}$$

from which the complex reflectivity phase factors $\phi^{\pm}_{m,n}(x)$ can be defined,

$$\phi^{+}_{m,n}(x) = \frac{\ln R^{+}_{m,n}(L)}{2i} + \frac{\alpha_{m,n} k(L-x)}{1-M_x^2} \tag{3.9}$$

$$\phi^{-}_{m,n}(x) = \frac{-\ln R^{-}_{m,n}(0)}{2i} + \frac{\alpha_{m,n} k(-x)}{1-M_x^2} \tag{3.10}$$

Substituting equations 3.7 and 3.8 into equation 3.6, and after some algebra, the final expression for the acoustic pressure at (x, r, θ) due to a buzz-saw mode $(m = m_B, n = 1)$ which is launched with an amplitude $a_{p_{0_{m_B,1}}}$ forward of the fan plane, becomes

$$p_p(x,r,\theta) = \frac{a_{p_{0_{m_B,1}}} \psi_{m_B,1}(r,\theta) i e^{i\phi^{-}_{m_B,1}(x_f)} \sec\phi^{-}_{m_B,1}(x_f)}{\left(\tan\phi^{+}_{m_B,1}(x_f) - \tan\phi^{-}_{m_B,1}(x_f)\right)} \frac{\cos\phi^{+}_{m_B,1}(x)}{\cos\phi^{+}_{m_B,1}(x_f)} e^{\frac{-iM_x k\left(x-x_f\right)}{1-M_x^2}} \tag{3.11}$$

The full derivation of equation 3.11 is detailed in Appendix A. In the above equations the parameter $\alpha_{m,n}$ is defined as

$$\alpha_{m,n} = \sqrt{1-\zeta^2_{m,n}} \tag{3.12}$$

where from equation 2.11

$$\zeta_{m,n} = \frac{mM_t}{k_{r_{m,n}} a (1-M_x^2)^{\frac{1}{2}}} \tag{3.13}$$

Note that $\alpha_{m,n}$ has an interpretation as a modal cut-off ratio, taking a value of $\alpha_{m,n} = 0$ at cut-off, tending to 1 for modes well above cut-off.

3.1.2 The secondary sound field due to control actuators

The secondary sound field excited in order to control the buzz-saw noise is assumed to be generated by an array of point monopole sources. Unlike buzz-saw noise, these will initially radiate sound in both directions along the duct. The acoustic pressure at (x, r, θ) due to a secondary source at (x_s, r_s, θ_s) radiating forward can be obtained by following an identical procedure to $p_p(x, r, \theta)$ in equation 3.11. For a mode of amplitude $a_{s_{0_{m,n}}}$ at the source location in the absence of reflection, the result is

$$\begin{aligned} p_s(x,r,\theta) &= \sum_{m,n} \frac{a_{s_0} i\psi_{m,n}(r,\theta)\left(e^{i\phi^-_{m,n}(x_s)}\sec\phi^-_{m,n}(x_s) + e^{-i\phi^-_{m,n}(x_s)}\sec\phi^-_{m,n}(x_s)\right)}{\left(\tan\phi^+_{m,n}(x_s) - \tan\phi^-_{m,n}(x_s)\right)} \\ &\quad \times \frac{\cos\phi^+_{m,n}(x)}{\cos\phi^+_{m,n}(x_s)} e^{\frac{-iM_x k(x-x_s)}{1-M_x^2}} \end{aligned} \tag{3.14}$$

Equation 3.14 reduces to an expression similar to that derived by Morfey [43].

$$p_s(x,r,\theta) = \sum_{m,n} \frac{a_{s_0} i\psi_{m,n}(r,\theta)}{\left(\tan\phi^+_{m,n}(x_s) - \tan\phi^-_{m,n}(x_s)\right)} \frac{\cos\phi^+_{m,n}(x)}{\cos\phi^+_{m,n}(x_s)} e^{\frac{-iM_x k(x-x_s)}{1-M_x^2}} \tag{3.15}$$

The modal amplitude term $a_{s_{0_{m,n}}}$ in equations 3.14 and 3.15 is that excited by the point monopole source in an infinite duct, evaluated at the position of the source,

$$a_{s_{0_{m,n}}} = \frac{\rho c_0 \psi^*_{m,n}(r_s,\theta_s) q_s}{2S\alpha_{m,n}} \tag{3.16}$$

given by $p(\mathbf{x}|\mathbf{x_s}) = ik\rho c_0 q_s(\mathbf{x_s}) G(\mathbf{x}|\mathbf{x_s})$ for a point source at $\mathbf{x_s}$ evaluated at the source plane $\mathbf{x} = \mathbf{x_s}$ and using the Greens function $G(\mathbf{x}|\mathbf{x_s})$ in equation 1.C.12 in Goldstein [13].

The final result for the secondary field at (x, r, θ) due to a point secondary source

$$p_s(x,r,\theta) = \sum_{m,n} \frac{i\rho c_0 q \psi_{m,n}(r,\theta)\psi^*_{m,n}(r_s,\theta_s)}{S\alpha_{m,n}(\tan\phi^+_{m,n}(x_s) - \tan\phi^-_{m,n}(x_s))} \frac{\cos\phi^+_{m,n}(x)}{\cos\phi^+_{m,n}(x_s)} e^{\frac{-ikM_x(x-x_s)}{1-M_x^2}} \tag{3.17}$$

3.2 Modal reflection coefficients for a flanged duct in the absence of flow

In the model of the ducted buzz-saw sound field we approximate the modal reflection coefficients $R^{\pm}_{m,n}$ in the equations in section 3.1 by the modal reflection coefficients for a semi-infinite flanged duct. These were evaluated using Zorumski's generalised impedance method [63] for the modal refiection coefficients for a semi-infinite duct terminated by an infinite, rigid baffle, in the absence of fiow. The theory predicts the modal refiection coefficients and includes the reflection coefficients of scattered modes whereby a single mode incident upon the end of the duct scatters into modes of different radial mode order. For simplicity, modal coupling will be neglected in our model.

The modal reflection coefficient may be deduced from the modal impedance at the duct termination. The generalized modal termination impedance is defined as the ratio of the modal pressure amplitude P_{mn} of the incident mode to the modal velocity amplitude V_{ml} of the reflected mode evaluated at the termination. It is a function of the non-dimensional frequency ka and is given by the equation 3.18 [63]

$$\begin{aligned} Z_{mnl}(ka) &= \int_0^{\frac{1}{2}\pi} \sin\phi D_{mn}(ka,\sin\phi) D_{ml}(ka,\sin\phi) d\phi \\ &- i\int_0^{\infty} \cosh\xi D_{mn}(ka,\cosh\xi) D_{ml}(ka,\cosh\xi) d\xi \end{aligned} \tag{3.18}$$

where D_{mn} is the modal directivity function, which can be written as

$$D_{mn}(ka,\tau) = \left\{ ka \left[\frac{\tau\psi_{mn}(ka)J'_m(\tau ka) - \lambda_{mn}\psi'_{mn}(ka)J_m(\tau ka)}{\lambda^2_{mn} - \tau^2} \right] \right\} \tag{3.19}$$

where the prime denotes differentiation with respect to the argument.

Note that the imaginary part of equation 3.18 is an infinite integral. However, the integral is rapidly convergent whereby good results can be obtained by truncating the upper limit

of integration to 10. At $\xi = 10$ and above the value of the imaginary part is of the order of 10^{-9}.

For a particular spinning mode order m, equation 3.18 defines the elements of a matrix of modal scattering impedances $\mathbf{Z_{mnl}}$,

$$\mathbf{Z_{mnl}} = \begin{bmatrix} Z_{m11} & Z_{m12} & \cdots & \\ \vdots & \ddots & & \vdots \\ \vdots & & \ddots & \vdots \\ & \cdots & \cdots & Z_{mn_{max}l_{max}} \end{bmatrix} \tag{3.20}$$

Using the theory due to Zorumski [63] one obtains a reflection coefficient of +1 at the modal cut-off frequency. However, both Rienstra & Hirschberg [57] and Norris & Sheng [47] note that at cut-off the reflection coefficient goes to -1. The Zorumski theory yields reflection coefficients with the correct magnitude, but with a phase which differs from that predicted in Rienstra & Hirschberg [57] by π radians. This discrepancy is corrected by both Hewlett [25] and Wang & Tszeng [61] who both use a similar expression to determine the reflection coefficients. With the error corrected, the matrix of reflection coefficients $\mathbf{R_{mnl}}$ is related to the matrix of impedances by

$$\mathbf{R_{mnl}} = (\mathbf{Z_{mnl}\Omega_{ml}} + \mathbf{I})^{-1} \times (\mathbf{Z_{mnl}\Omega_{ml}} - \mathbf{I}) \tag{3.21}$$

where $\mathbf{I}$ is an identity matrix with the same dimensions as $\mathbf{Z_{mnl}}$ and $\mathbf{\Omega_{ml}}$ is a diagonal matrix with elements equal to the cut-off ratio of equation 3.12 for $M_x = 0$

$$\Omega_{mn} = \alpha_{mn} = \frac{k_{x_{m,n}}}{k} = (1 - (k_{r_{m,n}}/k)^2)^{\frac{1}{2}} \tag{3.22}$$

The above method yields matrices of reflection coefficients which contain scattering terms. However, at frequencies close to cut-off, typical of buzz-saw frequencies, the leading diagonal elements dominate the matrix. Thus we will assume that the mode reflects energy

only into the same radial mode as that incident on the duct termination.

Figure 3.3(a) shows the variation of the magnitude of the modal reflection coefficients for spinning mode orders $m = 1$ to 5 and radial order $n = 1$, corresponding to EO's from 1 to 5. The graph is plotted against frequency expressed in terms of the cut-off ratio ζ, defined in chapter 2. Cut-off modes will have a cut-off ratio less than 1 and cut-on modes have a value much greater than 1.

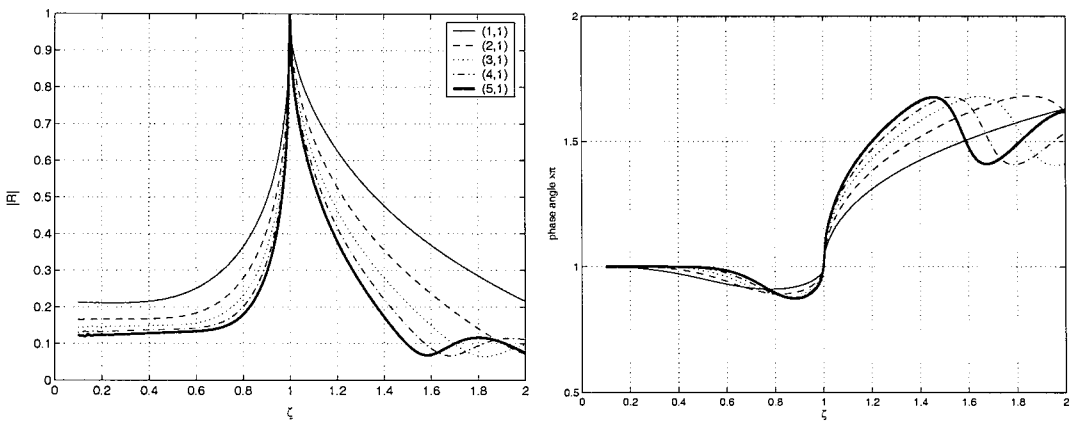

(a) (b)

Figure 3.3: *Modulus (a) and Phase (b) of the Modal Reflection Coefficients for spinning mode order m=1 to 5 and radial mode order n=1*

Comparison of figure 3.3(a) with the results obtained by Rienstra and Hirschberg [57] for the modulus and phase of the modal reflection coefficient for an unflanged duct indicates qualitatively similar behaviour. Note that their phase is defined to be negative owing to the choice of time convention $e^{i\omega t}$ adopted here, whereas Zorumski [63] assumes $e^{-i\omega t}$.

3.2.1 Extension to include mean flow

Johnston and Ogimoto [30] have shown that reflection coefficients with uniform mean flow can be expressed in terms of those with no mean flow by

$$R_{m,n}(ka, \alpha_{m,n}, M_x) = E_{m,n} \frac{k + M_x \alpha_{m,n} k}{k - M_x \alpha_{m,n} k} R_{m,n}(ka, \alpha_{m,n}, 0) \tag{3.23}$$

where $E_{m,n}$ in equation 3.23 takes a different value for the inlet and exhaust cases, which are respectively,

$$E_{m,n} = 1 \qquad (-1 < M_x \leq 0) \tag{3.24}$$

$$E_{mn} = \frac{k - M_x k^+_{x_{m,n}}}{k - M_x k^-_{x_{m,n}}} \quad (0 \leq M_x < 1) \tag{3.25}$$

In equation 3.25 above, the axial wavenumbers $k^{\pm}_{x_{m,n}}$ are defined

$$k^{\pm}_{x_{mn}} = \left(\frac{\pm\alpha_{m,n} - M_x}{1 - M_x^2} \right) k \tag{3.26}$$

Note that equation 3.23 reduces to the empirical expression derived experimentally by Ingard and Singhal [27] and later theoretically proved by Bohn and Zukoski [7] for the unflanged inlet plane wave reflection coefficient given by

$$R_{00}(M_x) = R_{00}(0)\left(\frac{1 - M_x}{1 + M_x} \right) \tag{3.27}$$

3.3 Energy transmission

In this section it will be shown that the approach used above to modify the reflection coefficients to include flow is consistent with energy conservation when the definition of acoustic energy in flow by Morfey is used. Morfey [43] defines a modal energy transmission coefficient $q_{m,n}$ as the ratio between the resultant sound power $W_{m,n}$ and the sound power $W^+_{m,n}$ flowing toward the duct termination,

$$W_{m,n} = q_{m,n} W^+_{m,n} \tag{3.28}$$

At frequencies above the cut-off frequency, $q_{m,n}$ can be deduced from [43]

$$q_{m,n} = 1 - |R_{m,n}|^2 \left(\frac{1 - \alpha_{m,n} M_x}{1 + \alpha_{m,n} M_x} \right)^2 \tag{3.29}$$

Since $q_{m,n} \leq 1$ by energy conservation, equation 3.29 imposes a fundamental limit on the maximum value of the modal pressure reflection coefficient, of the form

$$|R_{m,n}| \leq \left(\frac{1 + \alpha M_x}{1 - \alpha M_x} \right) \tag{3.30}$$

Substituting the expression for the inlet-duct absolute reflection coefficient with mean flow from equation 3.23 into equation 3.29 gives

$$q = 1 - |E_{mnl}|^2 |R^0_{mnl}|^2 \tag{3.31}$$

The terms on the right hand side will always be less than, or equal to one. Energy conservation is therefore satisfied by the transformation of equation 3.23.

The reflection coefficients and corresponding energy transmission coefficients are plotted in figures 3.4 and 3.5 for a range of Mach numbers, at frequencies above and below the cut-off frequency.

At frequencies near cut-off therefore, $|R_{m,n}| \approx 1$. This suggests that buzz-saw modes are strongly reflected at the duct termination leading to strong axial standing waves in the duct. The effect of these on active control performance is examined in chapter 5. In practice, blockage by the rotor and stator may cause the strongest reflection in the engine.

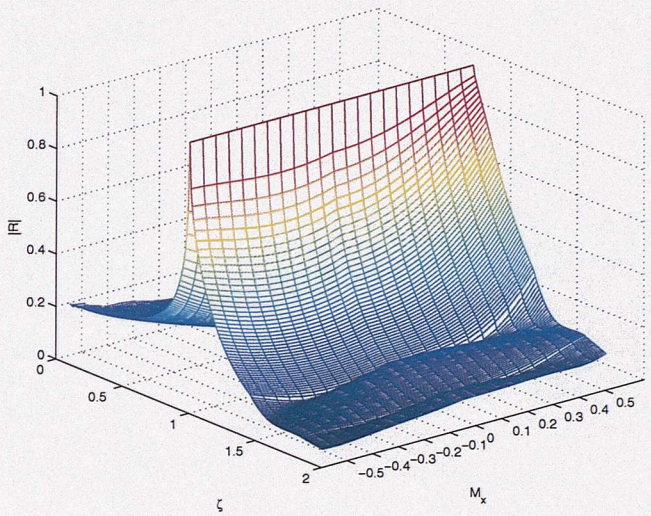

Figure 3.4: *Modulus of the Modal Reflection Coefficients*

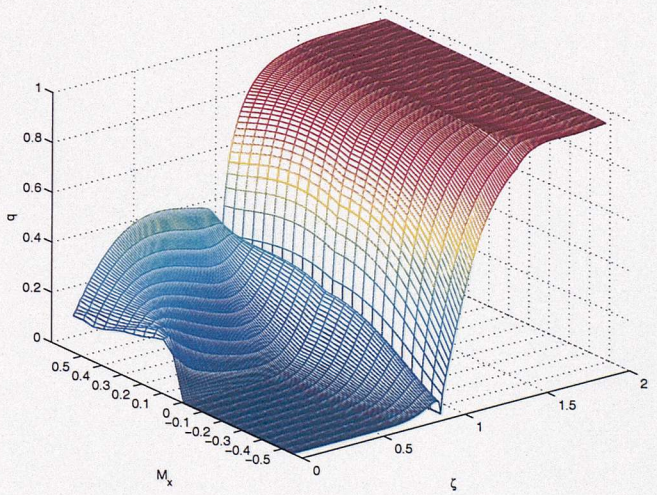

Figure 3.5: *Energy Transmission coefficients*

3.4 Conclusions

- A finite length duct model has been developed to model the propagation of buzz-saw noise in the engine inlet.
- The Zorumski [63] generalised impedance method has been used to estimate the modal reflection coefficients at the duct terminations. Modification was made to include a uniform mean flow. It has been shown that the reflection coefficients given by this model are consistent with the energy conservation definition given by Morfey [43].

Chapter 4

Active Control Theory

4.1 Control objectives

This chapter discusses the control objectives to be investigated in chapters 5 and 7. These are summarised below:

- Pressure Control - Minimising the sum of the square pressures measured at an array of microphones downstream of an array of secondary actuators. The relationship between pressure minimisation and reduction in total sound power radiated from the inlet will be clearly established.
- Modal Control - Minimising the sum of the weighted square modal amplitudes measured at the duct wall. Driving the modal amplitudes simultaneously to zero ensures that the radiated sound power is also zero. A large number of sensors are required to fully decompose the sound field into its spinning mode and radial modal contributions. This modal decomposition may also be difficult to implement in a real-time control system due to the higher computational overhead required. Therefore a more pragmatic approach will be investigated. We shall seek to minimise the sum of the spinning mode amplitudes at the duct wall, which can be inferred directly from the pressure measurements at the error sensors.

4.1.1 Minimisation of the sum of the squared pressures

The most widely used and practical control objective in most ANC duct applications consists of minimising the sum of the square pressures at error sensors mounted flush to the duct wall. At a single frequency we seek to minimise the cost function J with respect to the secondary source strength vector $\mathbf{q_s}$. The cost function is equal to the sum of the square pressures at the error sensors. In vector form, this may be written as $J = \mathbf{p^H p}$. The cost function relating to the sum of the squared pressures at I rings located at axial station x_i $(i = 1, I)$, each comprising L sensors, can be written as

$$J = \sum_{i=1}^{I} \sum_{l=1}^{L} |p(\theta_l, x_i)|^2 = \mathbf{p^H p} \tag{4.1}$$

Here, $\mathbf{p}$ is the vector of the pressures at the error sensors, which can be expressed as the sum of the contributions $\mathbf{p_p}$ from the primary source and $\mathbf{p_s}$ from the secondary sources. The primary pressure field at the error sensors is calculated from equation (3.11). The vector of secondary source pressures is given by $\mathbf{p_s} = \mathbf{Z q_s}$ where $\mathbf{Z}$ is a matrix of transfer impedances whose (i, j)th element is

$$Z(x_i, x_j) = \sum_{m,n} \frac{i\rho c_0 \psi_{m,n}(r_i, \theta_i)\psi^*_{m,n}(r_j, \theta_j)}{S\alpha_{m,n}(\tan\phi^+_{m,n}(x_j) - \tan\phi^-_{m,n}(x_j))} \frac{\cos\phi^+_{m,n}(x_i)}{\cos\phi^+_{m,n}(x_j)} e^{\frac{-ikM_x(x_i - x_j)}{1-M_x^2}} \tag{4.2}$$

Putting $\mathbf{p} = \mathbf{p_p} + \mathbf{Z q_s}$, the cost function J can be written in the Hermitian quadratic form [45],

$$J = \mathbf{q_s^H A q_s} + \mathbf{q_s^H b} + \mathbf{b^H q_s} + c \tag{4.3}$$

where $\mathbf{A} = \mathbf{Z^H Z}$, $\mathbf{b} = \mathbf{Z^H p_p}$ and $c = \mathbf{p_p^H p_p}$

The solution to $\partial J / \partial \mathbf{q_s} = 0$ for the optimum secondary source strength vector is of the form

$$\mathbf{q_s} = \mathbf{q_{opt}} = -[\mathbf{Z^H Z}]^{-1}\mathbf{Z^H p_p} \tag{4.4}$$

4.1.2 Minimisation of the sum of the squared spinning mode amplitudes at the duct wall

Here we seek to minimise the sum of square spinning mode amplitudes at the duct wall with respect to the secondary source strength vector $\mathbf{q_s}$, given by

$$J = \sum_{i=1}^{I} \sum_{m} |w_m \hat{a}_m(x_i)|^2 = \hat{\mathbf{a}}_m{}^{\mathbf{H}} \mathbf{W} \hat{\mathbf{a}}_m \tag{4.5}$$

where $\hat{\mathbf{a}}_m$ is a vector of the spinning mode amplitudes at the duct wall which can be written as the sum of the primary and secondary spinning mode amplitudes, $\hat{\mathbf{a}}_{m_p}$ and $\hat{\mathbf{a}}_{m_s}$ respectively. The diagonal matrix $\mathbf{W}$ can be used to weight the cost function such that control is focussed only on certain spinning mode orders.

A vector of the primary spinning mode amplitudes $\hat{\mathbf{a}}_{m_p}$ is calculated from the pressure measurements at the error sensor array. The mth element at an axial position x is given by

$$\hat{a}_m(x) = \frac{1}{L} \sum_{l=1}^{L} p(\theta_l, x) e^{-im\theta_l} \tag{4.6}$$

where the hat represent the amplitude at the wall. It should also be noted that a single subscript represents a spinning mode amplitude, and a double subscript represents the mode amplitude of a single (m,n) mode.

The secondary spinning mode amplitudes can be expressed as the product of a vector of secondary source strengths $\mathbf{q_s}$ and a modal 'transfer impedance' matrix $\hat{\mathbf{Z}}_m$ which describes the coupling between each secondary source and each spinning mode at each axial location

Following an identical procedure to the minimisation of $\mathbf{p^H p}$, the cost function of equation 4.5 can be expressed as a Hermitian quadratic form with respect to the complex secondary strength vector $\mathbf{q_s}$. The optimum source strength for minimising the sum of the square spinning mode amplitudes at the duct wall is given by

$$\mathbf{q_s} = \mathbf{q_{opt}} = -[\hat{\mathbf{Z}}_m^{\mathbf{H}} \hat{\mathbf{Z}}_m]^{-1} \hat{\mathbf{Z}}_m^{\mathbf{H}} \hat{\mathbf{a}}_{\mathbf{m_p}} \tag{4.7}$$

In order to determine the effectiveness of these control objectives the primary and secondary source strengths are used to determine the sound power transmitted along the duct, before and after control. The total transmitted power can be found from the following definition of sound power W in an axial uniform mean flow [43]:

$$W = \sum_{m,n} \gamma_{m,n} |a_{m,n}|^2 = \sum_{m,n} \frac{S|a_{m,n}|^2}{2\rho_0 c_0} [(1 + M_x^2) \Re \{\beta_{m,n}\} + M_x(1 + |\beta_{m,n}|^2)] \quad , \tag{4.8}$$

where $\beta_{m,n}$ is the modal admittance ratio, defined as the ratio of modal axial velocity $u_{m,n}$ to pressure $p_{m,n}$.

$$\beta_{m,n} = \rho_0 c_0 \frac{u_{x_{m,n}}}{p_{m,n}} = \frac{-i\alpha_{m,n}(1 - M_x^2) \tan \phi_{m,n}^+(x) - M_x(1 - \alpha_{m,n}^2)}{1 - \alpha_{m,n}^2 M_x^2} \tag{4.9}$$

The modal pressure amplitudes after control are determined from the sum of the primary and secondary mode amplitudes due to M sources.

$$a_{m,n} = a_{p_{m,n}} + \sum_{m=1}^{M} \frac{i\rho c_0 q(x_{s_m}, r_{s_m}, \theta_{s_m})}{S\alpha_{m,n}(\tan \phi_{m,n}^+(x_{s_m}) - \tan \phi_{m,n}^-(x_{s_m}))} \frac{\cos \phi_{m,n}^+(x)}{\cos \phi_{m,n}^+(x_{s_m})} e^{\frac{-ikM_x(x - x_m)}{1 - M_x^2}} \tag{4.10}$$

4.2 The Need for Regularisation

4.2.1 Inversion of the $\mathbf{Z^H Z}$ matrix

The active control theory outlined in section 4.1 relies fundamentally on the assumption that the inverse of the $\mathbf{Z^H Z}$ exists and can be accurately obtained. The extent to which a matrix can be accurately inverted is dependent on the singular values of the matrix. [17]

The singular value decomposition of a matrix $\mathbf{A}$ of dimension $L \times M$ is defined by

$$\mathbf{A} = \mathbf{U}\boldsymbol{\Sigma}\mathbf{V^H} \tag{4.11}$$

where $\mathbf{U}$ and $\mathbf{V}$ are square matrices of the left and right eigenvectors having dimensions of $L \times L$ and $M \times M$ respectively. The matrix $\boldsymbol{\Sigma}$ has the same dimensions as $\mathbf{A}$ and contains the M singular values σ_m of the matrix,

$$\boldsymbol{\Sigma} = \begin{bmatrix} \sigma_1 & 0 & \cdots & 0 \\ 0 & \sigma_2 & & \vdots \\ \vdots & & \ddots & \vdots \\ 0 & \cdots & \cdots & \sigma_m \\ 0 & \cdots & \cdots & 0 \\ \vdots & & & \vdots \\ 0 & \cdots & \cdots & 0 \end{bmatrix} \tag{4.12}$$

The inverse of the matrix can then be expressed very simply in terms of this singular value decomposition as

$$\mathbf{A^{-1}} = \mathbf{V}\boldsymbol{\Sigma}^{-1}\mathbf{U^H} \tag{4.13}$$

where $\boldsymbol{\Sigma}^{-1}$ can be written

$$\mathbf{A}^{-1} = \begin{bmatrix} \frac{1}{\sigma_1} & 0 & \cdots & \cdots & \cdots & 0 \\ 0 & \frac{1}{\sigma_2} & & \cdots & \cdots & \vdots \\ \vdots & & \ddots & \cdots & \cdots & \vdots \\ 0 & \cdots & \cdots & \frac{1}{\sigma_m} & \cdots & 0 \end{bmatrix} \tag{4.14}$$

Thus it can be seen that if the matrix has singular values that are equal to zero or smaller than machine precision, the inverse may be inaccurate due to numerical errors in its calculation.

Figure 4.1 shows the squared singular values of the impedance matrix $\mathbf{Z}$ for a control system with 30 sources and 30 sensors at EO=8 with an axial flow Mach number $M_x = -0.55$ and a tip speed Mach number of $M_t = 1.05$. The source array is postioned at $x_s = 1m$ and the sensor array is at $x_e = 1.24m$ in a duct of length $1.84m$.

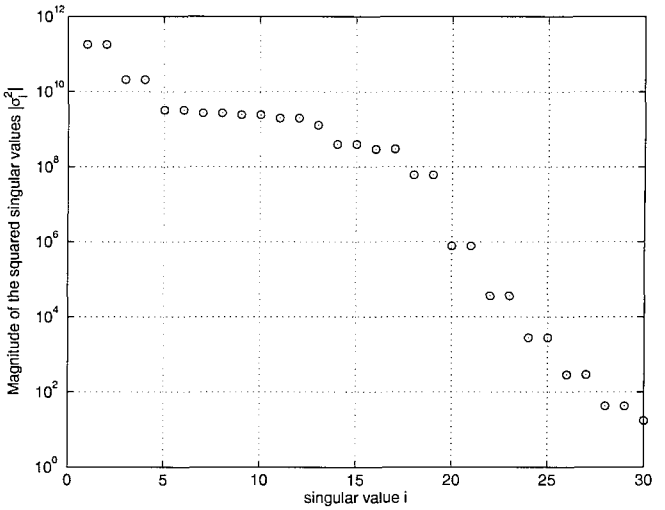

Figure 4.1: *The squared singular values σ_i of the* $\mathbf{Z}$ *matrix for a control system with 30 sources and 30 sensors at EO=8*

It is shown in figure 4.1 that the smallest singular value is of order 10. A matrix is said to be singular, and therefore has no inverse, if it contains one or more singular values which are equal to zero. It is clear therefore that this matrix is not close to singular and the inverse matrix should be easily obtainable numerically.

Although there are no eigenvalues close to zero, however, the range of singular values is of the order of 10^{11}. The range of the singular values provides a measure of the sensitivity of the control system to noise at the error sensors. This stability can be determined by examining the conditioning of the matrix $\mathbf{Z^H Z}$.

4.2.2 Matrix conditioning

An important quantity in matrix theory is the condition number $\kappa(\mathbf{A})$ of the matrix $\mathbf{A}$, which quantifies the sensitivity of errors in $\mathbf{x}$ to errors in $\mathbf{y}$, under the transformation $\mathbf{x} = \mathbf{A}^{-1}\mathbf{y}$. The condition number of a matrix is defined as the ratio of the maximum and minimum singular values,

$$\kappa(\mathbf{A}) = \frac{\sigma_{max}}{\sigma_{min}} \tag{4.15}$$

A matrix with a high condition number is said to be ill-conditioned and a low condition number is characteristic of a well-conditioned matrix. The condition number dictates how sensitive the control system is to small perturbations, or noise, on the primary pressure signals. An ill-conditioned control system will produce comparatively large variation in the optimal source strengths $\delta\mathbf{q}$ due to only a relatively small perturbation in the primary pressure measurements $\delta\mathbf{p_p}$. This relationship is given in equation 4.16 [2].

$$\frac{\|\delta\mathbf{q}\|}{\|\mathbf{q}\|} \leq \kappa(\mathbf{Z^H Z})\frac{\|\delta\mathbf{p_p}\|}{\|\mathbf{p_p}\|} \tag{4.16}$$

Equation 4.16 shows that if the condition number is large then only a small level of noise is needed at the error sensors to require an unrealistically large value for the optimum source strength.

4.2.3 Principal coordinates of the control system

Further insight into how the singular value spread affects the level of the optimum source strengths in the presence of noise can be carried out by transforming the system into its principal coordinates [17, 20]. If the transfer impedance matrix $\mathbf{Z}$ is expressed in terms of its left and right eigenvectors then the pressure at the error sensors is given by

$$\mathbf{p} = \mathbf{p_p} + \mathbf{U}\boldsymbol{\Sigma}\mathbf{V}^{\mathbf{H}}\mathbf{q} \tag{4.17}$$

Multiplying both sides by $\mathbf{U}^{\mathbf{H}}$, transforms the control problem into a decoupled set of equations known as the 'principal coordinates' of the system,

$$\mathbf{U}^{\mathbf{H}}\mathbf{p} = \mathbf{U}^{\mathbf{H}}\mathbf{p_p} + \boldsymbol{\Sigma}\mathbf{V}^{\mathbf{H}}\mathbf{q} \tag{4.18}$$

One can now define a transformed error signal $\mathbf{y} = \mathbf{U}^{\mathbf{H}}\mathbf{p}$ which is equal to the sum of the transformed primary pressure signals $\hat{\mathbf{p}} = \mathbf{U}^{\mathbf{H}}\mathbf{p_p}$ and the transformed source strengths $\boldsymbol{\Sigma}\mathbf{v}$, where $\boldsymbol{\Sigma}$ is the matrix of the singular values (see equation 4.12) and $\mathbf{v}$ is the transformed source strength $\mathbf{v} = \mathbf{V}^{\mathbf{H}}\mathbf{q}$,

$$\mathbf{y} = \hat{\mathbf{p}} + \boldsymbol{\Sigma}\mathbf{v} \tag{4.19}$$

The matrix of singular values $\boldsymbol{\Sigma}$ only contains non-zero values on the leading diagonal. The sum of the transformed pressure signals is therefore a set of uncoupled equations for each transformed source and sensor pair of the form

$$y_{\mathrm{m}} = \hat{p}_{\mathrm{m}} + \sigma_{\mathrm{m}} v_{\mathrm{m}} \tag{4.20}$$

We can now minimise the new transformed cost function (which is the same as minimising the original cost function, since $\mathbf{y}^{\mathbf{H}}\mathbf{y} = \mathbf{p}^{\mathbf{H}}\mathbf{U}\mathbf{U}^{\mathbf{H}}\mathbf{p} = \mathbf{p}^{\mathbf{H}}\mathbf{p}$). The minimum value of $\mathbf{y}^{\mathbf{H}}\mathbf{y}$

with respect to $\mathbf{q}$ or $\mathbf{v}$ in terms of $\mathbf{\Sigma}$ is given by

$$J_{min} = \hat{\mathbf{p}}^{\mathbf{H}}[\mathbf{I} - \mathbf{\Sigma}[\mathbf{\Sigma}^{\mathbf{H}}\mathbf{\Sigma}]^{-\mathbf{1}}\mathbf{\Sigma}^{\mathbf{H}}]\hat{\mathbf{p}} \tag{4.21}$$

The leading diagonal of the $[\mathbf{I} - \mathbf{\Sigma}[\mathbf{\Sigma}^{\mathbf{H}}\mathbf{\Sigma}]^{-1}\mathbf{\Sigma}^{\mathbf{H}}]$ matrix only contains non-zero elements for the last $L - M$ elements where L is the number of sensors and M is the number of sources. This suggests that for an overdetermined system where there are more sensors than sources, the minimum value of the cost function is determined by these values of the transformed primary pressure signals. Thus the cost function $\mathbf{J} = \mathbf{y}^{\mathbf{H}}\mathbf{y} = \mathbf{p}^{\mathbf{H}}\mathbf{p}$ can be written as the expression below:

$$J = J_{min} + \sum_{m=1}^{M} |y_m|^2 \tag{4.22}$$

For the square control system, where the number of sources and sensors are equal, the value of J_{min} will be zero.

Equation 4.22 suggests that in order for the control system to converge on the minimum value, the second term in the equation must decay to zero. This formulation leads to the idea of 'modes of convergence' of the control system. From this concept we can explain the behaviour of the system in detail. Each of these modes of convergence decays to the minimum value of the cost function with a time constant which is inversely proportional to the squared singular value of $\mathbf{Z}$, which is equal to the eigenvalue λ_m of $\mathbf{Z}^{\mathbf{H}}\mathbf{Z}$ [17].

$$\lambda_m = \sigma_m^2 \tag{4.23}$$

In a badly conditioned control system, therefore, where the singular value spread is large, the modes will converge at different rates, and, as indicated by equation 4.20, a large source strength will be required to control the slower modes. If the sources and sensors in a control system are positioned such that they are weakly coupled, for example due to transducers on the nodal line of a dominant mode then a large source strength is required

in order to control the mode. In the same way, if the singular value is small, then the transformed sources will be badly coupled into the associated control mode and hence a high source strength is required.

The decay of the cost function for a real-time control system at each sample time n can be written approximately as

$$J(\mathrm{n}) \approx J_{min} + \sum_{m=1}^{M} |p_m|^2 \, e^{-2\alpha\lambda_m n} \tag{4.24}$$

where p_m is the mth element of the transformed pressure vector $\mathbf{p}$, and λ_m is the mth eigenvalue of the $\mathbf{Z^H Z}$ matrix. The parameter α in this case is the convergence parameter for the real-time control system. This parameter will be discussed later in this thesis.

The eigenvalue spread of the matrix $\mathbf{Z^H Z}$ for the system decribed in section 4.2.1 is identical to the spread of the squared singular values of the matrix $\mathbf{Z}$ shown in figure 4.1. The conditioning of the transfer impedance matrix will be highly dependent on the size of the duct, and the positions of the source and sensor arrays both axially and circumferentially. Elliott [17] notes that the condition number will increase as the actuators and sensors are positioned closer together, and when the number of sources exceeds the number of significant modes.

At EO=8 the range of spinning modes that can propagate in the duct is $-8 \leq m \leq 8$. Correspondingly, figure 4.1 shows that the first 17 singular values are similar in magnitude. When only these singular values are retained, the condition number of this truncated matrix will be of the order 10^2 and the matrix is therefore relatively well-conditioned. The remaining eigenvalues reduce rapidly resulting in a large condition number when all 30 eigenvalues are included.

Figure 4.2 shows the magnitude of the transformed primary pressure signals $\hat{\mathbf{p}}$. This graph identifies the transformed primary disturbances that need to be attenuated in order to reach the minimum value of the cost function.

For the square control system with 30 sources and 30 sensors, the minimum value of the cost function is zero. In order to achieve this minimum value the uncoupled equations of the form shown in 4.20 must also be equal to zero,

$$y_{\mathrm{m}} = \hat{p}_{\mathrm{m}} + \sigma_{\mathrm{m}} v_{\mathrm{m}} = 0 \tag{4.25}$$

Clearly, if the transformed pressure signal $\hat{p}_{\mathrm{m}}$ is much greater than zero and the associated singular value σ_{m} is small, then the required transformed source strength will be large in order for the sum to be equal to zero.

By relating each of the dominant pressure signals to its associated eigenvalue one can determine whether the associated transformed source can couple well into the mode of convergence in order to achieve this desired decay.

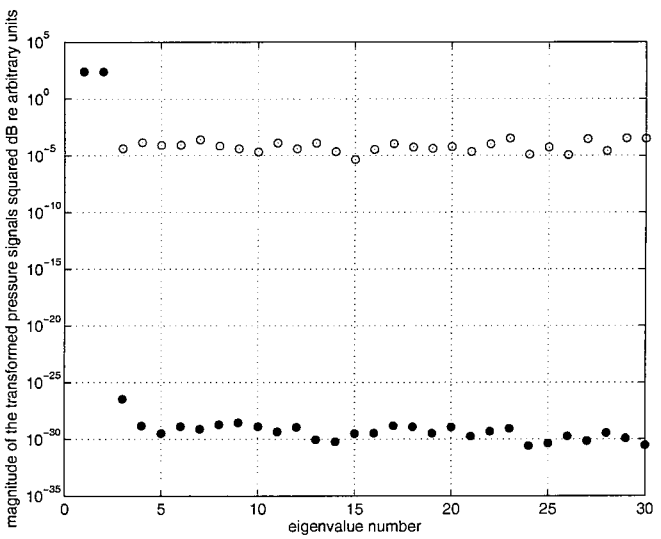

Figure 4.2: *The magnitude of the primary pressure contribution transformed into the coordinates of the control system for the noise-free single mode case (filled) and with 40dB signal to noise ratio at the error sensor (empty)*

Figure 4.2 shows that in the absence of noise with only a single dominant mode present in the primary sound field, the first two transformed primary pressure signals are dominant. These will correspond to the forward and backward buzz-saw spinning mode ($m = m_B$) in

the primary pressure field. The remaining transformed primary pressures have an insignificant magnitude of the order of 10^{-30}, which is close to the minimum value of the cost function. The significant transformed pressure values are associated with large singular values. The transformed sources should therefore couple well into the modes of convergence allowing the system to converge to a minimum value very quickly. Control can be achieved without excessive source strengths being required. We can see also that although there are smaller singular values, the transformed primary pressure signals associated with these eigenvalues are close to the minimum value of the cost function and thus will not require high source strengths to converge. Although the matrix itself is badly conditioned, the noise-free transformed system is 'well-conditioned' and will converge to a minimum value without requiring excessive source strengths.

However, with 40dB of signal to noise ratio at the error sensors (circles in figure 4.2), all of the transformed pressure signals are now significant. In this simulation, the 'noise' is assumed to be local to the error sensors and comprises of random additions to the primary pressure vector. If the pressure signals are noisy at the error sensors, then there will be an amplitude contribution at each spinning mode order, whether the mode is cut-on or cut-off. Thus these values need to decay to zero in order to reach the minimum value of the cost function. The transformed primary pressure signals associated with the small singular values will generate larger secondary source strengths in order to control the sound field.

The following section presents a method for constraining the control system. This has the effect of increasing the small singular values and hence improve the conditioning and the stability of the control system.

4.2.4 Tikhonov regularisation

Tikhonov regularisation adds to the unconstrained cost function presented in section 4.1.1 a term that penalises control effort. The regularised cost function for pressure control, is given by

$$J = \mathbf{p}^{\mathbf{H}}\mathbf{p} + \beta \mathbf{q}_{\mathbf{s}}^{\mathbf{H}}\mathbf{q}_{\mathbf{s}} \tag{4.26}$$

where β is an arbitrary dimensional constant which is referred to as the Tikhonov regularisation parameter. In order to explain the effect that regularisation has on the control stability, we shall once again perform a singular value decompostion on the transfer impedance matrix $\mathbf{Z}$.

One can obtain the vector of optimal secondary source strengths in the regularised case in terms of the singular value decomposition of $\mathbf{Z}$.

$$\mathbf{q_{opt}} = -\mathbf{V}[\mathbf{\Sigma}^{\mathbf{H}}\mathbf{\Sigma} + \beta\mathbf{I}]^{-1}\mathbf{\Sigma}^{\mathbf{H}}\mathbf{U}^{\mathbf{H}}\mathbf{p_p} \tag{4.27}$$

where

$$[\mathbf{\Sigma}^{\mathbf{H}}\mathbf{\Sigma} + \beta\mathbf{I}]^{-1}\mathbf{\Sigma}^{\mathbf{H}} = \begin{bmatrix} \frac{\sigma_1}{\sigma_1^2+\beta} & 0 & \cdots & \cdots & \cdots & 0 \\ 0 & \frac{\sigma_2}{\sigma_2^2+\beta} & & \cdots & \cdots & \vdots \\ \vdots & & \ddots & \cdots & \cdots & \vdots \\ 0 & \cdots & \cdots & \frac{\sigma_n}{\sigma_n^2+\beta} & \cdots & 0 \end{bmatrix} \tag{4.28}$$

As $\beta \rightarrow 0$, $\frac{\sigma_n}{\sigma_n^2+\beta}$ approaches $\frac{1}{\sigma_n}$ and the matrix in equation 4.28 becomes equal to the inverse of the singular value matrix of $\mathbf{Z}^{\mathbf{H}}\mathbf{Z}$ in equation 4.14. For large regularisation parameter $\frac{\sigma_n}{\sigma_n^2+\beta}$ approaches $\frac{\sigma_n}{\beta}$ [46]. Introducing a regularisation parameter therefore has the effect of increasing the near zero singular values while keeping the higher singular values close to their original values. This filtering effect is explained in further detail by Hansen [23].

With reference to the modes of convergence of the control system, the addition of this regularisation parameter modifies the rate of decay. The modes will now converge with a time constant which is inversely proportional to the modified eigenvalue $\lambda_m = \sigma_m^2 + \beta$, where σ_m is the mth singular value of the transfer impedance matrix $\mathbf{Z}$. Thus the value

of the cost function at each sample time n now becomes [17, 18]

$$J(n) = J_{min} + \sum_{m=1}^{M} \frac{\sigma_m^2}{\sigma_m^2 + \beta} |\hat{p}_m|^2 e^{-2\alpha\lambda_m n} \tag{4.29}$$

4.2.5 Choice of regularisation parameter

Much work has been published in recent years regarding the use of the *L-curve* in determining the 'optimal' regularisation parameter [23]. In terms of the active noise control problem, an *L-curve* is formed by plotting the 2-norm of the optimal secondary source strengths $\|\mathbf{q_{opt}}\|$ against the 2-norm of the residual pressure at the error sensors after control $\|\mathbf{Z q_{opt}} + \mathbf{p_p}\|$. The 'optimal' regularisation parameter is said to be the β-value that 'balances' $\|\mathbf{q_{opt}}\|$ and $\|\mathbf{Z q_{opt}} + \mathbf{p_p}\|$ such that both values are simultaneously as small as possible.

We have seen that the high condition number of the transfer impedance matrix will result in large values for the secondary source strengths due to small values of noise in the pressure measurements. Figure 4.3 below shows the L-curve for the control system described in section 4.2.1 with 40dB Signal to Noise Ratio at the error sensor array. In order to 'filter out' the smaller singular values in the matrix, the regularisation parameter β must be greater than the squared minimum singular value of the matrix σ_{min}^2. The minimum squared singular value is of the order 10^2 from figure 4.1. Thus, β is varied from $\beta = 1000$ and $\beta = 1 \times 10^{11}$.

The 'optimal' regularisation parameter is said to occur at the 'corner' of the L-curve and from figure 4.3 is equal to $\beta = 5.5 \times 10^7$.

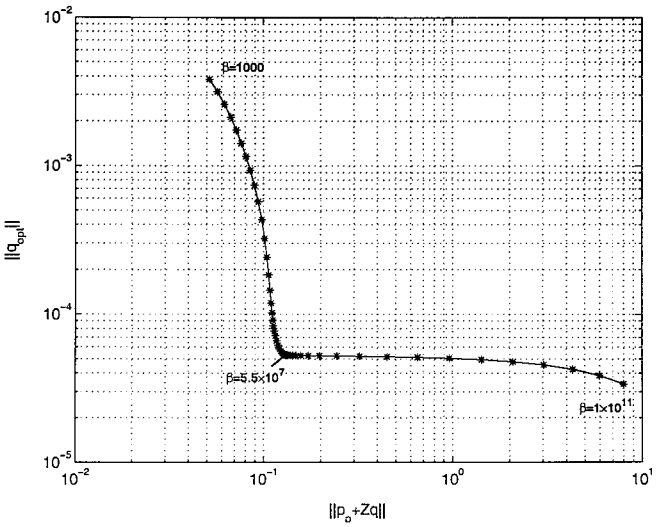

Figure 4.3: *Variation of 'optimal' source strength and residual sound pressure at the error sensors with varying values of β for a system with 30 sources and sensors at EO=8*

In figure 4.1 we have identified that there are 17 significant singular values, associated with the propagating modes in the duct. The optimal value of β identified in figure 4.3 will increase all of the singular values $i > 18$ such that the spread of singular values is approximately 10^3 and thus the modifed $\mathbf{Z}$ matrix is now well conditioned. If the regularisation parameter is increased beyond this value, it will begin to alter the singular values $i = 1 - 17$ associated with the propagating modes and thus control performance will be degraded.

The optimal value of β will be particular to the arrangement of sources and sensors, frequency and value of SNR at the error sensors, and will need to be recalculated for each case.

4.3 Conclusions

- For the single ring control system with 30 sources and 30 sensors at EO=8, the transfer impedance matrix $\mathbf{Z}$ has no singular values close to zero. The inverse exists and therefore a global minimum exists for the cost function J.

- The condition number $\kappa(\mathbf{Z})$ is very large indicating that the matrix is ill-conditioned. The addition of a small amount of noise at the error sensors will result in a comparatively large increase in the required source strengths.

- It has been shown that regularisation is required in order to limit the source strengths if 'noise' is present at the error sensors. An 'optimal' value for the regularisation parameter β exists and this value will be dependent on the system characteristics.

Chapter 5

Active Control performance when minimising the sum of the square pressures in the absence of extraneous modes

5.1 Introduction

This chapter examines theoretically the performance of the active control of a single buzz-saw mode obtained by minimising the sum of the squared pressures at the error sensors. In this chapter it is assumed that extraneous modes and noise at the error sensors are absent. This control method is used in most practical commercial active control systems due to the simplicity of its implementation. Unlike modal control (Chapter 7), for example, no phase calibration of the error sensors is required. All simulations in this chapter assume that the primary field comprises only of the modes of spinning mode order $m = m_B = EO$. In reality, this is not the case. The effect that noise and extraneous modes have on the control system will be assessed in Chapter 6.

Performance of the control system following the control of the single buzz-saw mode associated with $EO = 8$ i.e. $(m_B = 8, n = 1)$ will be quantified by computation of the sound power reduction. The results for this engine order have been found to represent the behaviour at all engine orders up to EO=14. In this frequency range only one radial mode order can propagate at each engine order. At higher engine orders the second radial mode order begins to cut-on. A control system with only a single ring of sources and sensors will be shown to be insufficient to independently control the sound field into separate radial orders. Poor control performance is therefore predicted at these higher frequencies. For engine orders below EO=5 the buzz-saw mode is cut-off. In the simulations reported here, the flow is assumed to have an axial flow Mach number M_x of -0.55 and a tip speed Mach number M_t equal to 1.05. Unless otherwise stated, the fan plane is positioned at $x = 0.6m$, the single ring of secondary sources is positioned at $x = 1m$ and the single ring of error sensors at $x = 1.24m$. The duct has a length of $1.84m$ and a radius of $0.4m$. The Mach numbers, the duct radius and the relative distances between the source and sensor rings in the inlet section are chosen to be similar to the original specifications of the expermental rig to be used by the SILENCE(R) partners in their tests on the scale model RACE rig [1]. At the time of writing, the length of the duct section was unclear and thus this dimension has been estimated. The geometry of the duct model is shown in figure 5.1.

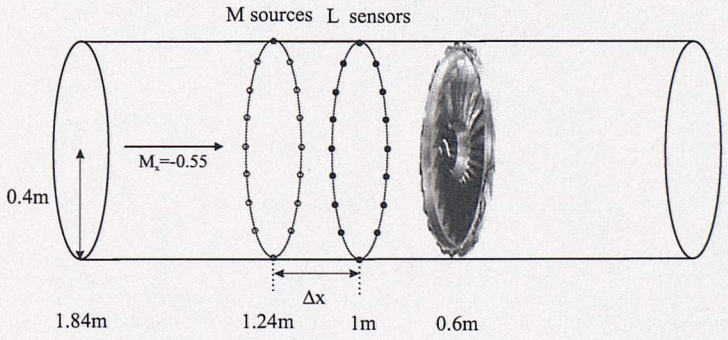

Figure 5.1: *Geometry and dimensions of the duct model (not to scale)*

[1]Note that the rig test has now been moved to ANECOM which at the time of writing had not yet begun.

5.2 Predicted performance for a control system with a single ring of sources and sensors

Figure 5.2 shows the sound power reduction predicted at each EO when minimising the sum of the square pressures at a single ring of 30 sensors using a single ring of 30 sources. The clear bars show the sound power level before control, and the solid bars show the resulting levels after control. The buzz-saw amplitude at the fan face before control a_{p0} (see chapter 3) was determined using the FDNS method developed by McAlpine and Fisher [42] using estimated data for the sound pressure levels at the fan face.

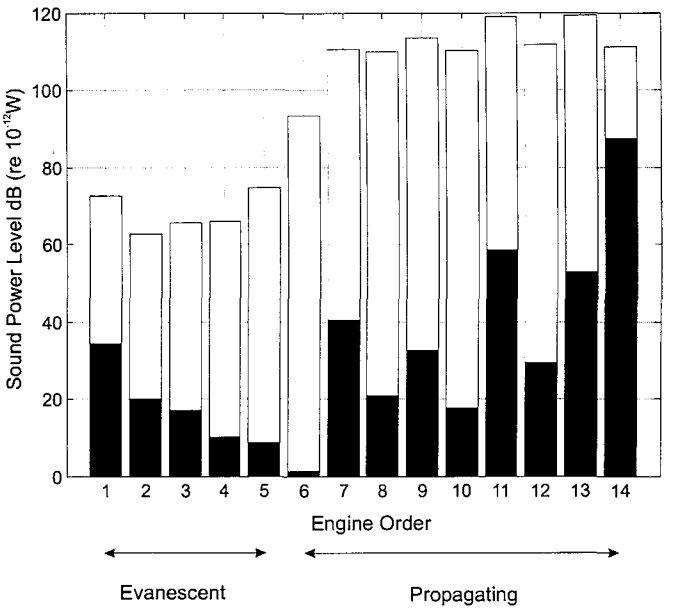

Figure 5.2: *Predicted Sound Power Reduction for EO=1-14 when minimising the sum of the square pressures in the absence of noise. The clear bars show the sound power level before control, and the solid bars show the resulting levels after control.*

In figure 5.2 the sound power reduction increases from EO=1 to 5. At this fan tip speed these buzz-saw tones are cut-off. The buzz-saw mode at EO=5 is the closest to cut-on (but still cut-off) and will have decayed by the least amount upon reaching the error sensor array. Control performance will therefore be greater for high cut-off engine orders than for low EO's. At EO=6 to 13, sound power reductions of 70 to 90dB are predicted in this

noise-free simulation. However, at EO=14, sound power is only reduced by between 10 and 15dB. This is because at this high engine order, the sources inadvertently excite the $m = -16$ mode, which is only just cut-off (following the Nyquist sampling theorem the 30 sources and sensors cannot independently control modes $|m| > 15$). Modal spillover at these high EOs will therefore considerably limit control performance, as observed in figure 5.2. The influence on control performance of modal spillover will be adressed later in this chapter.

In the following sections the performance of the active control system is investigated following the control of the single buzz-saw mode associated with $EO = 8$ i.e. $(m = 8, n = 1)$. Results at this EO have been found to be typical for all low frequency engine orders up to $EO = 14$ (See figure 5.2).

5.2.1 Numbers of sources and sensors required for effective active noise control.

This section will establish criteria for the number of sources and sensors required for the effective active control of buzz-saw tones obtained by minimising the sum of the square pressures at the error sensors.

Figures 5.3-5.5 illustrate, respectively, the variation of the sound power reduction, the mean squared volume velocity, and the sound pressure level reduction, with varying combinations of sources M and sensors L between 1 and 30. The distance between the source and sensor array was set to $\Delta x = 0.24m$.

Figures 5.3 and 5.4 suggest that the behaviour of the control system can be divided into four regions:

Region I - $L < 2m_{max} + 1$, $M < 2m_{max} + 1$. Region I encompasses all combinations of sources and sensors where both L and M fail to meet the Nyquist criterion of $2m_{max} + 1$ where m_{max} is the maximum spinning mode order at the frequency of interest [21]. The use of too few sources *and* sensors results in poor 'global' control performance with levels

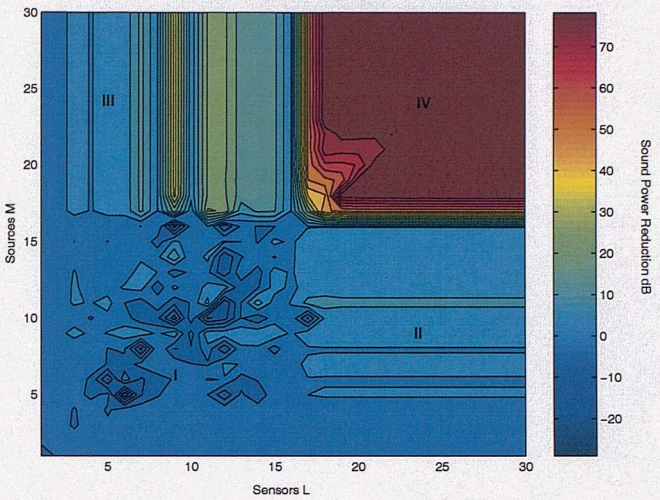

Figure 5.3: *Sound Power Reduction with varying numbers of sources M and sensors L*

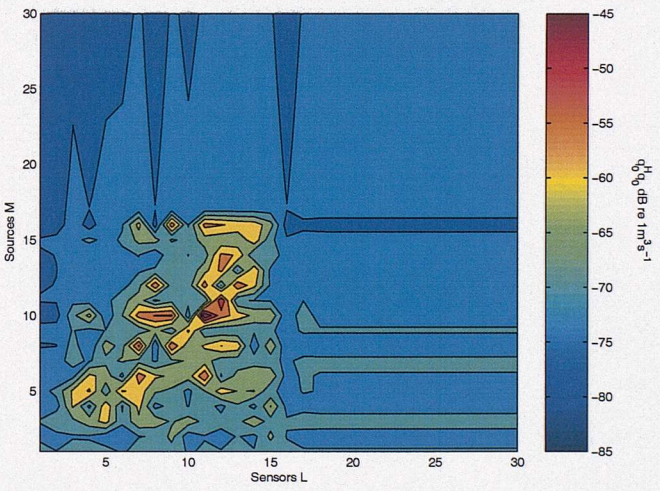

Figure 5.4: *Mean squared volume velocity for varying numbers of sources M and sensors L*

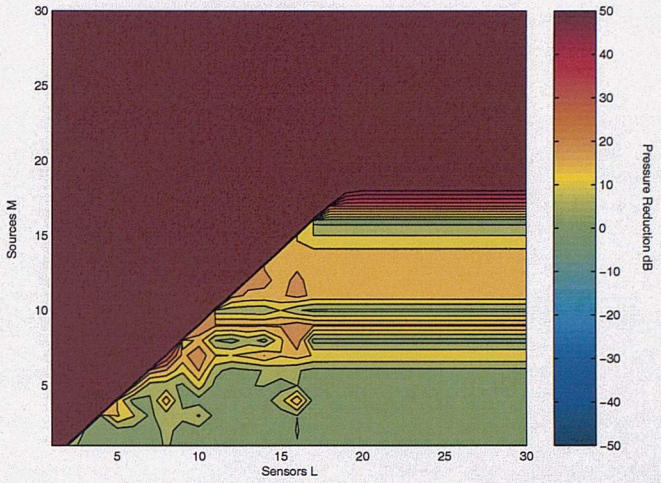

Figure 5.5: *Sound pressure level reduction at the error sensors with varying numbers of sources M and sensors L*

of sound power reduction varying from -3dB (corresponding to a power increase) to 3dB. It is clear from figure 5.5 that the pressure at the error sensors can be reduced by more than 50dB in the underdetermined case where there are more sources than sensors. However, in the overdetermined case $L > M$ it seems that with fewer sources than sensors the pressure reduction is poorer, varying from 10 to 15dB. The volume velocities tend to vary across this region from 45 to 70 dB re $1m^3s^{-1}$. Higher volume velocities are therefore the cause of an increase in sound power.

Region II - $L > M$, $L > 2|m_{max}|+1$, $M < 2|m_{max}|+1$. Region II contains combinations of sources and sensors that give small reductions in sound power and also relatively small reductions in sound pressure at the error sensors (figure 5.5). The power and pressure reductions improve slightly as the number of sources increase. The maximum reduction in this region is approximately 3dB. The number of sensors exceeds the Nyquist value, however, there are insufficient sources to control either the 'local' or 'global' sound fields to a large extent ('local' control is defined as the reduction the sound pressure at the error sensors). The Nyquist value is defined such that are at least 2 sensors for each period, thus it is equal to $2|m_{max}| + 1$ where m_{max} is equal to the highest propagating spinning mode order. Similarly to region I, it can be seen that with the number of sources less than the number of sensors, 'local' control performance is not as effective, despite the fact that

in this case the number of sensors satisfies the Nyquist criterion. This implies that both sources *and* sensors must satisfy the Nyquist criterion.

Region III - $L < M$, $L < 2|m_{max}| + 1$, $M > 2|m_{max}| + 1$. Here the number of sources satisfy the Nyquist criterion but the number of sensors does not. Throughout region III there are small reductions in sound power which are marginally larger than those in region II. The level of reduction varies between 0dB and 12dB, gradually increasing as the number of sensors approaches the Nyquist value. Figure 5.5 suggests that the reason for the higher levels of sound power reduction is that the pressure at the error sensors is more effectively minimised. It is clear that for all combinations where the number of sources exceeds the Nyquist value, there are good levels of both pressure and power reduction. The values of 'optimal' volume velocity do not vary greatly across this region.

Region IV - $L > 2|m_{max}| + 1$, $M > 2|m_{max}| + 1$. In Figure 5.3 Region IV displays significant reductions in sound power, that are in excess of 30dB for all combinations of sources and sensors. The sound pressure level at the error sensors is reduced by values in excess of 50dB across Region IV. In this region the number of sources exceed the Nyquist value and the number of sensors is greater than, or equal to, this value. The volume velocity from Figure 5.4 is fairly constant across this region. An interesting feature present in figure 5.3 for the sound power reduction is that it increases slowly, reaching a maximum value for $M > 20$ and $L > 20$. This is because at combinations of sources and sensors that are equal to, or just greater than $2|m_{max}| + 1$, the mode amplitudes are not fully driven to zero, but are excited such that their sum is zero. A more realistic sampling criterion in order to guarantee global control of the sound field would be to ensure that the number of sources and sensors exceeds $2|m_{max}| + 3$.

5.2.2 Modal spillover

Further examination of the source-sensor combinations where the number of sources and sensors are equal to or close to $2|m_{max}| + 1$ shows that the sound power reduction is not as significant as when the number of sources and sensors are much greater than $2|m_{max}| + 1$.

Much higher levels of sound power reduction are observed where the number of sources and sensors are significantly greater than $2|m_{max}|+1$. If the control system only just meets the sampling criterion for sources and sensors, then any inadvertently excited modes with a higher spinning mode order cannot be controlled. The aim of the control system is to drive the pressure to zero, and this can only be achieved by exciting modes that the control system can sample such that they cancel with those that it cannot detect and control. This effect is known as modal spillover.

At the engine order of interest EO=8, the spinning mode $m = 9$ is very close to cut-on having a cut-off ratio of $\zeta \approx 0.9$ at $M_t = 1.05$. With the source and sensor array separation at only $0.24m$ this evanescent mode will have a significant amplitude at the sensor array. Attempts by a control system which only has numbers of sources and sensors equal to $2|m_{max}| + 1$ to control this mode will cause this evanescent mode to be aliased into the lower order modes. Figure 5.5 shows that with this combination of sources and sensors, the pressure is driven to zero. The sound power reduction, however is not as large. This can be explained by examining the relationship between the pressure and the mode amplitudes at the duct wall.

The control system seeks to drive the sum of the squared pressures measured at the error sensors to zero. The pressure at the lth sensor position can be expressed as the sum of the spinning mode amplitudes $\hat{a}_m$ at the duct wall,

$$p(\theta_l) = \sum_m \hat{a}_m e^{im\theta_l} \tag{5.1}$$

where each $\hat{a}_m$ comprises a sum of radial modes,

$$\hat{a}_m = \sum_n a_{m,n} \Psi_{m,n}(a) \tag{5.2}$$

where $a_{m,n}$ is the modal amplitude of the (m,n)th mode defined in chapter 2.

Assuming that there are a sufficient number of error sensors, one can obtain the values of

the amplitudes of the spinning modes after control by performing a spatial discrete Fourier transform of the pressure measurements at the duct wall,

$$\hat{a}_m = \frac{1}{L}\sum_{l=1}^{L} p(\theta_l)e^{-im\theta_l} \qquad \left(\frac{-(L-1)}{2} \leq m \leq \frac{L-1}{2}\right) \tag{5.3}$$

If the pressure is driven to zero at the error sensors,

$$p(\theta_l) = 0 \tag{5.4}$$

and as long as the number of sensors exceeds the number required to satisfy the Nyquist criterion of $L \geq 2|m_{max}|+1$ then equation 5.4 indicates that the individual spinning mode orders will also be driven to zero, i.e.

$$\hat{a}_m = 0 \qquad \left(\frac{-(L-1)}{2} \leq m \leq \frac{L-1}{2}\right) \tag{5.5}$$

Essentially therefore, if there is a sufficient number of sensors the control system is decoupled in as much as the spinning mode amplitudes are independently driven to zero.

In the present case of EO=8, with a single propagating mode present with $m_B = 8$, then this spinning mode order will be driven to zero if the number of sensors exceeds 15. As control occurs only in the spinning mode order $m = m_B = 8$, then this is the only mode which will carry sound power. Substantial sound power reductions are therefore predicted in this case. However, if there is significant contribution from the evanescent mode $m = m_B+1$, there will need to be sufficient sensors to observe this higher mode order and hence avoid aliasing into lower order spinning modes. This effect is seen in figure 5.3 to a greater extent when the number of sources is less than required to observe unambiguously the propagating buzz-saw mode. In this case the pressure is reduced to zero, however the propagating mode is aliased into the lower spinning mode order amplitudes by the sensor array. Sound power is therefore not significantly reduced.

5.2.3 The effect of source-sensor array separation distance on active control performance.

The model described in Chapter 3 was used to predict the variation in sound power reduction at EO=8 with separation distance Δx between the source and sensor rings. The results are shown in Figure 5.6 for a single ring of 30 sources and a single ring of 30 sensors. In the simulation the source array was kept at a fixed axial position whilst the sensor position was varied.

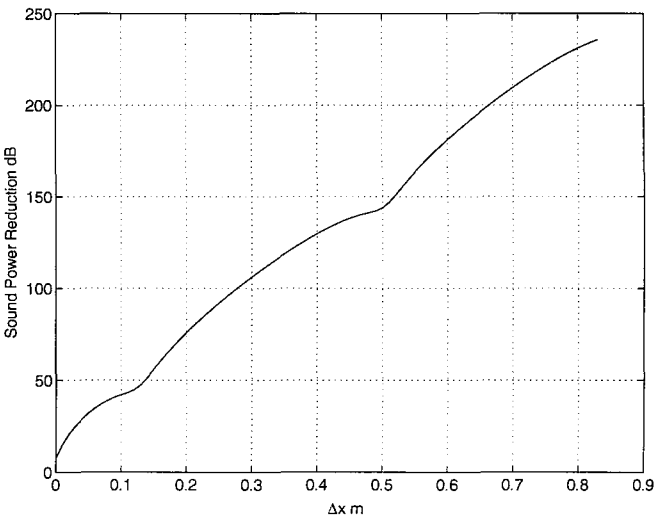

Figure 5.6: *Sound Power Reduction with varying source sensor separation distance Δx at EO=8 for a single ring of 30 sources and 30 sensors*

The variation in sound power reduction is shown to increase dramatically with increasing separation distance Δx. In this example, the reduction improves at a rate of approximately 250dBm^{-1}.

There are kinks in the curve at values of Δx approximately equal to 0.1m and 0.5m. An explanation for this phenomenon is given in figure 5.7. The upper plot shows the axial pressure variation of the buzz-saw tone through the duct. The lower plot is a repetition of figure 5.6 for the sound power reduction versus Δx. The vertical line in figure 5.7 shows the position of the secondary source array in the duct.

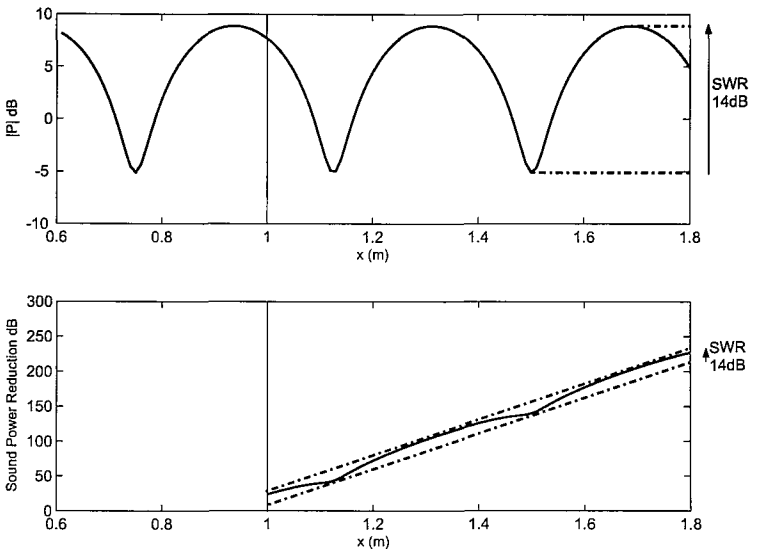

Figure 5.7: *Primary pressure variation within the inlet duct and sound power reduction with varying source sensor separation distance* Δx

An exact correspondence is observed between the minima in the primary field and the kinks in the graph of SPL reduction versus Δx. Figure 5.7 shows that at these axial locations, the source array is situated on a pressure minimum of the axial standing wave field set up between the duct terminations (assuming no blockage by the rotor). At these positions the actuators cannot couple as well into the mode as at other positions, and thus control performance drops. An exact correspondence is also observed between the maximum departure from straight-line behaviour and the standing wave ratio of the primary sound field, as indicated in figure 5.7 by the dashed lines. A 14dB deviation is observed in both figures 5.7(a) and 5.7(b). An analytic model which predicts this behaviour is presented in section 5.2.4

Further insight into the control mechanism following pressure minimisation is obtained by examining the individual mode pressure amplitudes after control. This is shown in figure 5.8(a) following control of the buzz-saw mode (8,1), normalised on the amplitude $|a_{p_{m_B,1}}|$ of the primary mode.

The sum of the squared pressures at the error sensors after control relative to $|a_{p_{m_B,1}}|^2$ is predicted to be of the order of 10^{-28}. Figure 5.8(a) shows that to achieve this reduction,

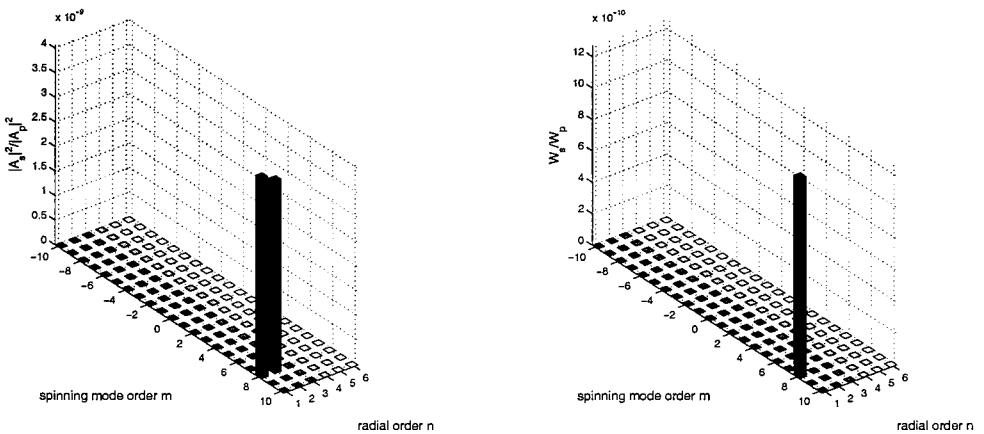

(a) (b)

Figure 5.8: *Modal amplitude (a) and modal power (b) distributions after control following minimisation of the sum of the square pressures at the error sensors*

the secondary sources have excited, not only the propagating buzz-saw mode, but also the second radial mode $n = 2$ associated with $m = 8$, which is cut-off. Since the mean square pressure mode amplitudes after control are nineteen orders of magnitude greater than the mean square pressure at the error sensors, the two modes $(8, 1)$ and $(8, 2)$ must be excited very nearly in anti-phase to achieve this level of reduction. This finding is consistent with equations 5.5 and 5.6 which predict that $\hat{a}_8 = \hat{a}_{8,1} + \hat{a}_{8,2} = 0$. As the propagating mode carries substantially more power than the evanescent mode, as shown in figure 5.8(b), the amplitude of the evanescent modes at the sensor array therefore imposes a fundamental limit on the maximum sound power reduction in the absence of noise or extraneous modes. An analytic model for predicting the power reduction based on this control principle is now discussed.

An identical control principle is described by Elliott and Billet [15] in the control of a single flexural wave in slender beams in the presence of a single evanescent wave. They show that the fundamental limit of control performance for vibrational power flow is determined by the amplitudes of the evanescent wave at the error sensors excited by the secondary sources after control.

5.2.4 Analytical model of the maximum sound power reduction

It was argued in the previous section that in the hypothetical noise-free control system the amplitude of evanescent modes at the error sensor array fundamentally limits the sound power reduction following active noise control obtained by pressure minimisation. In this section we shall use this finding to formulate an analytical model for the maximum sound power reduction. In the model we make the following assumptions:

(i) The sound field cannot be resolved into its separate radial mode orders by the single ring of sensors.

(ii) Providing that sufficient source and sensors are used in a single ring (section 5.2.1) the secondary source ring will only excite radial modes at $m = m_B$, including evanescent modes.

(iii) For $L = M$ the pressure is driven to zero at the error sensors. This is a valid assumption as the overall pressure after control is typically in excess of 100dB below that of the primary pressure in this noise-free simulation.

Assuming (i)-(iii) above, and setting the total pressure at the lth error sensor to zero $p(\theta_l) = 0$ gives

$$\left[a_{p_{m_B,1}}(x_e) + a_{s_{m_B,1}}(x_e)\right] \psi_{m_B,1}(a) e^{im_B\theta_l} + \sum_{n=2}^{\infty} \left[a_{p_{m_B,n}}(x_e) + a_{s_{m_B,n}}(x_e)\right] \psi_{m_B,n}(a) e^{im_B\theta_l} = 0 \tag{5.6}$$

where $\psi_{m_B,n}$ is the mode shape function for the mode (m_B, n), defined in chapter 3,

$$\psi_{m_B,n}(r,\theta_l) = \Psi_{m_B,n}(r) e^{im_B\theta_l} \quad ; \quad \Psi_{m_B,n}(r) = \frac{J_m\left(k_{r_{m_B,n}} r\right)}{N_{m_B,n}} \tag{5.7}$$

Note that in equation 5.6 the primary and secondary fields have been split into the propagating buzz-saw mode $a_{m_B,1}\psi_{m_B,1}$ and non-propagating evanescent modes $a_{e_{m_B,n}}\psi_{m_B,n}$

($n > 1$). The distance between the fan and the sensor array is generally much greater than the distance between the secondary sources and the sensor array. The amplitudes of the evanescent modes excited by the primary field decay to a much lower amplitude than the evanescent modes excited by the secondary sources. The amplitudes of the evanescent modes excited by the fan can therefore be neglected, but those excited by the secondary sources cannot.

The amplitude of the secondary propagating mode $a_{s_{m_B,1}}$ at the error sensor following cancellation of the pressure at the error sensors is therefore given by

$$a_{s_{m_B,1}}(x_e) = -a_{p_{m_B,1}}(x_e) + \frac{1}{\Psi_{m_B,1}(a)} \sum_{n=2}^{\infty} a_{s_{m_B,n}}(x_e)\Psi_{m_B,n}(a) \tag{5.8}$$

Note that the term $e^{im_B\theta_l}$ describing the circumferential variation of pressure cancels in equation 5.8 suggesting that $a_{m_B} = 0$ and hence the secondary mode amplitude is independent of the sensor azimuthal position. This result is consistent with the equation 5.6 obtained from the DFT argument proposed in 5.2.2. The total amplitude $a_{m_B,1}$ of the buzz-saw mode after control is therefore given by

$$a_{m_B,1}(x_e) = a_{p_{m_B,1}}(x_e) + a_{s_{m_B,1}}(x_e) = -\frac{\sum_{n=2}^{\infty} a_{s_{m_B,n}}(x_e)\Psi_{m_B,n}(a)}{\Psi_{m_B,1}(a)} \tag{5.9}$$

which is only determined by the mode amplitudes of the cut off modes at the error sensors. Assuming that the power carried by the cut-off modes can be neglected, the maximum theoretical sound power reduction at the error sensors after control is given by

$$\frac{W_o(x_e)}{W_p(x_e)} = \frac{\gamma_{m_B,1}(x_e)|a_{m_B,1}(x_e)|^2}{\gamma_{m_B,1}(x_e)|a_{p_{m_B,1}}(x_e)|^2} = \frac{\left|\sum_{n=2}^{\infty} a_{s_{m_B,n}}(x_e)\Psi_{m_B,n}(a)\right|^2}{\left|a_{p_{m_B,1}}(x_e)\Psi_{m_B,1}(a)\right|^2} \tag{5.10}$$

Further assuming that the cut-off mode $(m_B, 2)$ excited by the secondary sources is the dominant evanescent mode, the sound power level reduction in decibels (defined to be

> 0) is given by

$$\Delta SWL(x_e) = -10\log_{10}\left(\frac{\left|a_{s_{m_B,2}}(x_e)\Psi_{m_B,2}(a)\right|^2}{\left|a_{p_{m_B,1}}(x_e)\Psi_{m_B,1}(a)\right|^2}\right) \qquad (dB) \tag{5.11}$$

In Chapter 3, we showed that the amplitude $a_{p_{m_B,1}}$ of the primary buzz-saw mode at x_e is given by

$$a_{p_{m_B,1}}(x_e) = \frac{a_{p_0}(x_f)ie^{i\phi^-(x_f)}\sec\phi^-_{m_B,1}(x_f)}{(\tan\phi^+_{m_B,1}(x_f) - \tan\phi^-_{m_B,1}(x_f))}\frac{\cos\phi^+_{m_B,1}(x_e)}{\cos\phi^+_{m_B,1}(x_f)}e^{\frac{-iM_xk(x_e-x_f)}{1-M_x^2}} \tag{5.12}$$

where $a_{p_0}(x_f)$ is the pressure amplitude of the primary buzz-saw mode at the source plane in the absence of reflections and $\phi^{\pm}_{m_B,n}$ are the complex reflectivity factors deduced from the modal reflection coefficients at the terminations $R^{\pm}_{m_B,n}$ from the expressions given previously in chapter 3,

$$\phi^+_{m,n}(x_e) = \frac{\ln R^+_{m,n}}{2i} + \frac{\alpha_{mn}k(L-x_e)}{1-M_x^2} \tag{5.13}$$

$$\phi^-_{m,n}(x_e) = \frac{-\ln R^-_{m,n}}{2i} + \frac{\alpha_{mn}k(-x_e)}{1-M_x^2} \tag{5.14}$$

From Chapter 3 the amplitude of the evanescent mode $a_{m_B,2}$ at the error sensor array x_e due to M secondary sources is of the form

$$a_{m_B,2}(x_e) = \frac{i\rho c_0}{S}\sum_{m=1}^{M}\frac{q(\theta_{s_m})\,\psi^*_{m_B,2}(r_s,\theta_{s_m})}{\alpha_{m_B,2}(\tan\phi^+_{m_B,2}(x_{s_m}) - \tan\phi^-_{m_B,2}(x_{s_m}))}\frac{\cos\phi^+_{m_B,2}(x_e)}{\cos\phi^+_{m_B,2}(x_{s_m})}e^{\frac{-ikM_x(x_e-x_{s_m})}{1-M_x^2}} \tag{5.15}$$

The ratio of cosine terms in equation 5.12 describes the oscillatory nature of the axial pressure distribution due to the buzz-saw mode in the duct due to standing waves caused by reflection between the inlet and exhaust termination. In the case of the evanescent

mode, this term in equation 5.15 describes the decay of the mode in the axial direction. To show this behaviour explicitly, it is written in full as

$$\frac{\cos\phi^{+}_{m_B,2}(x_e)}{\cos\phi^{+}_{m_B,2}(x_s)} = \frac{e^{i\left((\phi_R+i\phi_I)-\frac{\alpha_{m_B,2}kx_e}{1-M_x^2}\right)} + e^{-i\left((\phi_R+i\phi_I)-\frac{\alpha_{m_B,2}kx_e}{1-M_x^2}\right)}}{e^{i\left((\phi_R+i\phi_I)-\frac{\alpha_{m_B,2}kx_s}{1-M_x^2}\right)} + e^{-i\left((\phi_R+i\phi_I)-\frac{\alpha_{m_B,2}kx_s}{1-M_x^2}\right)}} \tag{5.16}$$

where $\phi^{+}_{0_{m_B,n}} = \phi_R + i\phi_I$ is the complex reflectivity factor evaluated at the inlet termination $x = L$.

For the evanescent mode $(m_B, 2)$ the imaginary part ϕ_I of the reflectivity factor is generally much greater than the real part ϕ_R. The first exponential term in the numerator and denominator of equation 5.16 will therefore be negligible compared to the second terms on the top and bottom. In the limit as $R_{m,n} \to 0$ the imaginary part of the reflectivity factor tends to infinity, and equation 5.16 tends to

$$\lim_{R_{m,n}\to 0} \frac{\cos\phi^{+}_{m_B,2}(x_e)}{\cos\phi^{+}_{m_B,2}(x_s)} = e^{\frac{i\alpha_{m_B,n}k(x_e-x_s)}{1-M_x^2}} \tag{5.17}$$

As the $(m_B, 2)$ mode is cut-off, $\alpha_{m_B,2}$ is purely imaginary, and the above expression is equal to $e^{\Im\{k^{+}_{x_{m,n}}\}(x_e-x_s)}$, where $k^{+}_{x_{m,n}}$ is the axial wavenumber of the forward propagating mode given by

$$k^{+}_{x_{m_B,2}} = \frac{\alpha_{m_B,2} - M_x}{1 - M_x^2} \tag{5.18}$$

When equations 5.12 and 5.15 are combined, equation 5.11 may be written as

$$\Delta SWL(x_e) = \Delta SWL(x_s) - 8.7\Im\left\{k_{x_{m_B,2}}\right\}(x_e - x_s) + 10\log_{10}\left|\frac{\cos^2\phi^{+}_{m_B,1}(x_e)}{\cos^2\phi^{+}_{m_B,1}(x_f)}\right| \tag{5.19}$$

The term $\Delta SWL(x_s)$ is the sound power reduction for the case when the source and sensors have zero separation distance, $x_s = x_e$. From equation 5.11, it is equal to

$$\Delta SWL(x_s) = -10\log_{10}\left(\frac{|a_p(x_s)\Psi_{m_B,1}(a)|^2}{|a_e(x_s)\Psi_{m_B,2}(a)|^2}\right) \tag{5.20}$$

Equation 5.19 describes the variation of sound power reduction with varying source-sensor separation distance $\Delta x = x_e - x_s$. The second term on the right hand side of equation 5.19 describes the overall decay rate in figure 5.6, and is the dominant term. It shows that the gradient of the overall behaviour of the graph is exactly equal to the decay rate of the most significant evanescent mode. In this case, this is the second radial mode order at $m = m_B$.

The last term in equation 5.19 describes the oscillations in figure 5.6. By comparison with equation 5.12 this ratio of cosine terms describes the standing wave behaviour of the primary buzz-saw field. By finding the minimum values of this term one can determine the axial positions x_q from the 'exhaust' termination of the kinks in sound power reduction. The minimum value will occur where $\cos\phi^+_{m_B,1}(x_q) = 0$, corresponding to $\Re\left\{\phi^+_{m_B,1}(x_q)\right\} = (2q+1)\pi/2$. Solving for x_q, the position of the dips in figure 5.6 occur at

$$x_q = \frac{\left[-(2q+1)\pi/2 + \Re\left\{\phi^+_{0_{m_B},1}\right\}\right](1-M_x^2)}{\alpha_{m_B,1}k} \tag{5.21}$$

where $\phi^+_{0_{m_B},1}$ is the complex reflectivity factor evaluated at the inlet termination L. For $q = 1, 2$, the equation yields x_q values of 1.50m and 1.13m. These are the axial positions of the sensor array relative to the source position at 1m. This results in separation distances of 0.13m and 0.50m, which agrees closely with the dips observed in figure 5.6.

As demonstrated in figure 5.7, comparison of equation 5.19 with 5.12 shows that the maximum variation in power reduction in figure 5.6 from straight-line behaviour is identical to the standing wave ratio (SWR) of the primary field shown in figure 5.7. For the simulation under investigation here, $SWR \approx 14dB$.

Comparison between the power reduction predicted from the analytic expression of equation 5.9 and the exact calculation shown in figure 5.6 is shown in figure 5.9 below for

varying Δx. Excellent agreement is observed for $\Delta x > 0.1m$. Below this value of the separation distance the assumption that the second radial mode is the most significant evanescent mode breaks down and thus the model incorrectly predicts the sound power reduction.

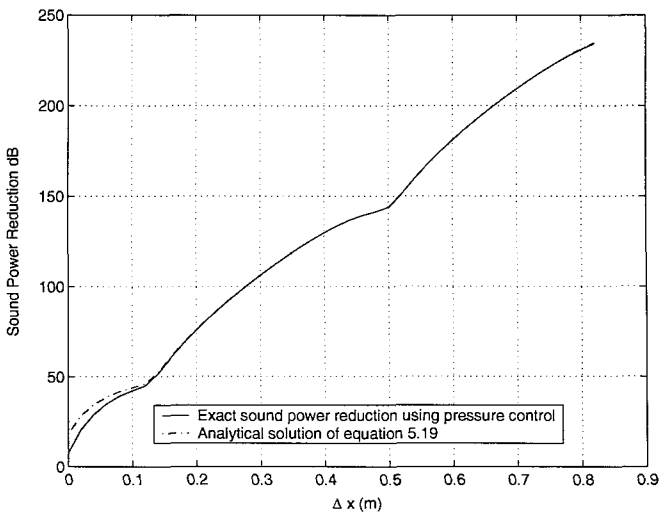

Figure 5.9: *Comparison of sound power reduction at EO=8 for varying separation distances obtained using the analytical model of equation 5.19 and the exact calculation*

5.2.5 Control performance versus engine speed

It was noted in Chapter 2 that in a hard-walled duct the buzz-saw field cuts-on abruptly as the tip speed exceeds a critical value above the speed of sound, and that each buzz-saw mode in each EO has a similar cut-off ratio $\zeta_{m,n}$, which is typically only slightly greater than unity. It has been shown in Chapter 3 that the modal reflection coefficients at frequencies close to the cut-off frequency are close to unity and that strong standing waves are set up in the duct (in the absence of blockage by the rotor and stator). In order to assess how engine speed, and hence standing wave behaviour, affects active control performance, the tip speed of the fan in the simulations was varied such that the frequency was taken through the buzz-saw mode cut-off frequency. The results of this simulation are shown in figure 5.10 using the same duct geometry and control system as that discussed in section 5.1. The sound power in the inlet duct, both before and after control, was then

plotted against the cut-off ratio $\zeta_{m,n}$ of the $m_B = 8$ buzz-saw mode (and the blade tip mach number M_t on another axis below it). It is assumed that $M_x = -0.52M_t$, from known values of M_x and M_t in the SILENCE(R) RACE rig.

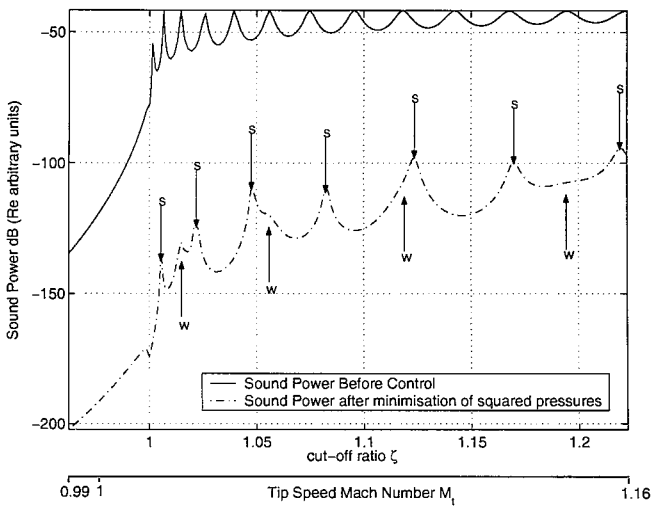

Figure 5.10: *Active control performance with varying tip speed for a single ring of 30 sources and 30 sensors at EO=8. The arrows indicate the family of strong (s) and weak (w) resonances after control*

The sound power 'spectrum' of the primary buzz-saw field (solid curve) comprises resonances due to the presence of axial standing waves between the reflective terminations of the duct. These resonant frequencies can be determined by setting the denominator of equation 3.11 for the primary pressure, equal to zero.

As M_t increases, and hence frequency increases, the resonant frequency bandwidth of the sound power reduction becomes broader. This is because, as frequency increases from cut-off, the reflection coefficients become smaller and hence more energy escapes from the duct. Thus the resonances become increasingly damped through radiation damping as tip speed increases.

After control, the resonant peaks in the sound power variation with varying tip speed M_t (dashed curve) have markedly shifted. A number of authors [12, 45] have also noted that controlling axial standing waves in a duct causes the introduction of other resonant frequencies in the acoustic response. This observation is now explored and the frequencies

of these spectral peaks predicted using the analytical model of equation 5.11.

If we assume that the most significant evanescent mode at the error sensors is the mode $(m_B, 2)$, then from equation 5.9 the power after control at the error sensors is

$$W(x_e) = \gamma_{m_B,1}(x_e) \left| \frac{a_{m_B,2}(x_e)\Psi_{m_B,2}(a)}{\Psi_{m_B,1}(a)} \right|^2 \tag{5.22}$$

We now introduce a modal secondary source strength Q_m, defined as the mth Fourier component of the secondary source ring $q(\theta_m)$,

$$Q_m = \frac{1}{M} \sum_{m=1}^{M} q(\theta_m) e^{-im\theta_m} \tag{5.23}$$

Equation 5.23 is now used to re-write equation 5.15 for the amplitude of the mode $(m_B, 2)$ excited by the secondary sources as

$$a_{m_B,2}(x_e) = Q_{m_B} z_{m_B,2}(x_s, x_e) \tag{5.24}$$

Where from equation 4.2 $z_{m,n}$ is a spinning mode transfer impedance defined by

$$z_{m,n}(x_s, x_e) = \frac{i\rho c_0 \Psi^*_{m,n}(a)}{S\alpha_{m,n}(\tan\phi^+_{m,n}(x_s) - \tan\phi^-_{m,n}(x_s))} \frac{\cos\phi^+_{m,n}(x_e)}{\cos\phi^+_{m,n}(x_s)} e^{\frac{-ikM_x(x_e - x_s)}{1-M_x^2}} \tag{5.25}$$

We have shown in section 5.2.2 that if there are sufficient sources and sensors and the pressure is driven to zero then the spinning mode amplitudes are also zero. When only the single spinning mode $m = m_B$ is present, this amplitude is equal to the propagating primary buzz-saw mode and the secondary sound field is the sum of the propagating $(m_B, 1)$ mode and the evanescent $(m_B, 2)$ mode. The primary and secondary source contributions to $m = m_B$ can be expressed in a similar form to equation 5.24. By substituting equation 5.24 into equation 5.6 and neglect of the evanescent modes in the primary field, the pressure at the error sensors can therefore be expressed as

$$a_{p_{m_B,1}}(x_e)\Psi_{m_B,1}(a) + Q_{m_B}\left(z_{m_B,1}(x_s,x_e)\Psi_{m_B,1}(a) + z_{m_B,2}(x_s,x_e)\Psi_{m_B,2}(a)\right) = 0 \quad (5.26)$$

where the term $e^{im_B\theta_l}$ has been cancelled. Solving for the modal source strengths gives

$$Q_{m_B} = \frac{-a_{p_{m_B,1}}(x_e)\Psi_{m_B,1}(a)}{z_{m_B,1}(x_s,x_e)\Psi_{m_B,1}(a) + z_{m_B,2}(x_s,x_e)\Psi_{m_B,2}(a)} \quad (5.27)$$

Combining equations 5.27, 5.24 and 5.22, the expression for the sound power after control is given by

$$W = \gamma_{m_B,1}(x_e)\left|\frac{a_{p_{m_B,1}}(x_e)z_{m_B,2}(x_s,x_e)\Psi_{m_B,2}(a)}{z_{m_B,1}(x_s,x_e)\Psi_{m_B,1}(a) + z_{m_B,2}(x_s,x_e)\Psi_{m_B,2}(a)}\right|^2 \quad (5.28)$$

In general, the pressure at the error sensors due to the cut-off mode $(m_B, 2)$ is much less than that due to the buzz-saw mode, so that $z_{m_B,2}(x_s,x_e)\Psi_{m_B,2}(a) << z_{m_B,1}(x_s,x_e)\Psi_{m_B,1}(a)$. For convenience we denote $z_{m_B,2}(x_s,x_e)\Psi_{m_B,2}(a)$ by $\epsilon(x_s,x_e)$ to denote a small quantity, to give

$$W(x_e) = W_p(x_e)\left|\frac{\epsilon(x_s,x_e)}{z_{m_B,1}(x_s,x_e)\Psi_{m_B,1}(a) + \epsilon(x_s,x_e)}\right|^2 \quad (5.29)$$

Given that ϵ is small, equation 5.29 for the power after control approximates further to

$$W(x_e) = W_p(x_e)\left|\frac{\epsilon(x_s,x_e)}{z_{m_B,1}(x_s,x_e)\Psi_{m_B,1}(a)}\right|^2 \quad (5.30)$$

Recalling that W_p is the sound power in the duct before control ,$W_p = |a_{p_{m_B,1}}|^2\gamma_{m_B,1}$, the primary mode pressure amplitude $a_{p_{m_B,1}}$ may be obtained by re-arranging equation 5.12 to give an expression whose denominator is independent of source position x_f.

$$a_{p_{m_B,1}}(x_e) = \frac{a_{p_{0_{m_B,1}}}(x_f) i e^{i\phi^-_{m_B,1}(x_f)} \cos\phi^+_{m_B,1}(x_e) e^{\frac{-ikM_x(x_e-x_f)}{1-M_x^2}}}{\sin(\phi^+_{0_{m_B,1}} - \phi^-_{0_{m_B,1}})} \tag{5.31}$$

The expression for the buzz-saw mode transfer impedance $z_{m_B,1}$ can be written in a similar way. Re-arranging 5.25 gives

$$z_{m_B,1} = \frac{i\rho c_0 \Psi^*_{m_B,1}(a) \cos\phi^+_{m_B,1}(x_e) \cos\phi^-_{m_B,1}(x_s)}{S\alpha_{m_B,1} \sin(\phi^+_{0_{m_B,1}} - \phi^-_{0_{m_B,1}})} e^{\frac{-ikM_x(x_e-x_s)}{1-M_x^2}} \tag{5.32}$$

Substituting equations 5.31 and 5.32 into 5.30 gives the following simple result for the sound power after control, expressed in non-dimensional form,

$$\frac{W(x_e)}{\frac{S}{\rho c_0}|a_{p_{0_{m_B,1}}}|^2} = \frac{S\gamma_{m_B,1}(x_e)|\epsilon(x_s,x_e)|^2}{\rho c_0 |\Psi_{m_B,1}(a)|^2} |\alpha_{m_B,1}|^2 \frac{\left|e^{i\phi^-_{m_B,1}(x_f)}\right|^2}{\left|\cos\phi^-_{m_B,1}(x_s)\right|^2} \tag{5.33}$$

Equation 5.33 predicts two families of resonances in the duct after control. One is a set of strong resonances (i.e. those with distinct peaks marked 's' in figure 5.10), the other are much more difficult to observe, and is referred to here as "weak", denoted by 'w' in figure 5.10.

'Strong Resonances'

The strongest resonances, after control, are associated with frequencies for which the term in the denominator in equation 5.33, $\left|\cos\phi^-_{m_B,1}(x_s)\right|^2$, takes minimum values. These frequencies, $k_q = \omega_q/c$ can be deduced from the frequency at which the real part of $\phi^-_{m_B,1}(x_s)$ is equal to $(2q+1)\pi/2$, where $q = 0, 1, 2\ldots$. Thus strong axial resonances occur when

$$\Re\left\{\phi^-_{m_B,1}(x_s)\right\} = \Re\left\{\phi^-_{0_{m_B,1}} + \frac{\alpha_{m_B,1} k_q(-x_s)}{1-M_x^2}\right\} = (2q+1)\frac{\pi}{2} \tag{5.34}$$

By inspection, equation 5.34 may be seen to express the condition for resonance of the $(m_B, 1)$ mode due to reflection between the source plane x_s and the exhaust termination at $x = 0$. Note that $\phi_{0_{m_B,1}}$ is the reflection phase at the exhaust termination and is a function of frequency. The resonance condition of equation 5.34 was verified by plotting the sound power before and after control versus $\Re\left\{\phi^-_{m,n}(x_s)\right\}/\pi$. Resonant frequencies $k_q = \omega_q/c$ are observed in figure 5.11 to correspond to values of $\Re\left\{\phi^-_{m,n}(x_s)\right\}/\pi = (2q+1)/2$ where $q = 0, 1, 2 \ldots$.

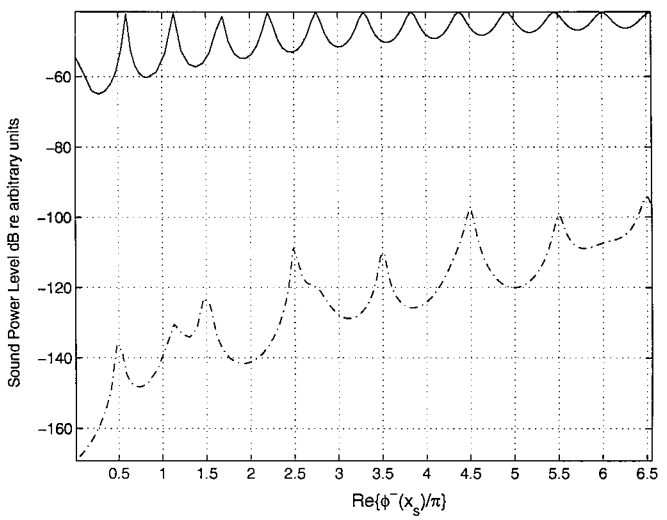

Figure 5.11: *The frequencies of the strong resonances in the power spectrum after control. The solid line shows the sound power level before control, and the dotted line shows the sound power level after control*

'Weak Resonances'

In addition to the strong resonance behaviour discussed above, there is a class of weaker resonances which are excited following active control after steady state conditions have been achieved. They occur most prominently at $\zeta = 1.02$ and 1.055 in figure 5.6. Inspection of equation 5.33 for the sound power after control reveals an additional, much weaker set of resonances, compared to those associated with equation 5.34. We have seen in the previous sections that the buzz-saw mode amplitude is only reduced to the level of the second evanescent radial mode. These resonances occur as a consequence of this residual

mode amplitude. Their frequencies can be determined from the maxima of the power factor $\gamma_{m_B,1}(x_e)$. The power factor $\gamma_{m_B,1}(x_e)$, from equation 4.8, contains the factor $\tan\phi^+_{m,n}$. Thus the condition for the weak resonances to occur is $\Re\left\{\phi^+_{m,n}(x_e)\right\} = (2q+1)\pi/2$ where $q = 0, 1, 2 \ldots$.i.e.

$$\Re\left\{\phi^+_{m_B,1}(x_e)\right\} = \Re\left\{\phi^+_{0_{m_B,1}} + \frac{\alpha_{m_B,1}k_q(L-x_e)}{1-M_x^2}\right\} = (2q+1)\frac{\pi}{2} \tag{5.35}$$

By inspection, equation 5.35 describes the condition for resonance of the buzz-saw mode reflecting between the sensor array x_e and the inlet termination $x = L$. Figure 5.12 shows the sound power before and after control versus $\Re\left\{\phi^+_{m_B,1}(x_e)\right\}/\pi$. Once again, the resonant frequencies $k_q = \omega_q/c$ correspond to values of $\Re\left\{\phi^+_{m,n}(x_e)\right\}/\pi = (2q+1)/2$, where $q = 0, 1, 2 \ldots$.

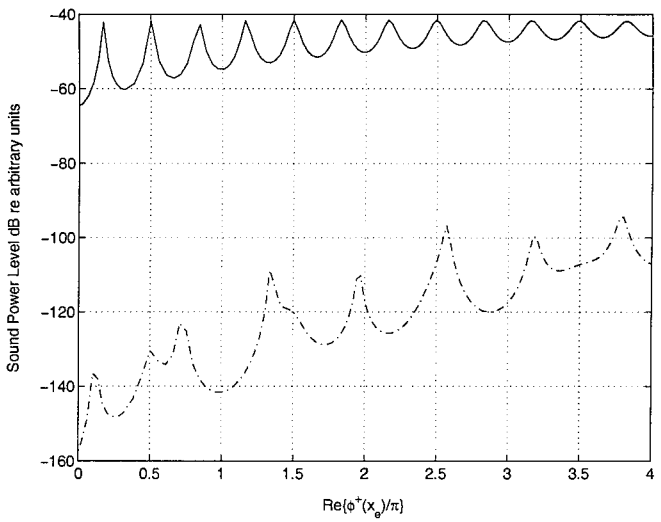

Figure 5.12: *The frequencies of the 'weak resonances' in the power spectrum after control. The solid line shows the sound power level before control and the dotted line shows the sound power level after control*

Note that the 'weak' resonances for $q > 2$ are masked by the strong resonances.

5.2.6 Control mechanism

In the previous section two classes of resonance were identified. One corresponds to standing waves between the source array and the exhaust termination, the other between the sensor array and the inlet termination. In this section the control mechanism in the time domain, which leads to their formation, will be described.

Figure 5.13 illustrates the control mechanism in the time domain by representing the buzz-saw mode as a pulse launched from the primary source at $t = -(x_s - x_f)/c$. The time-evolution of this pulse is now described in an attempt to explain the standing wave behaviour observed in figure 5.10.

a) A buzz-saw mode is radiated forward of the fan at $t = -(x_s - x_f)/c$ (at position x_f) *only* and travels toward the secondary sources.

b) At time $t = 0$ the buzz-saw mode reaches the secondary source array (at position x_s). The secondary source generates a mode of equal amplitude and opposite phase in both directions down the duct. The forward wave partially cancels with the buzz-saw mode due to the presence of the second evanescent mode at the error sensor array, whereas the backward propagating mode is unattenuated.

c) The residual waves travel toward the terminations.

d) At a time $t = \frac{2L - x_e - x_s}{c_0}$ the residual reflected propagating mode reaches the sensor array. The secondary sources anticipate its arrival and launch a wave at time $t = \frac{2(L - x_e)}{c_0}$ in order to drive it further to zero. As the sources will always under-estimate the level of this residual mode, this mechanism continues indefinitely resulting in a standing wave sound field between the sensor array and the inlet termination.

e) At a time $t = \frac{2x_s}{c_0}$ the reflected secondary pulse arrives back at the source array. The sources then radiates a pulse in order to attenuate the reflected secondary pulse. This pulse cancels with the forward propagating mode, but the backward propagating mode will once again be unaffected. This process continues indefinitely resulting

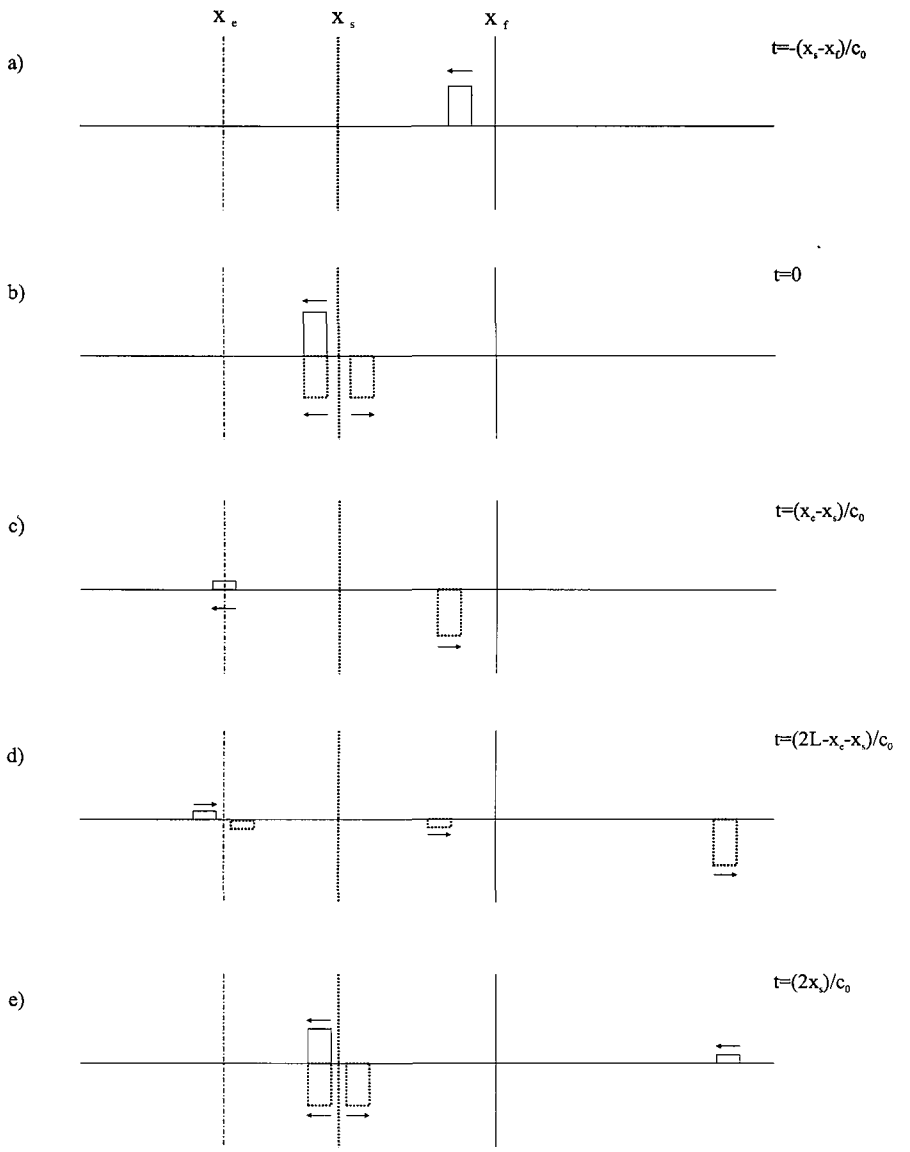

Figure 5.13: *A one-dimensional representation of the control mechanism*

in the standing wave sound field between the secondary sources and the exhaust termination. In the process of the controlling the weaker residual propagating mode, therefore a weak standing wave field between the error sensors and the inlet termination will also be set-up of lower amplitude.

5.3 Control performance with two rings of sources and two rings of sensors

Section 5.2 has shown that a single-ring control system cannot resolve the pressure detected at the error sensors into separate radial mode orders. As a consequence, in the absence of extraneous modes, the control system performance is limited by the amplitude of the evanescent mode associated with m_B excited by the secondary sources. In order to detect and control the separate radial mode orders, an additional ring of sources and sensors is required.

This is particularly true at full engine speeds which can reach values of up to $M_t \approx 1.3$. At these higher tip speeds, two or more radial mode orders can be cut-on.

Figure 5.14 is a sketch of the proposed two-ring control system.

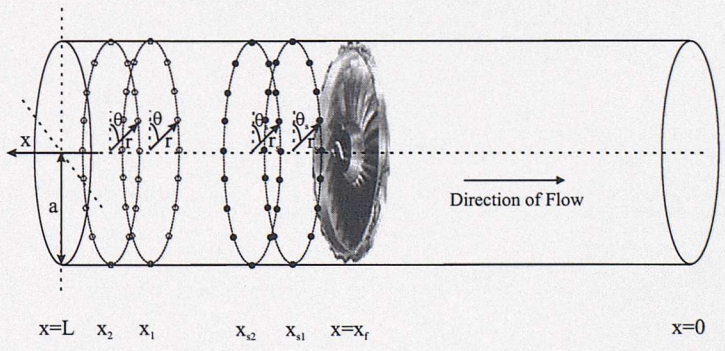

Figure 5.14: *Control system with two rings of sources and sensors*

It has been shown in section 5.2.1 that the number of sources and sensors required to substantially attenuate a single propagating mode is equal to $2|m_{max}| + 1$ where m_{max} is

equal to the highest propagating spinning mode order. Fruteau et al [21] show that the control of multiple radial mode orders requires as many source and sensor rings as the maximum propagating radial mode order.

Consistent with the results in section 5.2.1 each ring must contain $2|m_{max}|+1$ sources and sensors. In this section, we shall assume that each of the two rings contains 30 sources and sensors so that the control system will be effective in controlling the sound field at $EO \leq 14$ and at tip speeds where the number of propagating radial mode orders is less than or equal to two.

Figure 5.15 is a graph of the number of radial orders that can propagate at each EO from 1 to 14, over a range of tip speeds M_t which span both cutback and full power conditions for a typical aircraft engine. Here we assume $M_x = -0.52M_t$

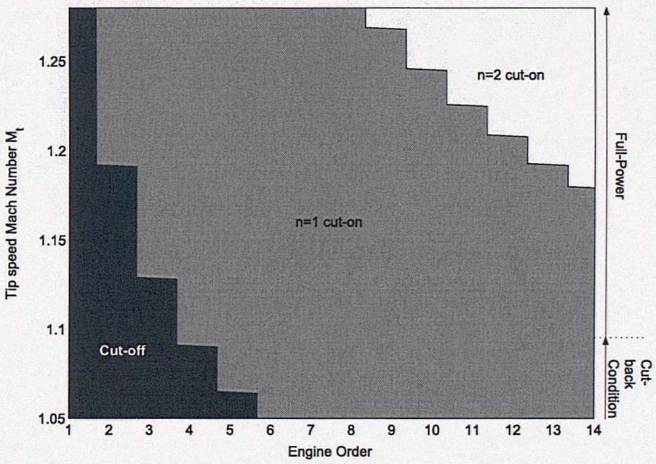

Figure 5.15: *Maximum number of radial mode orders cut-on at each engine order with varying tip speed mach number*

Figure 5.15 shows that in a typical engine more than one radial mode order becomes cut-on at high engine orders at conditions close to full-power. The two-ring control system should be able to successfully control all EOs up to $EO = 14$ at all tip speeds.

Figure 5.16 shows the sound power before and after control versus tip speed at EO=8. Results are plotted for both the single-ring system and the two-ring system. The single-ring system uses the same positions for control system elements as the model used in

the previous section. The two-ring system has the first source ring at an axial position $x_{s_1} = 0.8m$, the second source ring at $x_{s_2} = 1m$, the first sensor array at $x_{e_1} = 1.24m$ and the second sensor array situated at $x_{e_2} = 1.44m$.

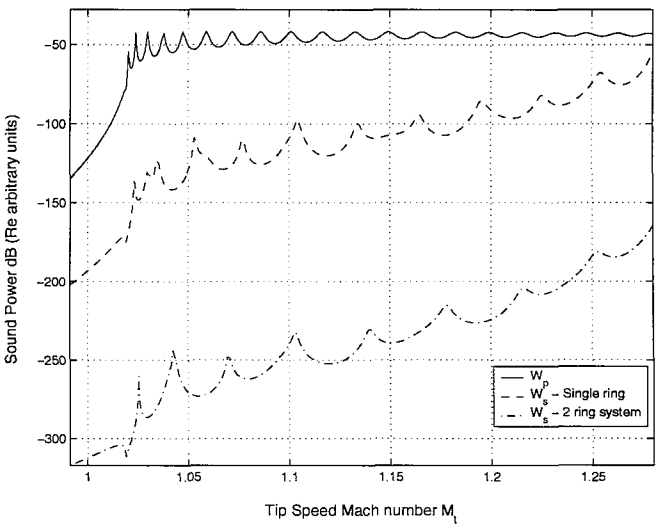

Figure 5.16: *Sound Power before and after pressure minimisation with two rings of 30 sources and 30 sensors to control EO=8*

The two-ring control system improves the sound power reduction by more than 100dB. Note also that the equations 5.34 and 5.35 for the single-ring control system no longer predict the spectral peaks for the two-ring control system. There are now fewer resonant peaks with the use of two rings of sources and sensors. The weak resonances associated with the residual evanescent mode in the single ring are no longer present as the evanescent mode can now be eliminated.

The control mechanism is more complicated than that with the single-ring control system. From the DFT argument discussed earlier in the chapter, driving the pressure to zero causes the amplitudes of the spinning modes at the duct wall to be driven to zero at both error sensor planes. It appears that it is easier for the control system to drive the spinning mode amplitudes to zero at two error sensor planes using two rings of sources than when using the single-ring control system.

5.4 Conclusions

- In the absence of noise, buzz-saw modes can be substantially attenuated by minimising the sum of the squared pressures at a single ring of sensors using a single ring of sources.

- The number of sources/sensors required to achieve control is equal to $2|m_{max}| + 1$, where m_{max} is equal to the highest propagating spinning mode order. However, a more practical criterion is suggested of $2|m_{max}| + 3$ in order to avoid problems associated with modal aliasing.

- Control performance is fundamentally limited by the level of the evanescent modes at the error sensor array. A simple analytic model was developed which predicts the sound power reduction.

- After control, strong standing waves are set up between the secondary sources and the exhaust termination, and weaker standing waves are also observed between the error sensors and the inlet termination. A control mechanism is explained which explains these standing wave regions.

Chapter 6

The Effect of 'Noise' and Extraneous Modes on Control Performance

Predictions of active control performance presented in the previous chapters assume that only a single buzz-saw mode is present in the primary sound field and that noise is absent. In reality, however, 'noise' or extraneous modes may be present at the error sensor array. These are defined below:

- 'Extraneous' modes ($m \neq m_B$). These may be excited by the various other source mechanisms in the engine. For example, rotor-stator interaction, rotor interaction with ingested turbulence, and other interaction mechanisms. This field propagates along the engine duct to the error sensors and may therefore be regarded as modal in nature.

- Locally generated noise. This could be present at the error sensor array due to factors such as turbulent flow noise at the microphones. This sound field is generated locally around the microphone and may be regarded as random contributions to the pressure measurements at each error sensor.

6.1 The effect of extraneous modes on control performance

This section investigates the effect of extraneous modes on active control performance.

6.1.1 Single ring of sources and sensors

In this section the active control performance prediction model described in chapter 3 is modified to include all possible modes in the primary field. The amplitude of the extraneous modes at the fan face $a_{p_{0_{em}}}$ are assumed to have equal amplitude but with random phase. The extraneous mode amplitudes $|a_{p_{0_{em}}}|$ relative to the buzz-saw mode $|a_{p_{0_{m_B}}}|$ at the fan face are determined by specifying a 'Signal to Noise Ratio' defined by

$$SNR_{em} = 20 \log \frac{|a_{p_{0_{m_B}}}|}{|a_{p_{0_{em}}}|} \tag{6.1}$$

and by assuming $a_{p_{0_{em}}} = |a_{p_{0_{em}}}|e^{i\phi}$ where ϕ is chosen randomly between $-\pi \leq \phi \leq \pi$.

In the absence of extraneous modes, the sound pressure after control at EO=8 using a single ring of 30 sources to minimise the pressure at a single ring of 30 sensors in the duct is reduced by 240dB, as described in chapter 5. The corresponding sound power reduction is predicted to be 89dB. If all propagating modes are included in the primary field at a level of 40dB below that of the buzz-saw mode then a similar level of pressure reduction is predicted at the error sensors. However, the sound power reduction is now only reduced by 19dB.

In order to explain this sensitivity of power reduction to small levels of extraneous modes we must once again examine the DFT relationship between the pressure sampled at the wall and the spinning mode amplitudes. It has been shown in chapter 5 that if the number of sources and sensors is sufficiently high, and the pressure at the error sensors is driven to zero, $p(\theta_l) = 0$, then the spinning mode amplitudes at the duct wall are also independently driven to zero, i.e.

$$\hat{a}_m = \frac{1}{\mathrm{L}} \sum_{\mathrm{l}=1}^{\mathrm{L}} p(\theta_\mathrm{l}) e^{-im\theta_\mathrm{l}} = 0 \tag{6.2}$$

Equation 6.2 suggests that using a single ring of sources and sensors to cancel the pressure at the error sensors causes the radial modes associated with a single spinning mode to be phased such that their amplitudes sum to zero. Since the single rings cannot independently detect and control individual radial modes, this is done without regard to the magnitude of their amplitudes.

This mechanism is illustrated in figure 6.1. It shows the predicted mode amplitudes for EO=8 at the error sensors before and after the minimisation of the sum of the square pressures using 30 sources and sensors. The extraneous mode amplitudes at the fan plane are set at 40dB below that of the buzz-saw mode.

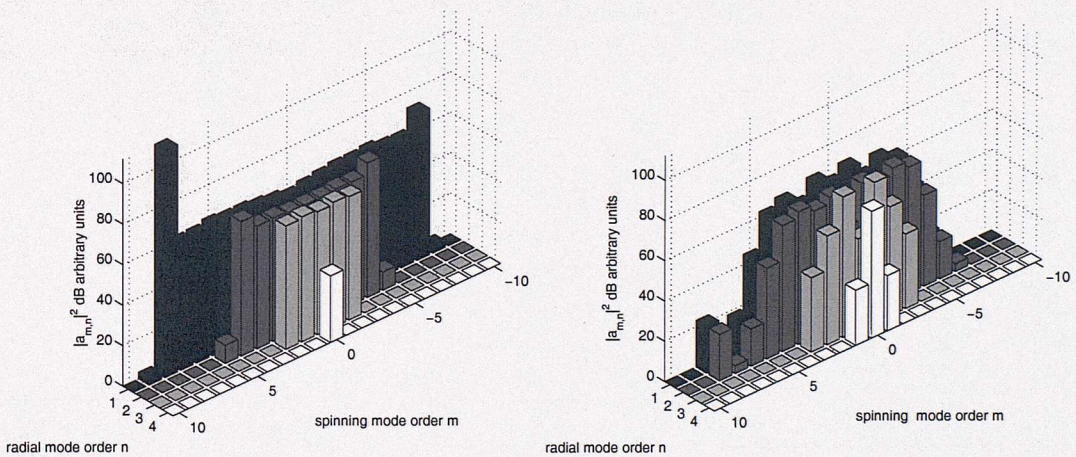

Figure 6.1: *Mode amplitudes at the duct wall before (a) and after (b) control at EO=8 at the error sensors. Extraneous modes are 40dB below the buzz-saw mode at the fan face*

Figure 6.1(a) for the mode amplitudes before control shows that for $5 \leq |m| \leq 8$ only a single propagating radial mode propagates, while for $|m| < 5$ there are up to 4 propagating radial mode orders, with the most associated with $m = 0$. It is also clear that evanescent modes all of which have cut-off ratios greater than 0.9 have a significant amplitude at the error sensors after control.

Figure 6.1(b) shows that the mechanism described in chapter 5 is applicable to all the modes $|m| \geq 5$ that comprise a single radial order mode. In each spinning mode, the propagating radial mode is driven to cancel with the evanescent mode.

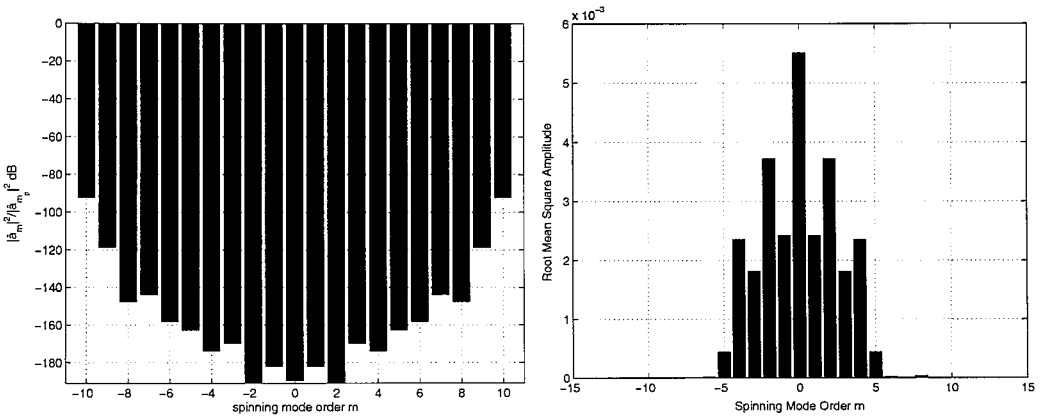

(a) (b)

Figure 6.2: *Sum of the radial mode orders (a) and root mean square amplitude of the modes in each spinning mode order (b) after control at EO=8 at the error sensors. Extraneous modes are 40dB below the buzz-saw mode*

For $|m| \leq 4$ there are multiple propagating radial mode orders which will be excited by both primary and secondary source array. In order to arrange for $\hat{a}_m = 0$, as shown in figure 6.2(a), the control system can only phase them such that they mutually cancel, i.e. $\sum_n a_{m,n} = 0$. This behaviour is shown in figure 6.2(a) for the reduction in the spinning mode amplitudes at the wall versus m. All spinning mode amplitudes are reduced by at least 90dB. Figure 6.2(b) is a plot of the mean of the radial modes associated with each spinning mode order. Clearly, the greater the number of radial mode orders associated with a particular m-value, the larger their average mode amplitude. In this figure, the $m = 0$ mode has the highest average mode amplitude, since at this frequency three radial mode orders can propagate in the duct. All three must be excited such that the sum of their amplitudes cancel, and hence their average value is higher than for the higher m-values.

6.1.2 Sound power reduction with varying extraneous mode 'signal to noise' ratio

In this section we shall investigate the variation of control performance with varying levels of extraneous modes in the primary field. The predicted sound power reductions at each engine order are shown in figure 6.3 for varying levels of SNR_{em}. The control system and system geometry defined in chapter 5 is assumed with a tip speed of $M_t = 1.05$ and an axial flow Mach number of $M_x = -0.55$. The control system consists of a single ring of 30 sources and 30 sensors.

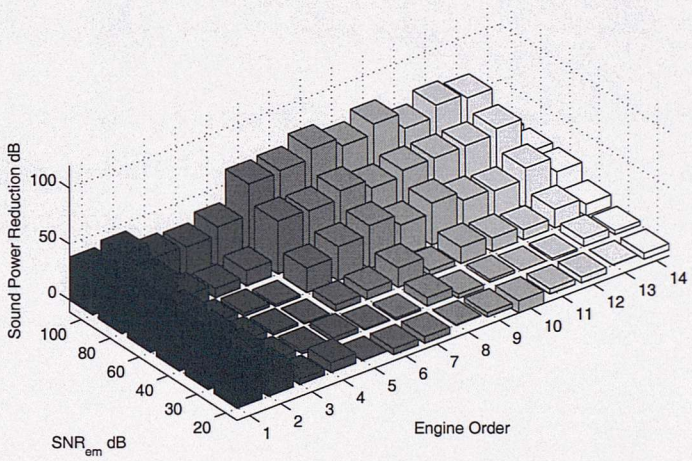

Figure 6.3: *Sound power reduction with extraneous mode SNR*

Large sound power reductions of up to 100dB are predicted in the absence of noise for all engine orders with (see figure 5.2). At EO=14, for which $m_B = 14$, the control system of 30 sources and sensors can only just independently control all the propagating modes and thus the control performance is affected by aliasing. Control performance is therefore degraded, as discussed in chapter 5.

For EO=1 to 5, the $m = m_B$ buzz-saw modes are cut-off and therefore transmit comparatively little sound power. The propagating extraneous modes therefore dominate the sound power in the duct. As the engine order increases, the number of propagating extraneous modes increases. For EO=1 to 3 only the first radial mode order can propagate

and thus the control system is unaffected by these extraneous modes. At EO=4 and 5 the second radial mode begins to propagate and cannot be independently controlled by the control system. Control performance is therefore quickly degraded as the level of the extraneous mode amplitudes is increased.

For EO=6 and above, multiple propagating radial modes are present and the system behaves as described in the previous section. In order to drive the pressure to zero, the control system will excite the modes with multiple radial modes orders such that the sum of the radial mode amplitudes is driven to zero. Thus as the engine order is increased, more 'extraneous' modes can propagate in the duct, and cannot be independently controlled. Thus the presence of 'extraneous' modes affects control performance to a higher degree at higher EOs than at low EOs, as shown in figure 6.3.

Figure 6.3 shows that although sound power reduction is reduced with extraneous modes present, the control system achieves reductions in sound power at all EOs provided $SNR_{em} > 30dB$. At lower values of SNR_{em} sound power increases are observed at some EOs. The levels of low frequency buzz-saw tones in practice are typically 130-140dB. It is therefore likely that the signal to noise ratio may be very large. This is confirmed by figure 6.4 which shows the spinning mode amplitudes at EO=6 measured in the EU experimental fan rig.

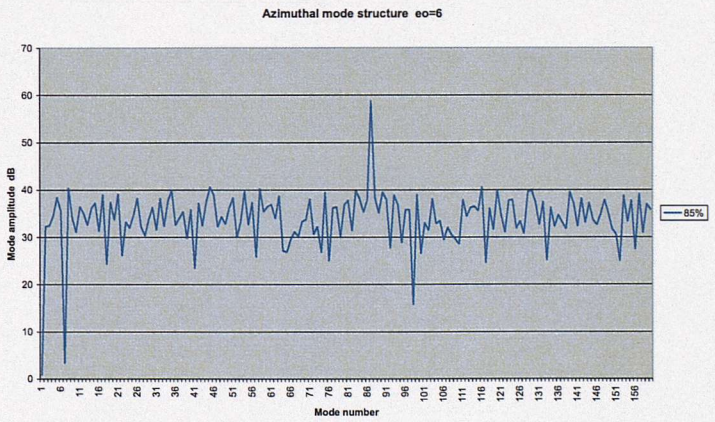

Figure 6.4: *Spinning mode decomposition at EO=6 for the EU SILENCE(R) experimental rig*

The decomposition includes modes from $m = -79$ to $m = 79$. It shows that mode 86 is dominant, corresponding to the spinning mode order $m_B = EO = 6$. In this measurement the signal to noise ratio of the microphones is 18dB due to the non-uniform sensor arrangement used in the mode detection ring. Thus, the only mode amplitude which is accurately measured is that of the $m = 6$ suggesting that the actual value of SNR_{em} is $> 18dB$ and that control may be limited in this rig extent by locally generated 'noise' at the microphones. The effect of this type of noise will be examined later in the chapter.

6.1.3 Two rings of sources and two rings of sensors

We have seen that a control system which seeks to minimise the sum of the squared pressures at two rings of error sensors using two source rings is able to resolve and independently control two separate radial mode orders in any single spinning mode. Thus, a control system with two rings of sources and sensors should be less affected by the presence of extraneous modes than the single ring control system studied previously. It will be able to drive more of the spinning mode orders to zero by reducing their amplitudes and not by simply phasing them to destructively interfere, as observed in figure 6.1. This is now investigated in more detail.

The control system under consideration is illustrated in figure 6.5. The positions of the sources and sensors are the same as in the previous section.

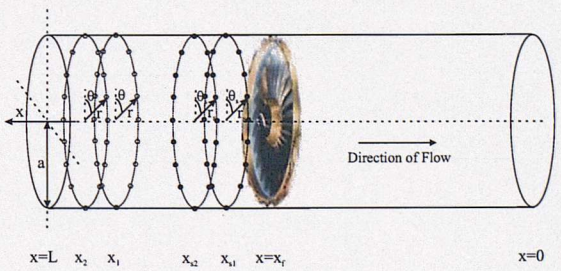

Figure 6.5: *Geometry of the two ring control system*

Figure 6.6 shows the sound power reduction predicted at each engine order for varying

extraneous mode levels, using 2 rings of sources and sensors.

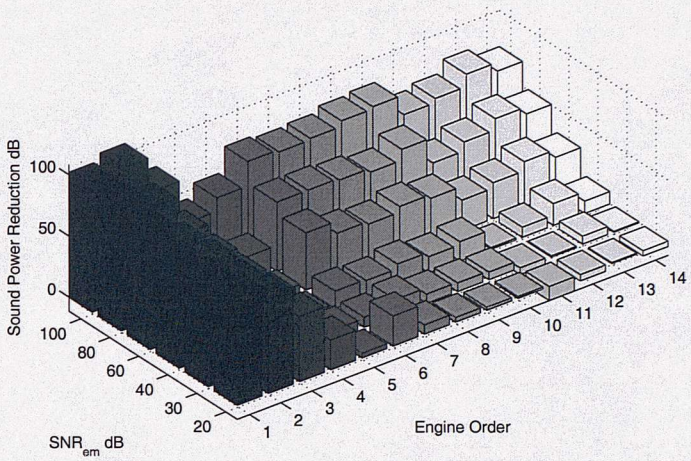

Figure 6.6: *Sound power reduction with extraneous modes of varying levels in the primary field for the two ring system*

Comparing figures 6.3 for the single-ring case and figure 6.6 for the two-ring case one can see that the sound power reduction for the lower engine orders (EO=1 to 3) has significantly increased. This is due to the fact that at these engine orders there is only a single propagating radial mode at any spinning mode order. The two-ring system can drive this propagating mode to zero and also attenuate any inadvertently excited evanescent $n = 2$ modes.

By contrast, the sound power reductions at the higher EO in the presence of extraneous modes is very similar using both the single-ring and the two-ring control systems. This can be explained by examining the amplitudes of the modes after control for the two-ring system with $SNR_{em} = 40dB$. The mode amplitudes at the error sensors before and after control are plotted in figure 6.7.

The two-ring system can be seen to attenuate the second radial mode orders which are excited in the primary field for engine orders 3 to 5. Thus for spinning mode orders $5 \leq |m| \leq 8$ the propagating modes and any evanescent modes $n \leq 2$ can be driven to zero. For mode orders $3 \leq |m| \leq 4$ where two radial modes can propagate, these modes

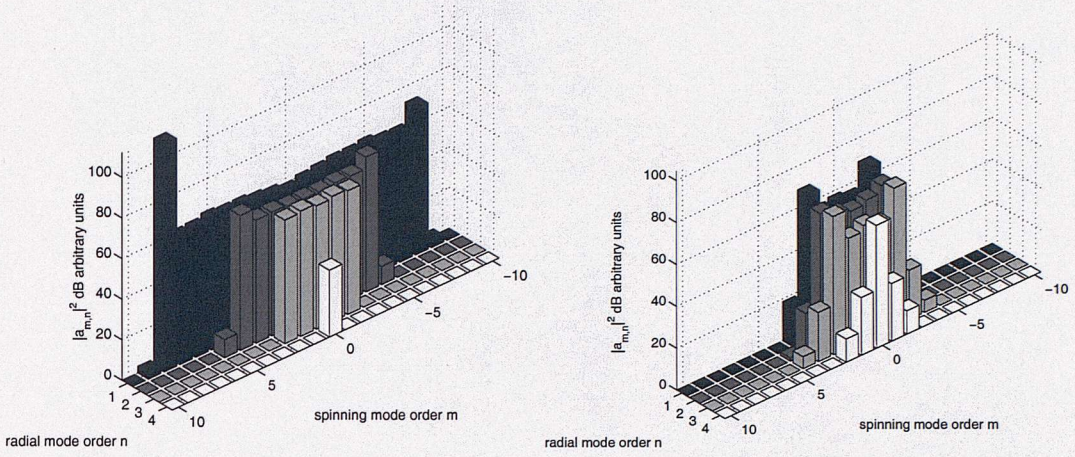

(a) (b)

Figure 6.7: *Individual mode amplitudes at the duct wall before 6.7(a) and after 6.7(b) control at EO=8, extraneous modes 40dB below the buzz-saw mode*

will be driven to zero. Spinning mode orders less than 5 comprise more than 2 propagating radial mode orders. In order to ensure that the spinning mode amplitude at the wall equals zero, therefore, the radial modes are simply phased to interfere destructively. These modes will still have a significant amplitude at the error sensors and will therefore dominate the sound power after control in a similar way to the single-ring system.

Figure 6.7(b) shows that, although the two-ring system is more effective in controlling the higher order spinning modes, it is the lower spinning mode orders that will dominate the sound power after control. The sound power reduction is therefore similar for both the single-ring and two-ring control systems at higher EOs with low signal to noise ratio.

The sum of the spinning mode amplitudes and the average amplitude of the modes in each spinning mode are plotted in figures 6.8(a) and 6.8(b) respectively for the two-ring system. As in the single-ring control system, figure 6.8(b) shows that the average spinning mode amplitude after control is highest in the $m = 0$ case.

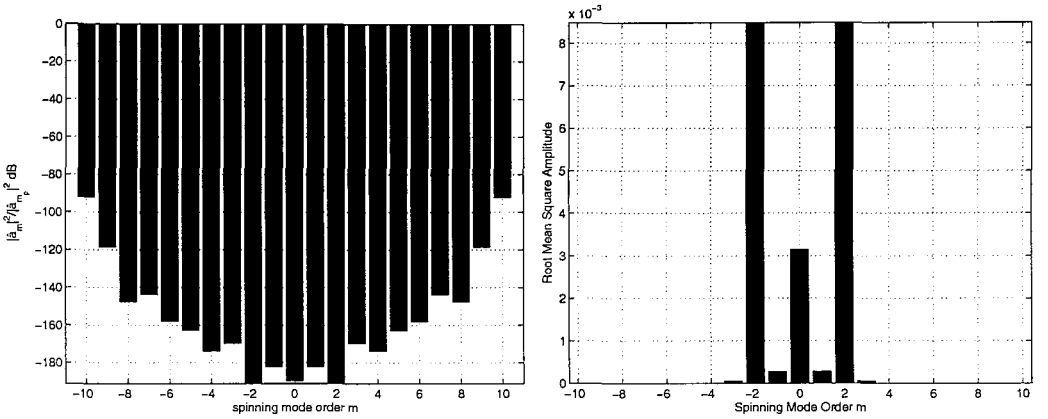

(a) (b)

Figure 6.8: *Sum of the radial mode orders (a) and the root mean squared amplitude of the amplitudes in each spinning mode order (b) after control at EO=8 at the error sensors for a two-ring system. Extraneous modes are 40dB below the buzz-saw mode*

6.2 The effect of 'local' noise on control performance

6.2.1 Single-ring of sources and sensors

The second type of 'noise' which could be present in the engine duct and and which may affect control performance is that of 'local' noise at the error sensors. This noise is not modal in structure and can be caused by flow noise generated locally at the microphones. In order to quantify the effect of this 'local' noise on control performance we shall once again define a Signal to Noise Ratio. The noise is defined by a signal to noise ratio of the amplitude of the primary pressure at a single error sensor to the amplitude of the noise n,

$$SNR_{ln} = 20 \log \frac{|p_p(\theta_l)|}{|n_p|} \tag{6.3}$$

The 'noise' at the error sensors is simulated from $n_p = |n_p|e^{i\phi}$ where ϕ is chosen randomly between $-\pi \leq \phi \leq \pi$. The 'noise' signals are added to the primary pressure measured at the error sensors,

$$p_{p_n}(\theta_l) = p_p(\theta_l) + n_p(\theta_l) \tag{6.4}$$

Figure 6.9 shows the spinning mode decomposition of the pressure signals at EO=8 before control in the case of extraneous modes of $SNR_{em} = 40dB$ and 'local' noise at the error sensors of $SNR_{ln} = 40dB$.

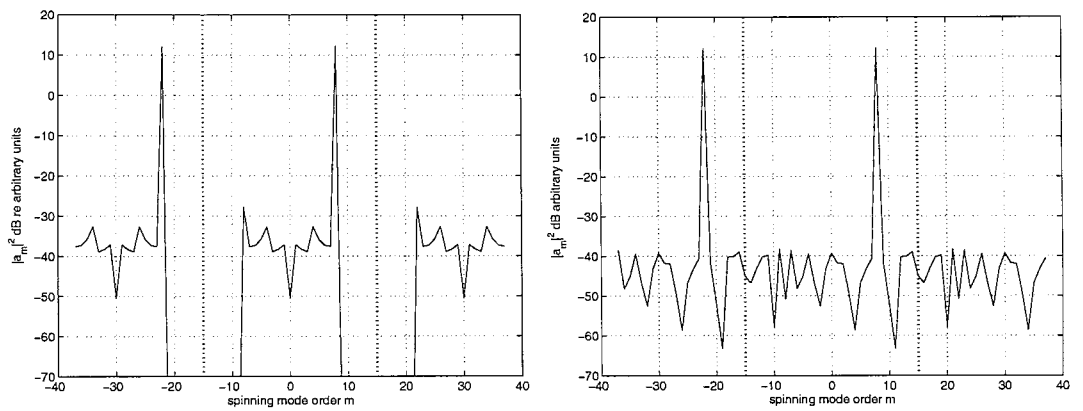

(a) (b)

Figure 6.9: *Spinning mode decomposition at EO=8 at the error sensors for a single ring system. (a)* $SNR_{em} = 40dB$ *(b)* $SNR_{ln} = 40dB$

In the case of the extraneous modes in figure 6.9(a), the spinning mode orders with a significant amplitude contribution at the error sensor array are restricted to the propagating modes. In this case there are sufficient sources and sensors to drive all spinning mode amplitudes to zero.

However, when this noise is local in nature, as assumed in figure 6.9(b), it appears to the control system that *every* spinning mode order has a significant amplitude at the error sensor array, whether cut-on or cut-off. The control system will therefore attempt to control all these 'modal' contributions. As there will be insufficient sources and sensors to control the higher mode orders, they will be aliased and the DFT argument given in 6.2 will not apply, hence the spinning mode amplitudes will not be driven to zero.

'Optimal' regularisation parameter

We have shown in chapter 4 that the transfer impedance matrix $\mathbf{Z}$ generally has a large condition number at low EO due to the fact that there are more sources than propagating spinning modes [17]. A small change in the pressure $\mathbf{p}$ due to noise at the error sensors will therefore result in a comparatively large change in the optimal secondary source strengths $\mathbf{q}$. It was found in chapter 4 that, using Hansen's L-curve technique [23], the optimal value for the regularisation parameter β for the single ring system was of the order of 10^7. This value of β gave roughly minimum values for the both the secondary source strengths and the residual pressure after control simultaneously.

We shall now investigate whether this 'optimal' value for β also gives the optimum level of sound power reduction in the presence of extraneous modes and locally generated noise. Figure 6.10 shows the sound power reduction after control with varying regularisation parameter β for the single-ring control system at EO=8 in the presence of both types of noise. The first vertical dotted line shows the value of the 'optimal' β as determined from the L-curve.

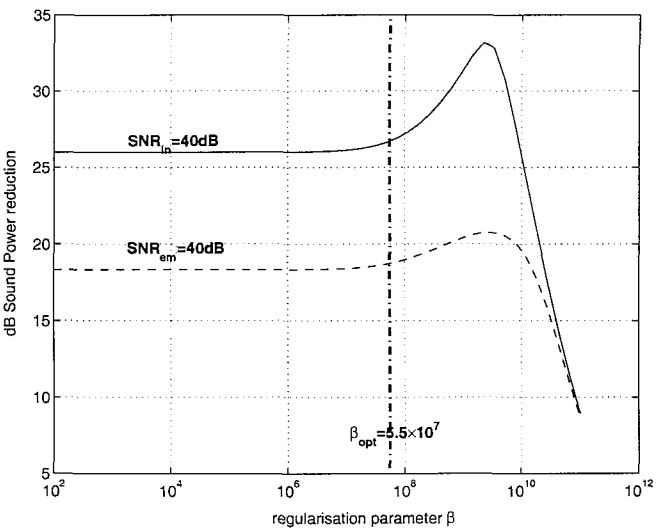

Figure 6.10: *Sound Power reduction at EO=8 with varying regularisation parameter β for a single ring control system with $SNR_{ln} = 40dB$ and with $SNR_{em} = 40dB$.*

Figure 6.10 shows that the sound power reduction is *not* at a maximum at the 'optimum'

value of β. Thus the 'optimal' value for β from the L-curve is the value which minimises the pressure at the error sensors, which is not necessarily the value that minimises the sound power. It therefore appears that the greatest sound power reduction occurs when using a regularisation parameter of $\beta \approx 2 \times 10^9$. This value of β shall be used to predict the mode amplitudes after control at the error sensors.

The dashed line in figure 6.10 shows the variation in sound power reduction with varying β where the level of extraneous modes is 40dB below the level of the buzz-saw mode. It was noted in chapter 4 that regularisation was not needed in order to limit the source strengths in this case. However, as the value of β is increased the sound pressure reduction is reduced as the regularisation parameter begins to dominate the leading diagonal of the transfer impedance $\mathbf{Z}$. At a value of $\beta \approx 1 \times 10^9$ the sum of the squared pressures is driven to a value of the order of 10^{-1} as opposed to values of the order of 10^{-28} with no regularisation applied. Equation 6.2 indicates that if the pressure is not driven to zero, then the spinning mode amplitudes will also not be driven to zero. It appears that at this β value the extraneous mode amplitudes are excited to a lower level which results in a greater sound power reduction. Further research is required to determine why this is the case.

Control performance in the presence of locally generated noise

In the presence of local noise with $SNR_{ln} = 40dB$ the sum of the squared pressures after control in the regularised case is of the order of 10^{-1} relative to an amplitude of 1 before control. The pressure is therefore not driven to zero, and thus the control system has not perfectly cancelled to zero the individual spinning mode orders at the duct wall.

Comparison of figure 6.11 for the mode amplitudes at the error sensors in the presence of local noise with figure 6.1(b) for the mode amplitudes in the presence of extraneous modes, shows that, in the case of local noise, the radial mode orders do not appear to be excited such that they destructively interfere. The mode amplitudes after control are not as high as when extraneous modes are present and thus the sound power reduction

after control will be greater in the case of locally generated random noise which effectively comprises a broad modal spectrum.

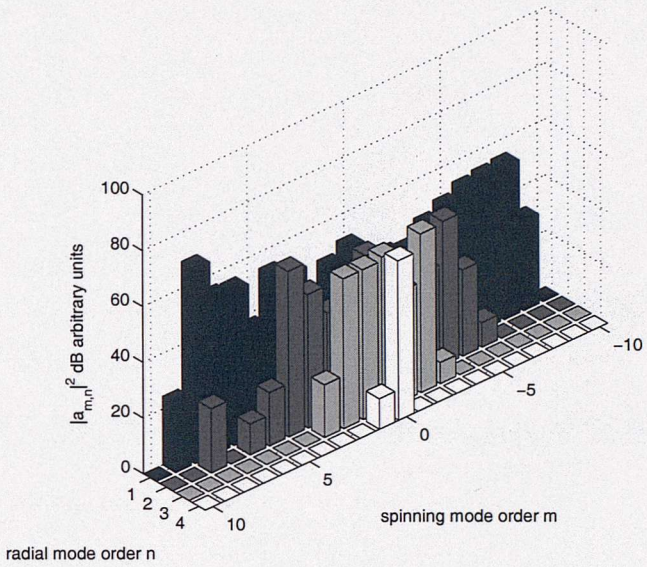

Figure 6.11: *Individual mode amplitudes at the error sensors after control for a single ring system with* $SNR_{ln} = 40dB$.

Locally generated random noise at the error sensors contains high m-values that are aliased. The control system will be contaminated by higher order modes which do not propagate to the far field. This behaviour actually *improves* control performance. Figure 6.12 shows the control performance of the single-ring system at EO=8 with varying SNR_{em} and SNR_{ln}. This figure shows that sound power reduction can be up to 12dB greater when the noise is locally generated at the error sensor array.

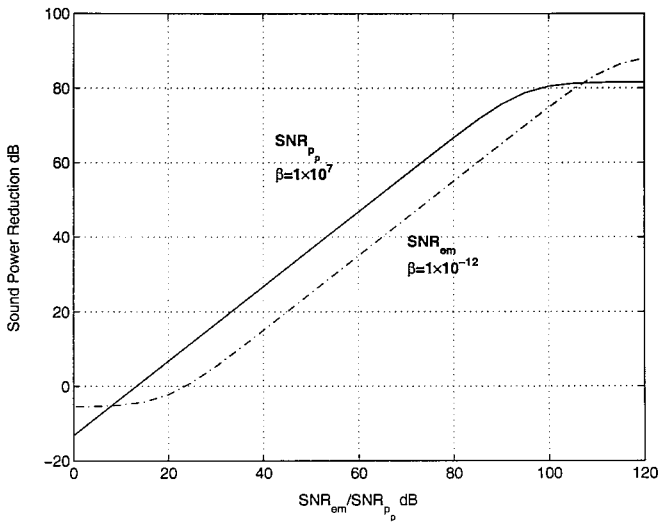

Figure 6.12: *The effect on control performance of the two types of 'noise' of the single ring system at EO=8*

6.2.2 Control performance using two rings of sources and two rings of sensors in the presence of locally generated noise

The effect of 'local' noise on the control performance of the two-ring control system is similar to the single-ring case. The use of two rings of sources and sensors yields slightly improved sound power reductions. Regularisation must be used in order to limit the source strengths as the transfer impedance matrix $\mathbf{Z}$ is now twice the size and consequently has a higher condition number. The optimum regularisation parameter is, however, is the same.

Figure 6.13 shows the individual mode amplitudes at the first ring of error sensors. The source rings are positioned at $x_s = 1.24m$ and $x_s = 1.44m$ and the sensor rings are at $x_e = 0.8m$ and $x_e = 1m$. The regularisation parameter is set to $\beta = 1 \times 10^9$

Once again, with local noise present, the amplitudes are not phased for perfect destructive interference, and are not excited to as high a level as in figure 6.7(b).

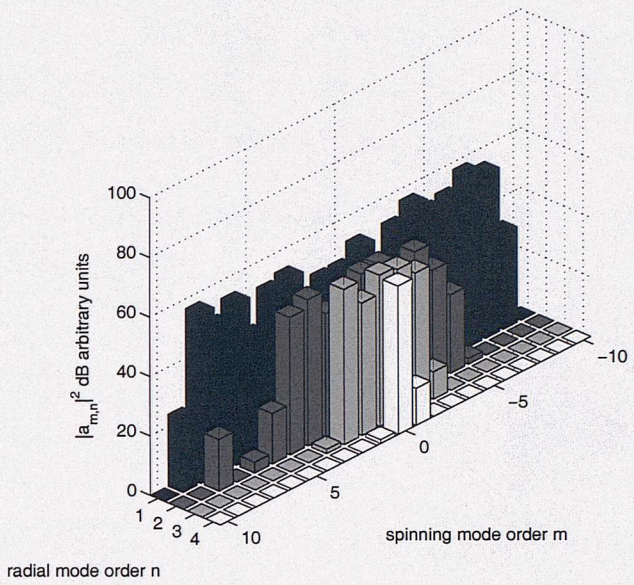

Figure 6.13: *Mode amplitudes at the error sensors at $x_e = 1.24m$ after control for a system with two rings of sources and two rings of sensors with $SNR_{ln} = 40dB$ with $\beta = 1 \times 10^9$.*

6.3 Conclusions

- The effect of extraneous modes and noise on control performance was studied.
- In the presence of extraneous modes, the pressure is driven to zero after control. However, the sound power reduction is degraded when compared to the noise free case. The sound power after control is dominated by the spinning mode orders which contain multiple radial mode orders, which cannot be independently controlled by the single ring system. These are excited such that they cancel, and therefore the higher engine orders are most affected by the presence of extraneous modes.
- Improvements in control performance are observed when using two rings of sources and sensors, however control will still be dominated by the level of the spinning mode orders with more than 2 propagating radial modes, thus the improvement at higher EOs and low SNR_{em} is not significant.
- When 'local' noise is added at the error sensors, the pressure is not driven to zero. The buzz-saw mode is attenuated, however, and the extraneous modes excited by

the secondary sources are not excited such that they cancel. It is predicted that sound power reduction will be greater if the noise is predominantly 'local' noise. Examining the modal decomposition of the EU experimental rig, it is likely that the noise will be mainly local to the error sensors.

- In the presence of local noise, the two ring system does not give significant improvements in control performance.

Chapter 7

Active Control of Buzz-saw Tones Using Modal Control Techniques

7.1 Introduction

It was shown in Chapter 5 that, in the absence of noise and extraneous modes, global control of the buzz-saw sound field can be achieved by simply minimising the sum of the squared pressures at the error sensors. However, when extraneous modes are present we have seen in chapter 6 that the pressure can still be driven to zero but the individual mode amplitudes are not necessarily driven to zero. With multiple radial modes present, spinning modes comprising multiple radial modes are excited so that their amplitudes at the duct wall cancel, according to the DFT argument proposed in chapter 5. An alternative control objective to pressure minimisation is to minimise the sum of the squared *mode amplitudes*. If this can be driven to zero, individual mode amplitudes will be driven to zero, and hence the sound power after control is eliminated. It has been noted in chapter 4 that it would require a large number of error sensors and a high computation overhead in a real-time control system in order to fully decompose the sound field into individual modal contributions. In this chapter, therefore, we shall investigate the extent to which the sound power can be reduced by minimising the sum of the squared spinning

mode amplitudes at the duct wall. These mode amplitudes can be easily calculated by performing a spinning mode decomposition of the pressure measurements at the error sensors. This modal approach will later be generalised to allow for arbitrary weighting of the various modal contributions.

7.2 Minimising the sum of the square spinning mode amplitudes at the duct wall

We shall now examine the behaviour of a control system with the same arrangement of sources and sensors as that shown in figure 5.1 in Chapter 5. Unless otherwise stated, the fan plane is positioned at $x = 0.6m$, the single ring of 30 secondary sources is positioned at $x = 1m$ and the single ring of 30 error sensors at $x = 1.24m$ in a duct of length $1.84m$ and radius $0.4m$. Once again a uniform mean flow of axial flow mach number $M_x = -0.55$ and tip speed mach number of $M_t = 1.05$ is assumed.

The spinning mode amplitudes *at the duct wall* can be calculated from pressure measurements at the error sensor array. This procedure is detailed in Chapter 4. The amplitude for the spinning modes at the plane of the error sensors can be determined from

$$\hat{a}_m = \frac{1}{L}\sum_{l=1}^{L} p(\theta_l)e^{-im\theta_l} \tag{7.1}$$

The optimum source strength vector $\mathbf{q_{opt}}$ for minimising the sum of the squared mode amplitudes at the duct wall, $J = \hat{\mathbf{a}}_m{}^{\mathbf{H}}\hat{\mathbf{a}}_m$, is given by

$$\mathbf{q_{opt}} = -[\hat{\mathbf{Z}}_m^{\mathbf{H}}\hat{\mathbf{Z}}_m]^{-1}\hat{\mathbf{Z}}_m^{\mathbf{H}}\hat{\mathbf{a}}_{\mathbf{m_p}} \tag{7.2}$$

where $\hat{\mathbf{Z}}_m$ is a matrix of 'modal' transfer impedances, whose (i,j)th element describes the extent to which the ith source couples into the jth spinning mode.

7.2.1 Equivalence of minimising the sum of the square spinning mode amplitudes and minimising the sum of the squared pressures

In section 5.2.2 it was demonstrated that if a sufficient number of sources and sensors is employed and the pressure is driven to zero at each error sensor, then the spinning mode amplitudes at the duct wall are also driven to zero. This relationship is reciprocal. Driving the sum of the spinning mode amplitudes at the duct wall to zero also drives the pressure at the error sensors to zero. This reciprocity follows from Parseval's theorem, which states that the 'energy' of a signal is the same whether expressed in one domain or its Fourier domain. Thus, following from the Fourier transform relationship,

$$p(\theta_l) = \sum_m \hat{a}_m e^{im\theta_l} \tag{7.3}$$

Parseval's theorem states that J is entirely equivalent whether expressed in terms of pressure or spinning mode amplitudes at the duct wall,

$$J = \sum_{l=1}^{L} |p(\theta_l)|^2 = \sum_m |\hat{a}_m|^2 \tag{7.4}$$

Equation 7.4 makes explicit that $\hat{a}_m = 0$ for all m implies that $p(\theta_l) = 0$ for all l. The pressure and modal active control approaches are therefore identical.

This is confirmed in figure 7.1, which shows the sound power both before and after the minimisation of the spinning mode amplitudes at the duct wall with varying tip speed for buzz-saw mode EO=8 in the absence of extraneous modes. It is identical to the power reduction presented in figure 5.16 following pressure minimisation.

7.2.2 Minimisation of the sum of squared weighted mode amplitudes

It has been shown that if one attempts to drive all of these spinning mode amplitudes to zero simultaneously then the control performance will be identical to that of pressure

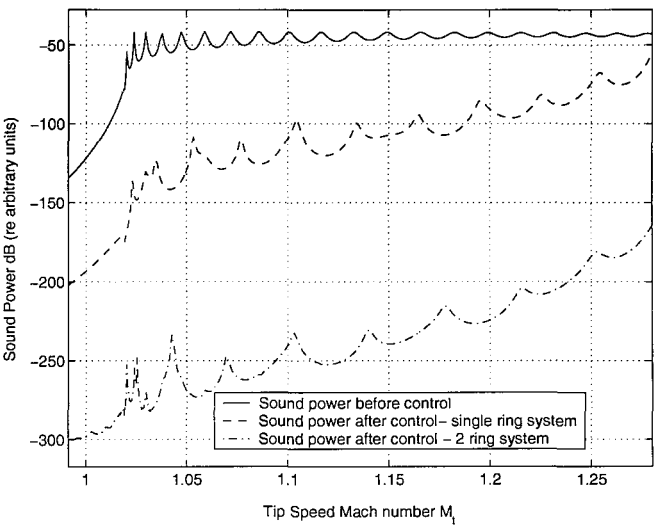

Figure 7.1: *Active control performance with varying tip speed for a single ring of 30 sources and 30 sensors and a system with two rings of 30 sources and two rings of 30 sensors at EO=8 after minimisation of all spinning mode amplitudes at the duct wall*

minimisation. However, if the spinning mode amplitudes in the cost function are weighted, one can select which spinning mode orders are controlled. As shown in chapter 6, in the presence of noise, driving the spinning mode amplitudes to zero does not ensure sound power reductions. The modal approach is therefore beneficial when noise is present as no control effort is 'wasted' controlling extraneous or aliased spinning modes, since these modes are ignored by the control system.

When modal weighting is applied, the cost function in equation 4.5 generalises to

$$J = \sum_{i=1}^{I} \sum_{m} |w_m \hat{a}_m(x_i)|^2 = \hat{\mathbf{a}}_m{}^{\mathrm{H}} \mathbf{W_m} \hat{\mathbf{a}}_m \tag{7.5}$$

Of particular interest here is the case when all the control effort is focussed on the buzz-saw mode, whilst ignoring the other modes. In this case, the weighting function is of the form

$$w_m = \begin{cases} 1 & m = m_B \\ 0 & m \neq m_B \end{cases} \tag{7.6}$$

The effectiveness of this control strategy compared to the uniformly weighted case is now examined. Figures 7.2(a) and 7.2(b) show the individual mode amplitudes at the error sensors before and after control for EO=8 for an assumed extraneous mode SNR of $SNR_{em} = 20dB$.

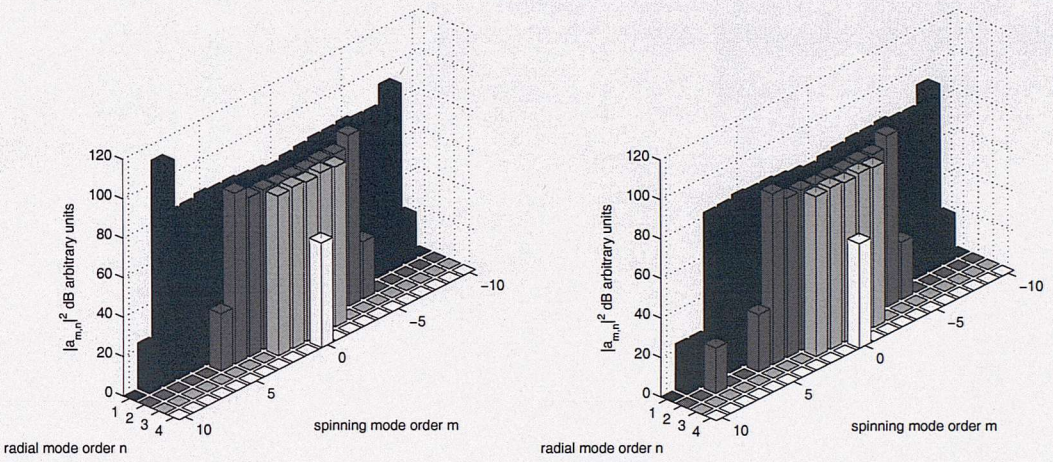

Figure 7.2: *Mode amplitudes before (a) and after (b) control at EO=8 with* $SNR_{em} = 20dB$ *using a weighted cost function*

Figure 7.2(b) show that control has occured solely in the mode order ($m = m_B = 8, n = 1$) which has reduced by approximately 90dB. The level of the buzz-saw mode is now equal to the second radial mode associated with $m = m_B$. The control principle described in chapter 5 for the case when no noise is present now also applies to this case. By contrast with the case when the modes were uniformly weighted, the extraneous modes are unaffected by the secondary source array and their levels are identical after control. By weighting the cost function, the secondary sources are effectively controlling the sound field as if there were no extraneous modes present.

This approach will also improve control performance where 'non-modal' local noise is

present at the error sensors. The control system will not attempt to control the higher order spinning modes which it 'observes' at the error sensors. Since only the buzz-saw mode is being controlled the control system will always meet the Nyquist criteria as $|m_{max}| = 8$, and hence good control performance is assured.

The benefits of single-mode control in relation to uniformly weighted modal control in the presence of local noise and extraneous modes are now investigated. Figure 7.3 shows the variation in sound power reduction with varying tip speed Mach number M_t following the minimisation of the sum of the squared pressures, the minimisation of the sum of the squared spinning mode amplitudes, and the minimisation of the buzz-saw mode only. Here we assume that there are extraneous modes in the primary field at a level of $SNR_{em} = 20dB$.

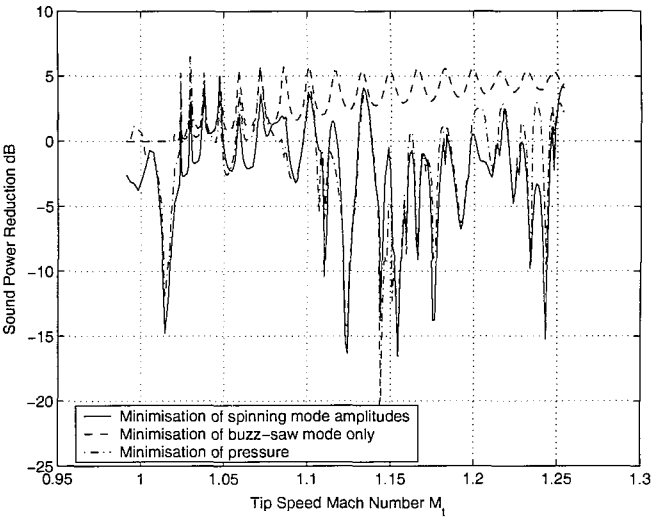

Figure 7.3: *Active control performance with varying tip speed for a single ring of 30 sources and 30 sensors and with extraneous modes at the fan face at levels 20dB below the level of the buzz-saw mode*

In the weighted mode case a sound power reduction of up to 5dB is observed at all tip speeds. With the buzz-saw mode now removed by the control system the sound power is now dominated by the propagating extraneous modes. Assuming equal power per mode in all extraneous modes the sound power after control is approximately equal to $-SNR_{em} + 10\log_{10} N$ where N is the number of propagating extraneous modes which

in this case is equal to 31.

Figure 7.4 shows the performance of the three control strategies when the noise present at the error sensors is due to 'local' noise at the error sensors. A regularisation parameter of $\beta = 1 \times 10^7$ has been used for all tip speeds in order to prevent unrealistically high optimal source strengths.

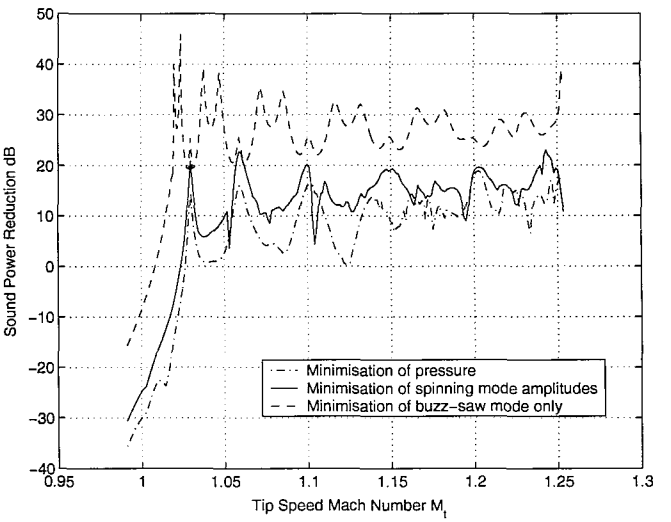

Figure 7.4: *Active control performance with varying tip speed for a single ring of 30 sources and 30 sensors and with 'local' noise at the error sensors at a level 20dB below the level of the buzz-saw mode*

As in figure 7.3, the pressure and spinning mode control strategies afford similar control performance. Substantially larger sound power reduction is observed when control is confined to the buzz-saw mode with improvements of up to 30dB being obtained at certain tip speeds compared with a maximum of 20dB for pressure minimisation.

It should be noted that minimising the weighted cost function involves inverting a 'modal' transfer function matrix $\hat{\mathbf{Z}}$ that is sparse with only a single row of non-zero elements. This matrix will therefore have singular values equal to zero. These will need to be discarded using a small regularisation parameter in order to obtain the pseudo-inverse of the matrix. The regularisation parameter required is substantially smaller than the regularisation parameter required in the minimisation of all spinning mode amplitudes.

In practice, noise at the error sensor array will be due to local 'non-modal' noise and extraneous modal contributions simultaneously. However, it is clear from the above that the single-mode cost function offers considerable benefit compared to the pressure, and uniformly weighted control algorithms, which attempts to control *all* modes indiscriminately.

Despite the improvement over pressure minimisation in the presence of noise, modal control does have some practical disadvantages when compared to the minimisation of the sum of the squared pressures. Firstly, the control elements will require careful phase calibration. Secondly, the actuator array will require all the speakers to be working in order for the mode to be synthesised. If an actuator fails, control will be severely degraded whereas, in the pressure minimisation case, the control system can adapt to the failure of a control system element. Finally, if the control objective is focussed on a single mode then if energy is scattered into another spinning mode order it will be ignored by the control system resulting in poor control performance.

7.3 Conclusions

- When the sum of the spinning mode amplitudes is minimised the control performance is identical to that achieved when minimising the sum of the square pressures.
- In the presence of noise, significant improvements in control performance are gained by weighting the cost function such that control is focussed on the buzz-saw mode $m = m_B$. The biggest increases are observed if the noise is 'local' to the error sensors.
- Modal control has a number of practical disadvantages: Control system elements must be phase calibrated, failure of control system elements will result in severe degradation of control performance and the control system cannot control scattered modes.

Chapter 8

Active Control Experiments

8.1 Introduction

Previous chapters have been concerned with theoretical aspects of the active control of buzz-saw tones. It has been shown that substantial reductions in the sound power radiated by a single spinning mode can be achieved in the absence of extraneous modes, but that the presence of extraneous modes can significantly degrade control performance.

This chapter describes experimental results relating to the control of a single spinning mode using a real-time control system comprising a single ring of 7 actuators and a single ring of 7 error microphones. The primary field, designed to simulate the characteristics of a buzz-saw tone, comprises 7 loudspeakers arranged in a ring. Figure 8.1 shows the experimental rig and the positions of the loudpspeaker and error microphone arrays.

The no-flow duct rig has a length of 2m and a radius of 0.3m. As demonstrated in chapter 5 the seven loudspeakers and seven error microphones are sufficient to control, without spillover, all spinning modes in the range $-3 \leq m \leq 3$. The array of actuators on the far right in figure 8.1 are used to excite, at a given frequency, the $m = -3$ spinning mode. This is achieved by exciting each loudspeaker with a single frequency signal and introducing a phase delay of $6\pi/7$ between adjacent loudspeakers. The following section provides a more

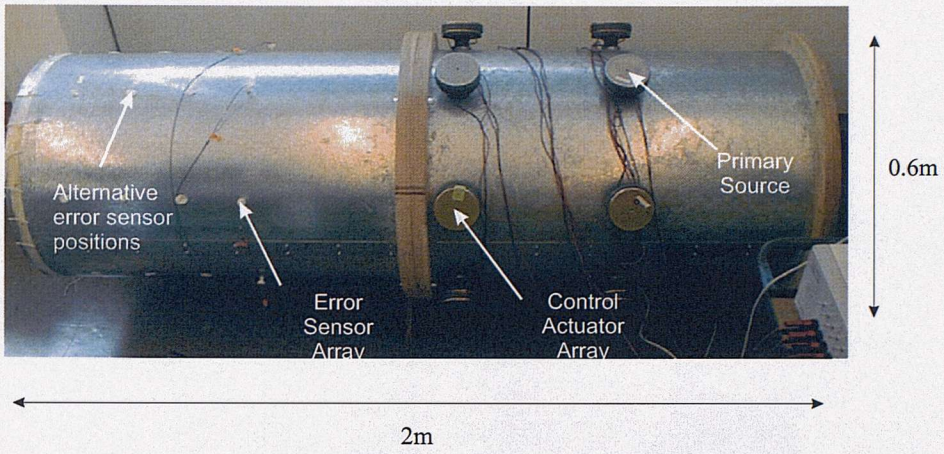

Figure 8.1: *The duct section and control system*

detailed account of the aspects of the experimental rig and the experimental procedures.

8.2 Experimental procedure

The aim of the experiment is to determine the extent to which 'global' control of the sound field can be achieved by driving the pressure to zero at the error sensors. The pressure is minimised at the error sensors by the use a real-time adaptive control system to minimise the sum of the square pressures measured at the error sensor array. The sound power radiated from the duct is then measured before and after control using a sound intensity probe in order to determine the sound power reduction.

It has been shown in chapter 5 that with seven loudspeakers and seven microphones the highest spinning mode order which can be successfully controlled without spillover into other modes is the $m = \pm 3$ mode. Thus the frequency range over which control will be attempted will extend from the cut-on frequency of the $(-3, 1)$ mode to the cut-on frequency of the $(-4, 1)$ mode, $f_{-3,1} < f < f_{-4,1}$. In our duct section the $(-3, 1)$ mode cuts on at 764Hz and the $(-4, 1)$ mode cuts-on at 967Hz. The effect on control performance of source-sensor array separation distance will also be investigated.

8.3 The experimental rig

8.3.1 Mode synthesiser ring

Figure 8.2 shows the power amplifiers used to drive the primary and secondary loudspeaker arrays. Channels 1 to 7 are connected to the loudspeaker array via a 'delay unit' which will introduce the $6\pi/7$ phase shift needed to generate the $m = -3$ spinning mode.

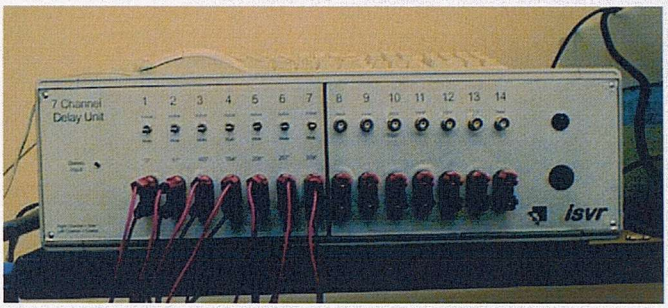

Figure 8.2: *Power amplifiers used to drive the primary and secondary actuators, including the delay line used to drive the mode synthesiser ring*

The phase shifts between primary actuators are generated from two sinusoidal signals 90 degrees out of phase, fed to the delay unit. This phase shift is achieved by generating a sine wave, and then passing it through an analogue integrator circuit to obtain the cosine signal. The integrator box contains an adjustable gain so that the amplitude of the cosine wave can be adjusted to equal that of the original sine wave. The two signals are added to give a single sinusoid whose amplitude A and phase ϕ may be adjusted independently, as indicated in equation 8.1

$$x(t) = a\sin\omega t + b\cos\omega t = A\cos(\omega t + \phi) \tag{8.1}$$

The delay line includes values for the coefficients a and b such that the phase change around the actuator ring is equal to 6π, corresponding to a phase difference between adjacent loudspeakers of $6\pi/7$. In the absence of imperfections, the loudspeaker array will therefore excite the $m = -3$ mode, independent of frequency.

Loudspeaker characteristics

Figure 8.3 shows a photograph of the compression driver used in both primary and secondary loudspeaker arrays. These drivers are usually used to drive horn loudspeakers. They were chosen as their magnitude and phase response was expected to be fairly well matched. They are also easily mounted in the duct by a screw thread at the opening of the loudspeaker.

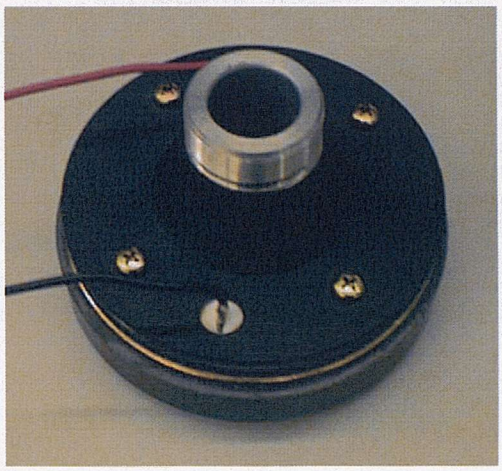

Figure 8.3: *Compression driver used for the mode synthesiser array and the control array*

The mode synthesiser used to generate the primary sound field is based on the assumption that the loudspeakers have identical magnitude and phase characteristics over the frequency range of interest. Of the 16 drivers purchased for the project, the 7 with the best-matched frequency response were selected to form the mode synthesiser ring. These were measured by placing a Bruel & Kjaer 1/2 inch microphone at the opening of the loudspeaker. The loudspeaker was driven with a white noise signal. The cross-spectrum $S_{xy}(f)$ was measured between the pressure signal and the excitation signal and also the power spectrum of the excitation signal $S_{xx}(f)$. These were used to deduce frequency response function of the loudspeaker obtained from the transfer function [4],

$$H(f) = \frac{S_{xy}(f)}{S_{xx}(f)} \tag{8.2}$$

The magnitude and phase plots for the 7 best matched loudspeakers are shown in figures 8.4 and 8.5 below. The vertical dashed lines contain the frequency bandwidth of interest in the experiment.

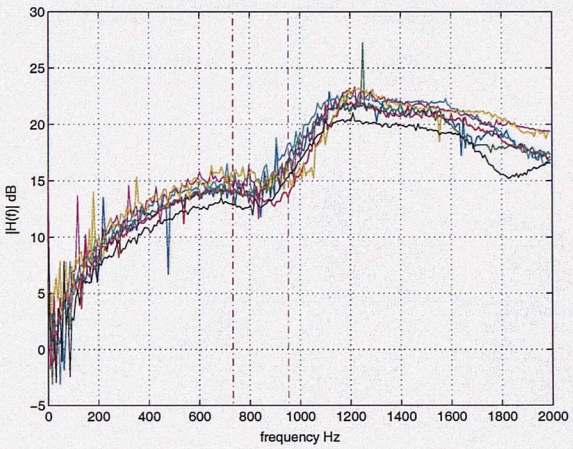

Figure 8.4: *Magnitude in dB of the frequency response function $H(f)$ for each loudspeaker in the mode synthesiser*

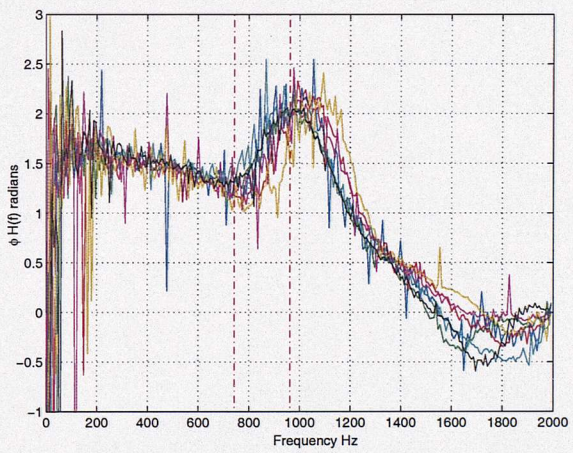

Figure 8.5: *Phase of the frequency response function $H(f)$ for each loudspeaker in the mode synthesiser*

The magnitudes of the loudspeakers' frequency responses are within 3dB over the frequency range of interest. The phase response of the loudspeakers are within 20° although this is difficult to see clearly due to random errors in the spectral estimate.

8.3.2 Modal analysis

In order to assess the performance of the mode synthesiser in exciting the $m = -3$ mode, a spinning mode decomposition was performed at the duct wall using the pressure signals measured at the error microphone array, using

$$\hat{a}_m(\omega) = \frac{1}{7}\sum_{l=1}^{7} p(\theta_l, \omega)e^{-im\theta_l} \tag{8.3}$$

The complex amplitude of the pressure signals $p(\theta, \omega)$ were obtained from the pressure time series $p(\theta, t)$ using the simple frequency correlation technique presented in appendix B.

Figure 8.6 shows the result of the spinning mode decomposition for each of the 14 excitation frequencies between 740Hz and 950Hz at which control was implemented. Due to loudspeaker mismatch and the finite size of the loudspeakers, all spinning mode orders are excited in the duct. However, the $m = -3$ mode is dominant at each frequency, and is approximately 10 to 20 dB above the level of the largest 'extraneous' mode. The term 'extraneous' is used here to indicate a mode other than the $(m = -3, n = 1)$ mode.

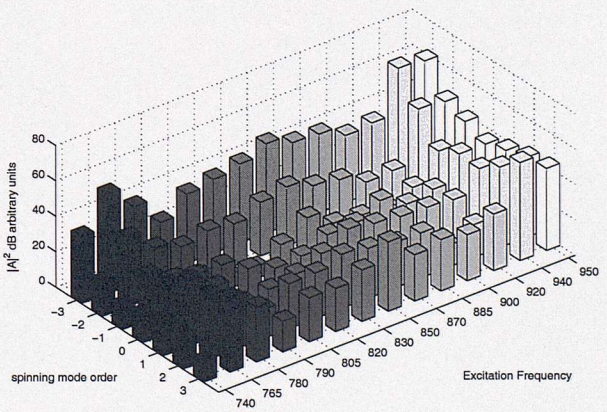

Figure 8.6: *Measured spinning mode decomposition at the wall at each excitation frequency*

8.3.3 The active control system

The following is a brief description of the hardware used to implement the active control.

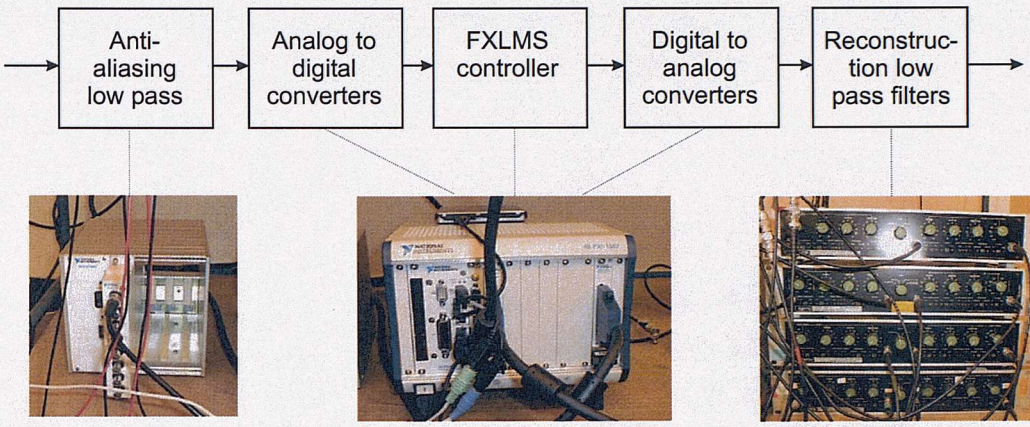

Figure 8.7: *Block diagram of the experimental rig*

Anti-aliasing filters

In order to avoid aliasing in the control system, one must remove all higher frequency signal components above the Nyquist frequency (Half the sampling frequency f_s). The low pass filters used to do this are 8th order elliptical low-pass filters housed in a National Instruments SCXI-1141 filter module, is shown in figure 8.7. At each frequency the anti-aliasing filters are set to have a cut-off frequency equal to the excitation frequency.

Analog to digital converters

The acquired analog signals were converted to digital signals using the 16-bit ADCs on the National Instruments PXI-6052E multifunction data acquisition card, as shown in 8.7

Digital to analog converters

The signal must then be converted back to analog signals in order to drive the loudspeakers. This digital to analog conversion is performed by the analog output card. The analog output card used is the National Instruments PXI-6733 which uses 16-bit DACs.

Reconstruction filters

After converting the digital signal to an analog signal, the resulting waveform will not be smooth but will be 'stepped'. 'Smoothing', or reconstruction filters, are therefore required in order to remove the high frequency harmonics which would be generated if this stepped waveform was output directly to the loudspeaker. KEMO type VBF/23 elliptical low-pass filters are used to 'smooth' the analog output signals. The reconstruction filters were less flexible than the anti-aliasing filters and therefore the cut-off frequency was set to 1kHz for the entire frequency range.

8.3.4 The filtered-reference LMS controller

Single channel example

The Filtered reference (Filtered-x) signal Least Mean Square (FXLMS) algorithm was implemented in real time to generate the control signals used to drive the actuator array. The commonly used [10, 41, 58] FXLMS algorithm is a modified version of the Least Mean Square (LMS) algorithm. The basic LMS algorithm adapts the coefficients of a Finite Impulse Response (FIR) filter such that a specified cost function is minimised. At each sample time the coefficients of the FIR filter are updated by an amount that is proportional to the instantaneous gradient of the cost function. This is usually defined as the instantaneous error measured at the microphone array.

The active control system of interest here may be represented by the following block diagram [45].

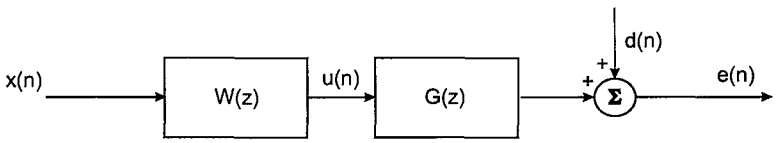

Figure 8.8: *Block diagram of the active control system*

In figure 8.8 $x(n)$ is a reference signal, which is a sinusoidal signal of the same frequency as the primary signal. In the figure, $W(z)$ represents the response of the adaptive FIR filter used to drive the secondary sources. The term $G(z)$ is the the acoustic response between the loudspeakers and the microphones in discrete form, commonly referred to as the plant model. The signal $d(n)$ is the primary disturbance signal which one is attempting to cancel, in this case the pressure at the microphone due to the primary sound field. The active control system can be assumed to be linear and time invariant [45] and therefore the ordering of the filters can be reversed to give the block representation shown in figure 8.9. The reference signal is now filtered through a sampled version of the acoustic response before being filtered using the adaptive FIR filter.

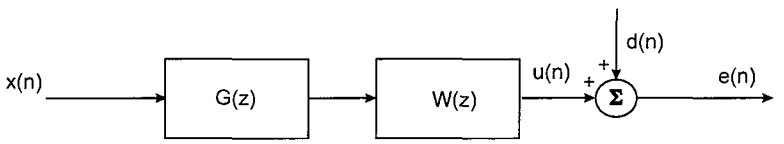

Figure 8.9: *Modified block diagram of the active control system*

For the active control system of interest here the error signal $e(n)$ is the sum of the pressure contributions from the primary source actuator and the secondary actuators. We seek to minimise this error signal by minimising the sum of the squared error signals at the error sensors. The error signal for an active control system with a single actuator, a single microphone and a single FIR filter with I coefficients is defined by the equation

$$e(n) = d(n) + \sum_{i=0}^{I} w_i r(n-i) \tag{8.4}$$

which can be written in vector form as

$$e(n) = d(n) + \mathbf{w^T r} \tag{8.5}$$

where $\mathbf{w}$ is a vector of filter coefficients. In this single frequency example, a two coefficient filter is sufficient. Here, $\mathbf{r}$ is a vector of the filtered reference signal for the current and previous samples.

$$\mathbf{w} = [w_0 \; w_i]^T \tag{8.6}$$

$$\mathbf{r} = [r(n) \; r(n-1)]^T \tag{8.7}$$

From equation 8.5 the instantaneous squared error at the microphone is given by

$$e^2(n) = \mathbf{w^T r r^T w} + 2\mathbf{w^T r}d(n) + d^2(n) \tag{8.8}$$

A vector of the instantaneous gradients of the cost function with respect to each of the filter coefficients in $\mathbf{g}$ is now defined as

$$\mathbf{g} = \left[\frac{\partial J}{\partial w_0(\mathrm{n})} \, , \frac{\partial J}{\partial w_1(\mathrm{n})}\right]^T \tag{8.9}$$

The instantaneous gradient may be used to update the filter coefficients. The general form of the LMS algorithm is therefore of the form

$$\mathbf{w}(\mathrm{n}+1) = \mathbf{w}(\mathrm{n}) - \frac{\alpha}{2}\mathbf{g} \tag{8.10}$$

where α is a convergence parameter, which determines the speed of convergence and is chosen to ensure the stability of the system. This will be discussed later in this chapter.

For the FXLMS algorithm, the instantaneous gradient of the cost function can be written

$$\mathbf{g} = 2\mathbf{w}\mathbf{r}\mathbf{r}^{\mathbf{T}} + 2\mathbf{r}d(\mathrm{n}) \tag{8.11}$$

which can be re-written,

$$\mathbf{g} = 2\mathbf{r}\left(d(\mathrm{n}) + \mathbf{w}\mathbf{r}^{\mathbf{T}}\right) \tag{8.12}$$

Noting that $e(\mathrm{n}) = d(\mathrm{n}) + \mathbf{w}\mathbf{r}^{\mathbf{T}}$ the gradient expression reduces to

$$\mathbf{g} = 2\mathbf{r}e(\mathrm{n}) \tag{8.13}$$

Therefore the FXLMS algorithm for a single channel can be written as

$$\mathbf{w}(\mathrm{n}+1) = \mathbf{w}(\mathrm{n}) - \alpha\mathbf{r}e(\mathrm{n}) \tag{8.14}$$

In a practical system, the acoustic response $G(z)$ which is used to calculate the filtered reference signal $\mathbf{r}$ is difficult to measure accurately and is thus only an estimate $\hat{G(z)}$ of the true response. In a practical system, therefore, the block diagram for the FXLMS algorithm is shown in figure 8.10.

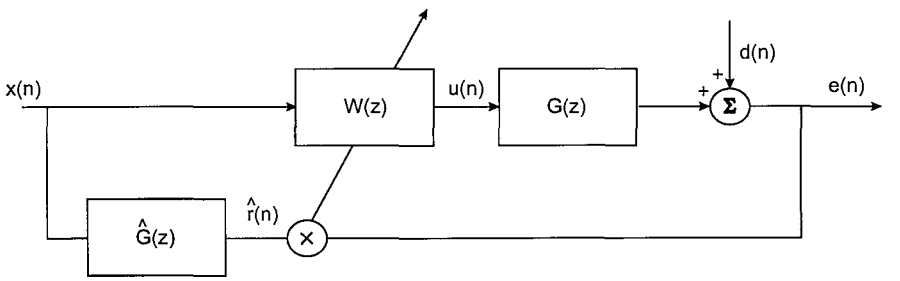

Figure 8.10: *Full block diagram of the practical FXLMS algorithm for a single channel system*

Multi-channel FXLMS algorithm

The above formulation for a single channel system can be generalised to the multi-channel case where there are multiple sources and sensors [19]. In this case, one obtains a vector of the error signals at the error sensor array $\mathbf{e}$ at a sample time n

$$\mathbf{e} = \mathbf{d} + \mathbf{R}\mathbf{w} \ , \tag{8.15}$$

where the vector $\mathbf{d}$ is the disturbance signal at the microphone array at sample time n. The matrix $\mathbf{R}$ is the filtered-reference signal matrix for all combinations of sources M and sensors L. The dimensions of this matrix are $L \times M \times I$, where I is the number of filter coefficients, which in the case of a tonal control system is equal to two [17].

At a single error sensor l, the error signal is therefore given by

$$e_l(n) = d_l(n) + \sum_{m=1}^{M} \sum_{i=0}^{2} w_{mi} r_{lm}(n-i) \tag{8.16}$$

The instantaneous gradient vector $\mathbf{g}$ in the multichannel case becomes

$$\mathbf{g} = 2\underbrace{(\mathbf{R}^{\mathbf{T}}\mathbf{R}\mathbf{w} + \mathbf{R}^{\mathbf{T}}\mathbf{d})}_{\mathbf{R}^{\mathbf{T}}\mathbf{e}} \tag{8.17}$$

and therefore the update equation for the multi-channel case is

$$\mathbf{w}(n+1) = \mathbf{w}(n) - \alpha\mathbf{R}^{\mathbf{T}}\mathbf{e} \tag{8.18}$$

Thus the update for a single filter coefficient is simply

$$w_{mi}(n+1) = w_{mi}(n) - \alpha \sum_{l=1}^{L} e_l(n)\hat{r}_{lm}(n-i) \tag{8.19}$$

The control signals which are output to the speakers can be updated at each sample time by filtering the reference signal using the current values of the filter coefficients. The control signal u_m(n) for the mth actuator is given by

$$u_m(n) = \sum_{i=0}^{2} w_{mi} x(n-i) \tag{8.20}$$

The filtered reference signals are usually generated by using a sampled estimate of the acoustic response between the loudspeakers and microphones. This plant model is estimated by measuring offline the transfer functions $H(f)$ between each source and sensor. We seek to control a tonal signal of a known frequency and thus the filtered reference signals can be inferred directly with no need for an external reference signal.

The reference signal $x(n)$ is a sinusoidal signal of the same frequency f as the primary disturbance

$$x(n) = \cos(2\pi f n T) \tag{8.21}$$

where T is the sampling period, $T = 1/f_s$. The control system will operate at a single frequency and thus the filtered reference signals can be inferred directly from knowledge of the magnitude and phase response between each actuator and microphone. The filtered reference signals at a sample time n for an actuator m and a sensor l will be of the form

$$\hat{r}_{lm}(n) = A_{lm} \cos(2\pi f n T + \phi_{lm}) \tag{8.22}$$

The magnitude A_{lm} and phase ϕ_{lm} of the transfer function between each loudspeaker m and microphone l can be measured simply by dividing the *complex* voltage signal measured at the sensor by the *complex* voltage driving the loudspeaker,

$$Z_{lm} = \frac{v_{in}(\theta_l)}{v_{out}(\theta_m)} = A_{lm} e^{i\phi_{lm}} \tag{8.23}$$

A matrix of single-frequency transfer functions can be measured offline and then used as an input to the control system. A control loop was programmed which 'simultaneously' acquires a voltage signal at each microphone and outputs a voltage to each loudspeaker. The processing steps involved in implementing the FXLMS algorithm at each sample time n are summarised below.

- The reference signal for the nth sample is generated,

$$x(\mathrm{n}) = \cos(\omega n T)$$

- The matrix of filtered reference signals $\mathbf{R}(n)$ is constructed using the amplitude and phase of the single frequency transfer function matrix $\mathbf{Z}$.

- The actuator signals are generated by filtering the reference signal $\mathbf{x} = [x(n) \;\; x(n-1)]^T$ using the current values of the filter coefficients $\mathbf{w}(n)$,

$$u_m(n) = \mathbf{w^T x}$$

- The error signal $\mathbf{e}(n)$ is the voltage signal measured at the microphone array. This is acquired for the nth sample and used together with the filtered reference signals to update the filter coefficients,

$$\mathbf{w}(n+1) = \mathbf{w}(n) - \alpha \mathbf{R^T e}(n)$$

  where $\mathbf{R} = [\mathbf{R}(n)|\mathbf{R}(n-1)]$.

8.3.5 Control system stability

The stability of the LMS algorithm can be determined by examining the eigenvalues of the autocorrelation matrix of the reference signal. In the case of the FXLMS algorithm, the stability is dependent on the eigenvalues of the cross-correlation between the plant model matrix $\mathbf{R}(n)$, which describes the acoustic path between the sources and sensors, and the estimated plant model matrix, measured offline, $\hat{\mathbf{R}}(n)$. For our tonal controller, only 2 coefficient filters are used in the plant model $G(z)$ and for the adaptive FIR filters

$\mathbf{w}$. For a single channel, the matrix $E\left\{\hat{\mathbf{R}}(n)\mathbf{R}(n)\right\}$ will have dimensions of 2×2. If the sampling rate is chosen such that there are 4 samples per cycle, the phase difference between samples will always be $\pi/2$ and thus if the estimate of the acoustic plant is perfect the matrix $E\left\{\hat{\mathbf{R}}(n)\mathbf{R}(n)\right\}$ will be symmetric, and will have equal eigenvalues. [17]

In chapter 4, the concept of 'modes of convergence' was discussed. The control system can be reduced to a set of independent 'modes' which all need to decay to zero in order for the error to go to zero. In the FXLMS algorithm the decay rate of the modes of convergence is inversely proportional to the eigenvalues of the matrix $E\left\{\hat{\mathbf{R}}(n)\mathbf{R}(n)\right\}$. Thus if these are equal then both modes will decay at equal rates. However, if the plant model is not identical to the actual plant response, then there may be modes which decay at different speeds.

The dominant factor that affects the conditioning and stability of the control system is the accuracy of the estimated acoustic plant matrix. Numerous studies have shown [8, 38, 19, 56] that the FXLMS algorithm is robust to errors in the plant model. It is shown that in both frequency domain [19] and time domain [56] analyses, in the single channel the phase is only required to be within $\pm 90°$ of the actual phase in order to ensure stability.

Boucher et al [8] show that the multi-channel system is almost as robust to errors in the plant model as the single channel case. They suggest that in order to guarantee stability the convergence parameter α must satisfy

$$\alpha < \frac{2\sigma_m}{|\lambda_m|^2} \tag{8.24}$$

where λ_m is the mth eigenvalue of the matrix $E\left\{\hat{\mathbf{R}}(n)\mathbf{R}(n)\right\}$ and $\sigma_m = \Re\{\lambda_m\}$.

Therefore, in order to achieve stability and fast convergence, the matrix $E\left\{\hat{\mathbf{R}}(n)\mathbf{R}(n)\right\}$ is required to have real and positive eigenvalues. The effect of errors on the plant model is investigated experimentally by Elliott et al [19]. By adding random numbers to the elements in the plant model matrix, they observe the resulting convergence behaviour.

The system converges in two stages, with one quickly converging mode and another more slowly diverging mode. This suggests the presence of a smaller negative eigenvalue and thus the control system is unstable. One way to avoid this instability is to ensure that all the eigenvalues are positive and real by adding a 'leak' to the FXLMS algorithm. This has the effect of adding a small value to the eigenvalues of the matrix $E\left\{\hat{\mathbf{R}}(n)\mathbf{R}(n)\right\}$ and effectively 'regularising' the $E\left\{\hat{\mathbf{R}}(n)\mathbf{R}(n)\right\}$ matrix. The addition of this effort weighting term, however, has the effect of limiting the pressure reduction at the error sensors, and hence degrades control performance. The 'leaky' FXLMS algorithm takes the form of

$$\mathbf{w(n+1)} = (\mathbf{1} - \alpha\beta)\mathbf{w(n)} - \alpha\mathbf{r(n)e(n)} \tag{8.25}$$

where β is the leakage term, exactly analogous to the regularisation parameter described in chapter 4.

8.4 Preliminary active control performance results

The active control system was implemented in real-time to control the spinning mode $m = -3$ generated by the mode synthesiser. As was mentioned earlier in this chapter, the theory suggests that the control system will only control, without spillover, of the modes $-3 \leq m \leq 3$. However, spillover into the $m = -4$ mode will be shown in chapter 9 to affect the power reduction significantly even though the pressure is considerably reduced at the error sensors. Thus the frequencies were chosen to be in the range extending from the cut-on frequency of the $(-3, 1)$ at 764Hz to the cut-on frequency of the $(\pm 4, 1)$ at 967Hz.

A value for the convergence parameter α was chosen arbitrarily to guarantee that the error converged to zero without going unstable. The convergence parameter used was of the order of 1×10^{-5}. This value of α appears to be very small and suggests that the system is potentially unstable and thus needs to converge slowly in order to maintain stability. However, as can be seen in figure 8.11, the control system converges in typically less than

one second. It is more likely therefore that the small value of α required is due to the fact that the reference signal is of a different magnitude than that of the measured value of the error signal. Thus the convergence coefficient is required to be small to overcome the difference in level.

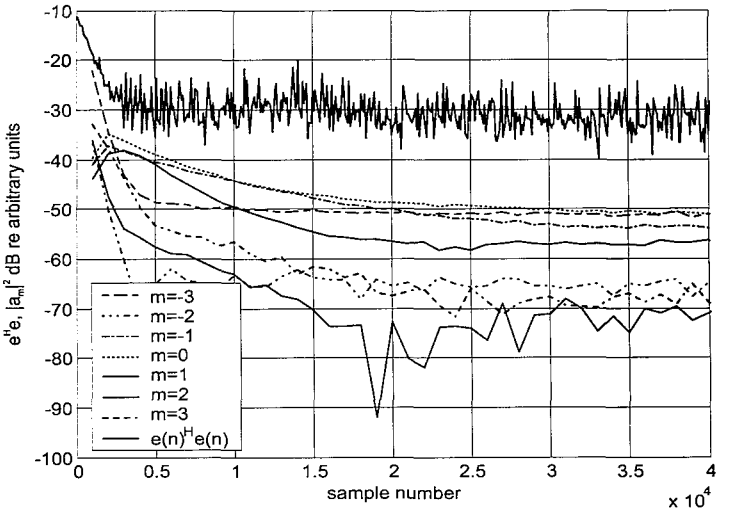

Figure 8.11: *Convergence of the control system at 830Hz*

The bold curve in figure 8.11 shows the variation of the mean squared error signal over time. An initial decay of approximately 20dB is achieved within approximately 3000 samples. At the frequency of 830Hz the sampling frequency f_s is approximately $3320Hz$ which equates to 4 samples per cycle. After this initial period, the error continues to decay very slowly, eventually giving a further 2-3dB reduction over the next 40,000 samples. This behaviour suggests that there is a slow mode of convergence and that the plant model may not be exact. However, for the purposes of our control experiment the intial convergence is sufficient to determine the associated sound power reduction achieved. Also plotted in figure 8.11 are levels of the estimated spinning mode amplitudes at the error sensors averaged over 1000 samples. The dominant mode $m = -3$ is observed to decay by approximately 30dB in the initial 5000 samples.

8.5 Conclusions

- The design of a real-time active control system has been presented.
- The primary 'buzz-saw' mode $m = -3$ is synthesised using an array of 7 actuators with a phase change of $6\pi/7$ around the array.
- An FXLMS algorithm is used to minimise the sum of the squared pressures at 7 microphones using 7 loudspeakers.
- The stability of the control system is dependent on the transfer function estimates.

Chapter 9

Discussion of Experimental Results

9.1 Introduction

In the previous chapter the implementation of a conventional real-time control system was described aimed at controlling the $m = -3$ single frequency spinning mode. This was achieved using an FXLMS algorithm to minimise the sum of the squared pressures at a single ring of seven microphones using a single ring of seven control actuators. This chapter will examine the results obtained from the procedure in more detail and explain how the results relate to the mechanisms of control identified earlier in this thesis. In particular, the relationship between pressure reduction at the error sensors and the reduction in transmitted sound power is investigated experimentally in the test rig discussed in chapter 8. Explanations of these findings are presented using computer simulations of the test rig.

In order to quantify the global performance of the active control system, the sound power radiated from the inlet of the duct was measured before and after control.

9.2 Pressure reduction at the error sensors

Convergence of the control system was assumed to occur when the microphone signals displayed on the oscilloscopes reduced to the level of the background noise. The microphone signals were recorded before and after control for subsequent processing in order to determine the reduction in the individual spinning mode amplitudes. These results will be examined later in the chapter as a means of understanding the control mechanism.

The reduction in the sum of the squared pressures recorded at the microphone array after control is shown in figure 9.1 for each of 14 excitation frequencies investigated between 740Hz and 950Hz. The microphone array is positioned 1.4m from the 'exhaust' termination of the duct, as shown in figure 8.1.

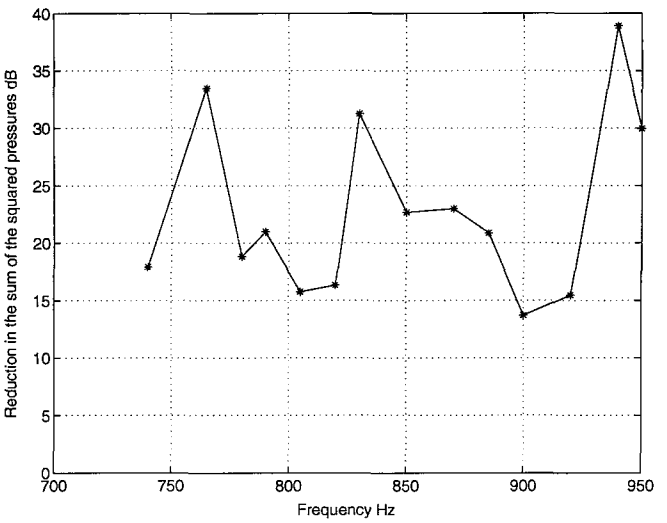

Figure 9.1: *Reduction in the sum of the squared pressures measured at the error sensor array after control versus frequency.*

Pressure reductions across the frequency range vary from 14dB in the worst case at 900Hz to 39dB at 940Hz. This variation is likely to be due to the accuracy of the transfer function measurements at each frequency and the signal to noise ratio at the error sensors. We shall now examine the corresponding sound power reduction obtained by integrating the normal component of intensity over the duct face (see figure 9.2) before and after control.

9.3 Sound power reduction

In order to calculate the sound power radiated from the duct 'inlet', the duct cross section was divided into a grid of 16 sections, as shown below in figure 9.2. An intensity probe was used to measure the area-averaged intensity $\langle \bar{I}_n \rangle_i$ flowing normally across each area section.

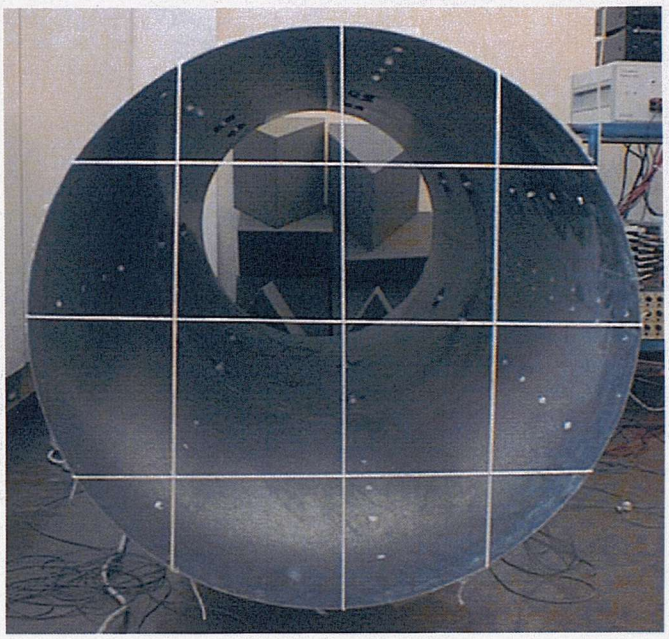

Figure 9.2: *The 16 section grid over which sound intensity was measured*

This was achieved by scanning the probe across the section and computing the space-time average $\langle \bar{I}_n \rangle_i$ $(i = 1 - 16)$. The sound power radiated from the duct section is deduced by multiplying the intensity measurements by the area of the respective grid section ΔS_i and summing.

$$\bar{W} = \sum_{i=1}^{16} \langle \bar{I}_n \rangle_i \Delta S_i \tag{9.1}$$

The variation in sound power reduction with frequency is plotted in figure 9.3 below with the error sensor array positioned closest to the secondary source array, as shown in 8.1. The vertical dashed lines denote the cut-off frequencies of the $(\pm 3, 1)$ and $(\pm 4, 1)$ modes. The

vertical solid lines denote the variations in predicted performance based on an estimated uncertainty in the amplitudes of the two axi-symmetric radial modes, which as we shall show in section 9.3.1 is one of the main factors in determining the power reduction in this test rig.

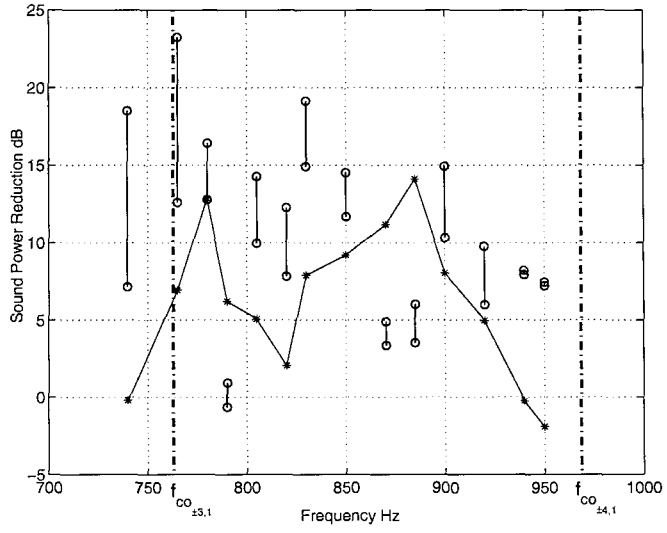

Figure 9.3: *The variation of sound power reduction following the minimisation of the sum of the squared pressures. The asterisks show the measured sound power reduction after control. The dotted vertical lines show the cut-on frequencies of the (-3,1) and (-4,1) modes. The vertical solid lines show the variation in predicted sound power reduction with varying levels of the axi-symmetric* $(0,1)$ *and* $(0,2)$ *modes*

The measured sound power reductions are seen to be highly frequency-dependent and unrelated to the frequency variations in pressure reduction plotted in figure 9.1. Reductions in sound power are obtained at all frequencies apart from at 740Hz, 940Hz and 950Hz, where small increases in sound power are observed.

The main reason for poor control performance at the two highest frequencies, is the presence of the $m = \pm 4$ modes, which at these frequencies are very close to cut-on, and will therefore have a significant ampltiude at the error sensors. These cannot be independently controlled due to insufficient numbers of sources and sensors.

9.3.1 Predicted sound power reduction

In figure 9.3 the vertical bars show the range of predicted power reductions at each frequency. The inputs to the model are the relative levels of the measured spinning mode amplitudes. All spinning mode orders $m \neq 0$ over the frequency range between 740 and 950Hz comprise a single propagating radial mode, whereas at $m = 0$ there are two propagating radial modes $(0,1)$ and $(0,2)$. Their amplitudes cannot be deduced from the single ring of measured pressure data. To allow for the uncertainty in the mode amplitudes $a_{p_{0,1}}$ and $a_{p_{0,2}}$, the bars show the variation in the predicted power reduction for varying ratio of $\frac{a_{p_{0,1}}}{a_{p_{0,2}}}$ between 10 to 0.1, whilst keeping $\hat{a}_{p_{0,1}} + \hat{a}_{p_{0,2}} = \hat{a}_{p_0}$, which is known from modal analysis of the measured data. The predicted power reduction is overestimated by between 5 to 10dB at most frequencies. The main reason for this is believed to be due to imperfect cancellation of the pressure at the error sensors. Another possible explanation for the overestimation is that the model assumes the duct walls are rigid. The duct rig is made of thin sheet metal and acoustic-structural interaction is likely to cause a small amount of noise to 'breakout' or radiate from the walls of the duct section. Anomalous results occur at the frequencies of 790Hz, 870Hz and 885Hz, where the predicted power reductions are poorer than those measured. The reason for this is currently not understood and is being investigated.

9.4 Modal decomposition for the interpretation of the control mechanism at the error sensors

At each of the frequencies at which control was implemented, the pressure signals at the error microphones were processed to determine the amplitudes $\hat{a}_m$ of the spinning mode orders at the duct wall. The complex pressure signals at the microphones $p(\theta_l, \omega)$,(l =1 to 7) were deduced from a measured pressure time series $p(\theta_l, t)$ over 1000 samples, corresponding to $T_s \approx 0.3s$ of data at 885Hz, following the procedure detailed in appendix B. A spinning mode decomposition of the sound field at the duct wall was then performed, before and after control, using

$$\hat{a}_m(\omega) = \frac{1}{7}\sum_{l=1}^{7} p(\theta_l, \omega) e^{-im\theta_l} \tag{9.2}$$

Application of the Nyquist theorem to spatially sampled sound fields, suggests that this operation allows the unambiguous decomposition of modal amplitudes for modes in the range $-3 \leq m \leq 3$. Higher order spinning modes present in the sound field will therefore be aliased, and hence will contaminate the measurement in the range of m for which it is valid. Modal decomposition results are shown in figure 9.4 at a frequency of 885Hz.

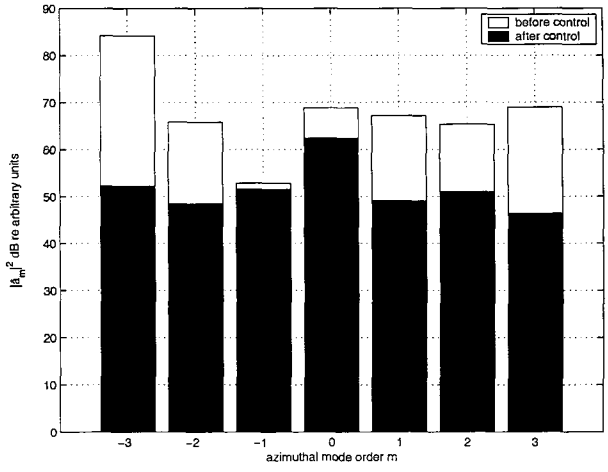

Figure 9.4: *Measured spinning mode amplitudes at the duct wall before and after control at 885Hz*

Before control, $m = -3$ is the dominant mode with a level 15dB greater than the other modes. After control, all spinning mode amplitudes appear to have been reduced, such that the axisymmetric $m = 0$ mode now dominates the sound field at the error sensors. At this frequency, the sound power is reduced by 14.5dB The measured modal decomposition is plotted in figure 9.5 for the higher excitation frequency of 950Hz. It shows that all spinning mode amplitudes have been reduced. However, figure 9.3 shows that in this case the sound power actually increases after control by approximately 2dB.

The important difference in these results at the higher frequency compared with the results at 885Hz in figure 9.4 is that now the $m = \pm 4$ modes with a cut-on frequency of 967Hz are now much closer to cut-on. At 950Hz, the cut-off ratio of the $m = \pm 4$ spinning

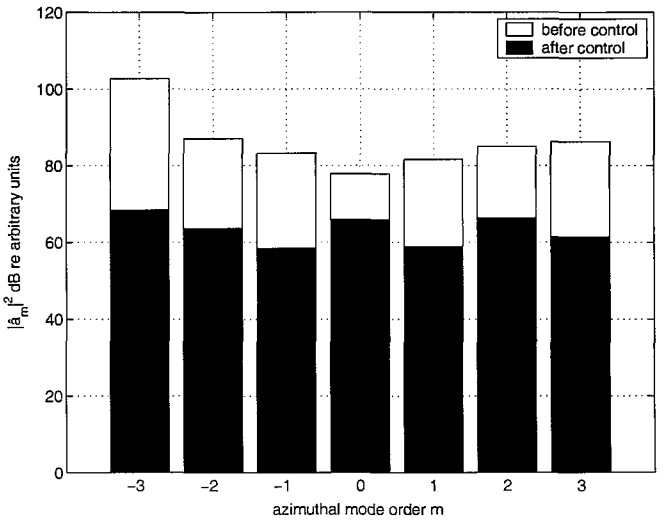

Figure 9.5: *Measured spinning mode amplitudes at the duct wall before and after control at 950Hz*

modes is $\zeta = 0.98$ and hence these modes decay very slowly along the duct by only 14dB between the secondary source and the error sensors. The control system will attempt to control this mode in order to cancel the pressure at the error sensors. However, due to an insufficient number of sources, the $m = \pm 4$ modes cannot be excited independently of the other (principally the $m = \pm 3$) modes. Moreover, due to an insufficient number of sensors the $m = \pm 4$ modes appear at the control system as a lower order mode. Thus, the $m = \pm 4$ cut-off modes are essentially aliased and control performance is degraded. Further discussion of this process is given in section 9.5

Figures 9.6(a) and 9.6(b) show a comparison between the measured spinning mode amplitudes after control at 950Hz and that predicted using the model with the measured spinning mode amplitudes input to the model. Although the predicted sum of squared pressures is zero, as predicted from equation 5.3 (of the order $-300dB$), the *measured* spinning mode amplitudes are not driven perfectly to zero, but attenuated by between 10 and 30dB.

Two main differences can be observed between the predicted and measured spinning mode amplitudes. Firstly, the predicted levels of the $m = \pm 3$ modes are much higher than the

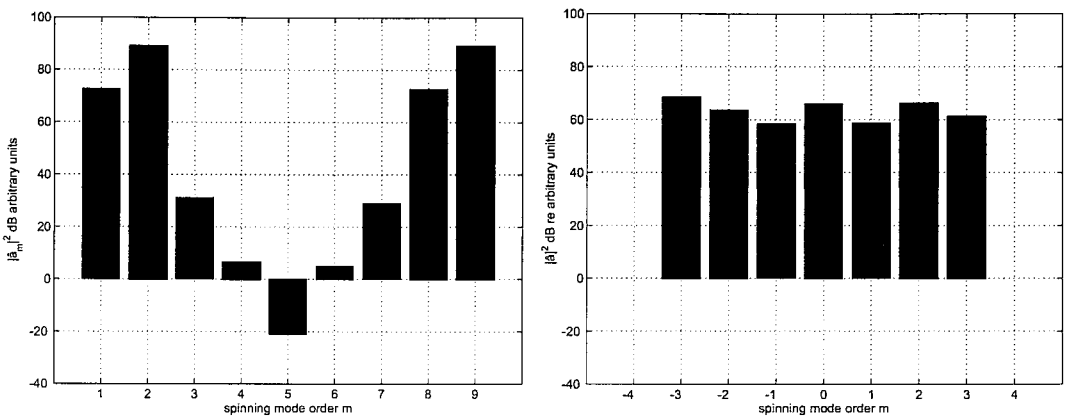

(a) (b)

Figure 9.6: *Comparison between predicted spinning mode amplitudes using the theoretical model (a) and measured spinning mode amplitudes (b) at 950Hz*

measurements by up to 25dB. This is due to the level of the $m = \pm 4$ mode being aliased into the lower order modes. Secondly, the predicted amplitudes of the $m = \pm 1$ and $m = 0$ modes are substantially lower than those measured. This is believed to be because the pressure at the error sensors is only reduced by 20-30dB whereas the prediction assumes perfect cancellation.

A comparison between figures 9.6(a) and 9.6(b) makes clear that the measured spinning mode amplitudes at the duct wall using insufficient sensors are not a reliable indication of the actual level of these spinning modes at the error sensors *after* control, when higher order extraneous modes are present. The measured $m = \pm 3$ mode amplitudes are therefore an underestimate of its actual level. The important finding from these two measurements is that at 885Hz, the axi-symmetric $m = 0$ mode dominates the sound field after control, whereas at the higher frequency of 950Hz, the $m = 0$ and the $m = \pm 4$ modes are equally important.

Note that aliasing is not such a problem in the modal decomposition before control, however, as the primary source is further away from the error sensors and the $m = \pm 4$ modes decay to significantly lower levels at the error sensors, as will be verified from computer predictions presented later in this chapter.

9.5 Control mechanism at the error sensors

In order to understand more fully the relationship between sound pressure reduction and sound power reduction, the individual mode amplitudes at the error sensors after control are predicted using the theoretical model. Figure 9.7(a) shows the predicted mode amplitudes at 885Hz of the first and second radial mode orders at the wall for $-4 \leq m \leq 4$. Figure 9.7(b) shows $\hat{a}_m$, the sum of the radial mode orders of each spinning mode, obtained using the theoretical model.

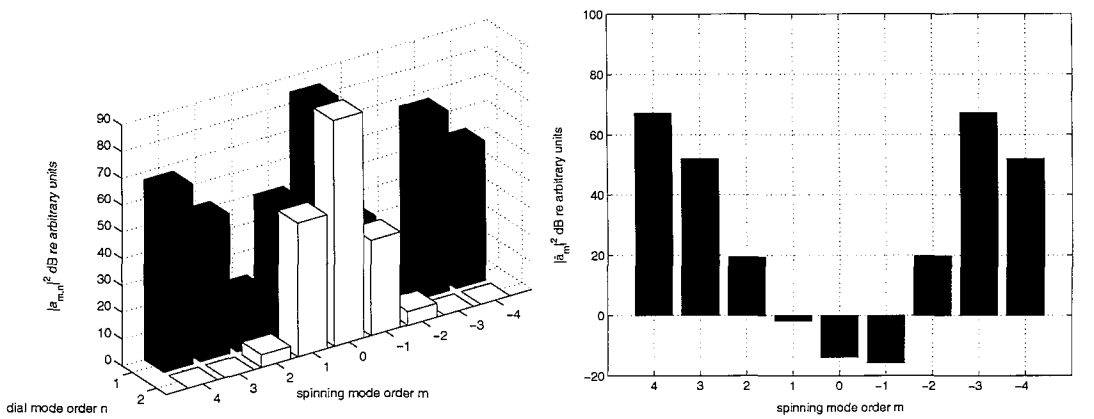

(a) (b)

Figure 9.7: *Predicted mode amplitudes at the error sensors (a) and the sum of the radial mode amplitudes (b) at the error sensors after control at 885Hz*

These predictions show two main features. One is the appearance of high amplitude ($m = \pm 4, n = 1$) modes. The other is the dominance of the axi-symmetric radial modes $(0,1)$ and $(0,2)$, associated with $m = 0$. Consistent with equation 5.5, figure 9.7(b) shows that $\hat{a}_0 = 0$ and hence the two radial modes must be driven so that their amplitudes exactly cancel, $\hat{a}_{0,1} = -\hat{a}_{0,2}$. Both of these modes are cut on and therefore carry sound power. It is therefore the level of these modes which in this experiment dominates the sound power after control at this frequency.

Far less important to control performance are the two radial mode amplitudes associated with the $m = \pm 1$ spinning modes, which also cancel at the error sensors, i.e. $\hat{a}_{1,1} + \hat{a}_{1,2} = 0$, even though the radial mode $(1,2)$ is just cut-off. Their amplitudes are therefore equal at

the error sensor array. Beyond the error sensor array, the evanescent mode decays away, whilst the propagating mode remains at constant level.

The most intriguing feature of figure 9.7 is that $\hat{a}_4 = -\hat{a}_{-3}$ and $\hat{a}_3 = -\hat{a}_{-4}$. Thus it appears that since the $\hat{a}_4$ mode cannot be controlled independently, the pressure at the error microphones is driven to zero by arranging for the amplitudes of $\hat{a}_4$ and $\hat{a}_3$ to cancel.

This behaviour can be explained by examining how the evanescent $m = \pm 4$ mode is aliased by the control system.

The use of 7 microphones assumes periodicity in the spinning mode spectrum such that

$$\hat{a}_m = \hat{a}_{m+7l} \qquad (l = -\infty \ldots 0 \ldots \infty) \tag{9.3}$$

If we take the actual spectrum after control for 885Hz shown in figure 9.7(b) comprising the modes $-4 \leq m \leq 4$, then the 'measured', aliased spectrum will be of the form

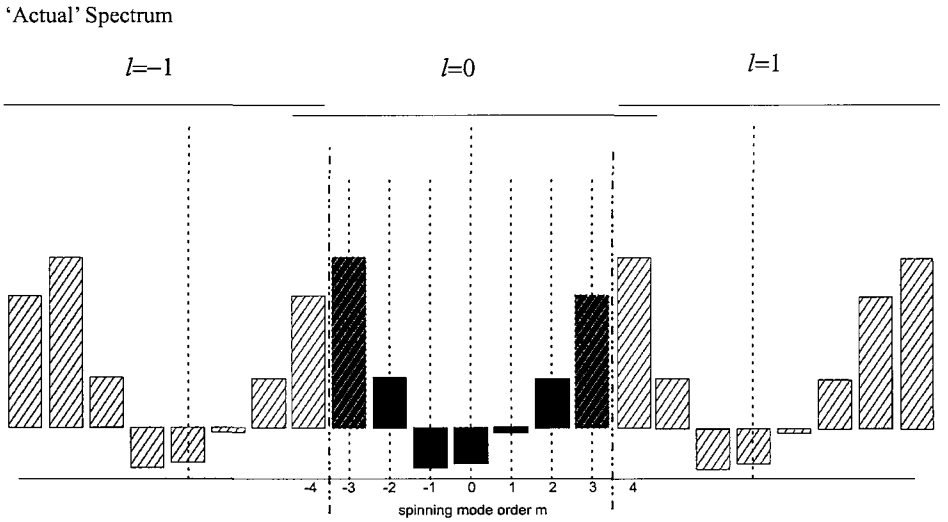

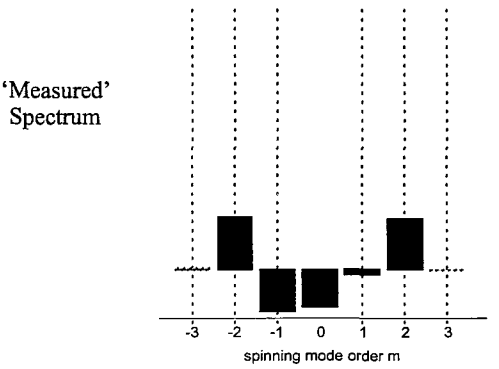

Figure 9.8: *The 'measured', aliased spectrum of spinning mode amplitudes after control at 885Hz*

Thus,

$$\begin{aligned} \underbrace{\hat{a}_3}_{measured} &= \underbrace{\hat{a}_3 + \hat{a}_{-4}}_{actual} \quad (l=-1) \\ \underbrace{\hat{a}_{-3}}_{measured} &= \underbrace{\hat{a}_{-3} + \hat{a}_4}_{actual} \quad (l=1) \end{aligned} \tag{9.4}$$

In order to drive the 'measured' spinning mode amplitude $\hat{a}_{\pm 3}$ to zero, the actual amplitudes are arranged such that

$$\begin{aligned} \hat{a}_3 + \hat{a}_{-4} &= 0 \\ \hat{a}_{-3} + \hat{a}_4 &= 0 \end{aligned} \tag{9.5}$$

The modal interpretation of the control mechanism involved in the cancellation of the pressure at the error sensors in the experimental duct has been shown to be surprisingly subtle. It may be summarised as follows:

a) The amplitudes of the $m = \pm 4$ modes are excited in order to cancel with the $m = \pm 3$ mode. The pressure is driven to zero by arranging for $\hat{a}_4 = -\hat{a}_{-3}$ and $\hat{a}_3 = \hat{a}_{-4}$ at

the error sensor plane. This is because the $m = \pm 4$ modes cannot be controlled independently by the seven sources and sensors of the control system.

b) The amplitudes of the $m = 0$ modes are arranged to cancel, $a_{0,1} = -a_{0,2}$, since the two radial modes associated with $m = 0$ cannot be independently controlled by the single ring of sources and sensors. The same process occurs for $m = \pm 1$ so that $a_{\pm 1,1} = -a_{\pm 1,2}$, even though the $a_{\pm 1,2}$ modes are cut-off.

It should be noted that the predictions for power reduction assume that the pressure is driven exactly to zero at the error sensor array. In practice, however pressure reductions are limited to between 10dB and 40dB. Nevertheless, evidence will be presented in the following sections that control mechanism discussed above is still relevant to the experimental rig.

9.6 Sound intensity distribution before and after control

9.6.1 Control at 885Hz - good control performance

Figure 9.3 shows that the largest sound power reduction of 14dB is observed at a frequency of 885Hz. (At the time of writing it is unclear as to why this is the case and this is currently being investigated). The change in intensity distribution across the duct face following control yields information that is useful for the interpretation of the control mechanism. The acoustic intensity distribution flowing across the duct 'inlet' at this excitation frequency before and after control is plotted in figures 9.9(a) and 9.9(b). Before control, the acoustic energy is concentrated close to the duct walls. This provides some evidence for the presence of the first radial mode order $n = 1$, as shown in figure 2.4.

Figure 9.9(b) confirms that after control the intensity at the duct walls has reduced by approximately 15dB, commensurate with the power reduction of 14dB. Furthermore, the radial variation of sound intensity is now significantly smaller compared with that before control suggesting that after control there is no longer a single radial mode order mode

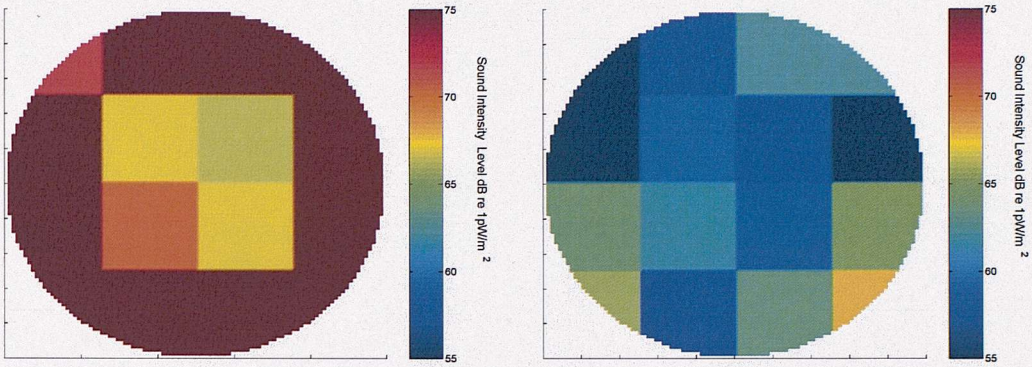

(a) (b)

Figure 9.9: *Measured sound intensity distribution before control (a) and after control (b) at 885Hz*

dominating the sound field in the duct, as confirmed by the predicted mode amplitudes in figure 9.7(a).

9.6.2 Control at 950Hz & 740Hz - poor control performance

The intensity distribution over the duct face at 950Hz before and after control, where the total power has *increased* by 2dB, is plotted in figures 9.10(a) and 9.10(b). Once again, before control there is evidence of the $n = 1$ mode as indicated by the localisation of energy close to the duct wall. However, a very similar intensity distribution is also observed after control, but is now marginally increased.

The likely explanation for this finding, as predicted by figure 9.6 is that at this frequency, the $(4, 1)$ mode is close to cut-on with a cut-off ratio of $\zeta \approx 0.98$. It will therefore make a more significant contribution to the pressure compared with at the lower frequencies. It was identified in the following section that in order to cancel the pressure to zero the control system excites the $m = \pm 3$ and $m = \pm 4$ modes such that $\hat{a}_4 = -\hat{a}_{-3}$ and $\hat{a}_3 = \hat{a}_{-4}$ at the error sensor plane. At a frequency of 950Hz where the $m = \pm 4$ modes are close to cut-on, this mechanism will dominate the sound power after control. Thus, the energy will be localised at the duct wall both before and after control.

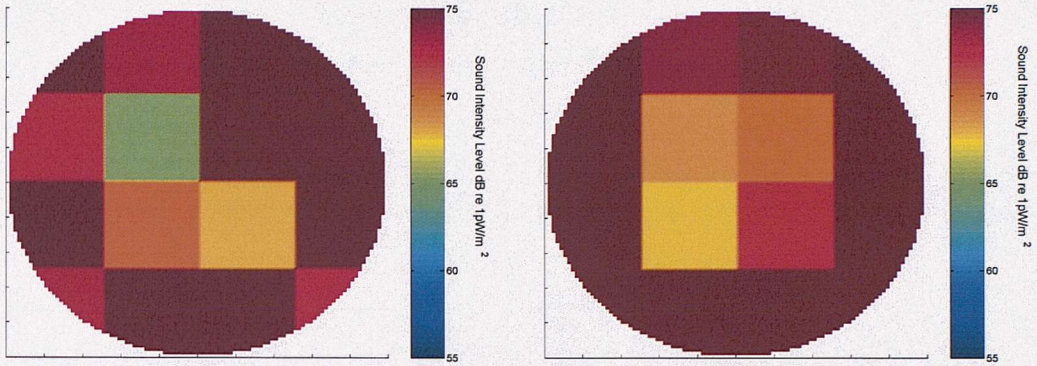

(a) (b)

Figure 9.10: *Measured sound intensity distribution before (a) and after (b) control 950Hz*

The sound intensity distribution before and after control at 740Hz is plotted in figures 9.11(a) and 9.11(b), for which the power is increased by approximately 1dB. Very little variation over the duct cross section is observed both before and after control.

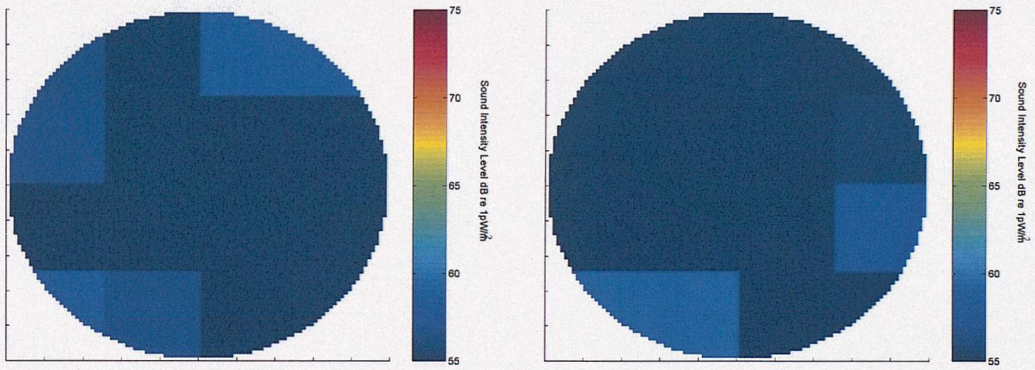

(a) (b)

Figure 9.11: *Measured sound intensity distribution before (a) and after (b) control 740Hz*

The likely explanation for poor control performance at this frequency of 740Hz is that the $(-3, 1)$ mode is cut-off ($\zeta = 0.97$). This mode will transmit very little power in comparison to the extraneous modes ($m < \pm 3$), which are also inadvertently excited. The small variation in intensity across the duct face, before control, plotted in figure 9.11(a) suggests that the axi-symmetric $m = 0$ mode is dominant. The axi-symmetric mode contains two propagating radial modes which cannot be independently controlled by the

single-ring control system. These modes will therefore also dominate the sound power after control resulting in very little, or no, reduction in sound power.

9.7 Axial variation in sound pressure reduction along the duct

In order to further investigate the mechanism of control, the sound pressure level was measured at a microphone positioned at 5cm intervals along the length of the duct at the duct wall, both before and after control.

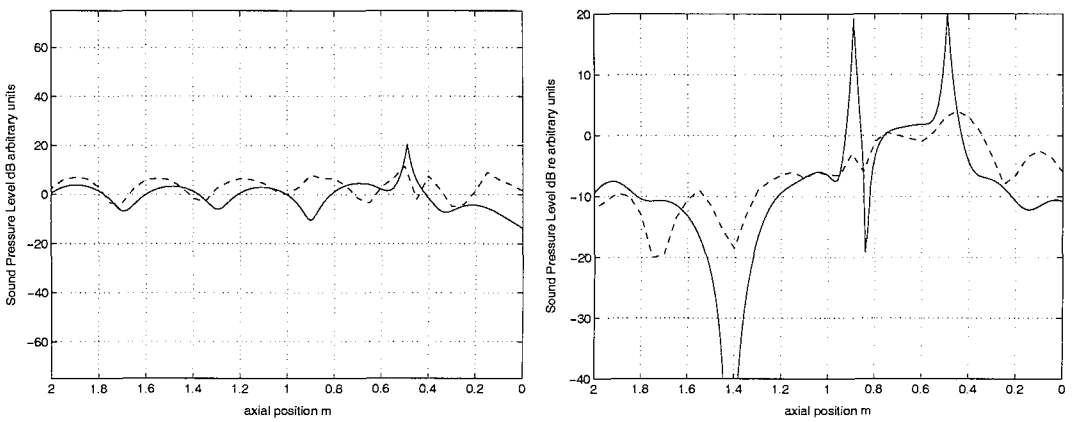

(a) (b)

Figure 9.12: *Comparison of measured (dotted line) and predicted (solid line) sound pressure level before control (a) and after control (b) at 885Hz with* $x_e = 1.4$

Figures 9.12(a) and 9.12(b) show a comparison between the measured and predicted axial variation of sound pressure levels at 885Hz, before and after control, respectively. This prediction was obtained by assuming modal amplitudes for the primary field $\hat{a}_m$ to be identical to those measured before control (figure 9.4). The radial modes associated with the axi-symmetric $m = 0$ mode are assumed to be of equal amplitude. The prediction code is modified such that the primary monopole sources behave similarly to the secondary sources and radiates in both directions along the duct (recall that it was assumed that the primary field only radiates initially towards the duct inlet). The microphone used for

the measurements was not calibrated. The absolute levels have therefore been adjusted such that the 'shape' of the pressure distribution can be compared. The comparison of the SPL before control shows reasonable agreement between the measured and predicted axial variation of SPL thus providing some verification of the accuracy of the theoretical model described in chapter 3.

The measured sound pressure level reduction at a frequency of 885Hz along the duct wall is plotted (dashed line) in figure 9.13. Also plotted (solid line) is the predicted sound pressure level reduction obtained using the theoretical model described in chapter 3.

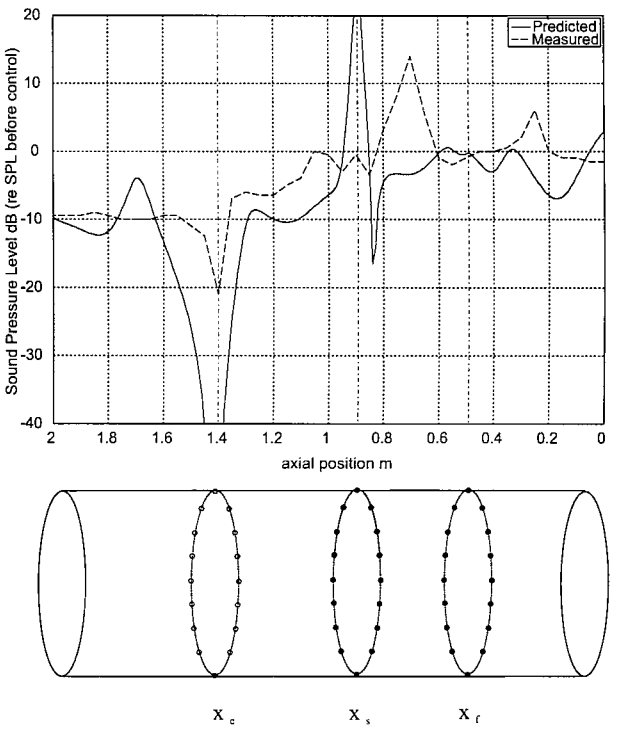

Figure 9.13: *Comparison of measured and predicted sound pressure reduction at 885Hz with varying axial position*

In this example, predictions are found to be in reasonable qualitative agreement with measurements. Different regions of behaviour are observed as follows:

- Region: $x > x_s$ Both experiment and prediction show that the sound pressure level is reduced at all locations forward of the secondary source array.

- Region: $x < x_s$ Small pressure reductions are produced between the 'exhaust' at $x = 0$ and the secondary source. Large increases in pressure level are also measured in this region, particularly at 0.7m where the sound pressure level is increased by 14dB.

- Region: $x_s \leq x \leq x_e$ The sound pressure level reduction forward of the secondary sources does not drop sharply, as would be predicted based on primary sound fields comprising only propagating modes, but appears to 'decay' gradually, and then suddenly drop to a minimum level at the error sensors.

- Region: $x > x_e$ Forward of the sensor array the predicted sound pressure reduction rises to a roughly steady level of about -10dB.

This behaviour is consistent with the control mechanism proposed in section 9.5, in which the axi-symmetric radial modes are excited so as to cancel at the error sensors, and the amplitudes of the $m = \pm 3$ and $m = \pm 4$ modes are excited such that they cancel at the error sensor array. In further support of this hyposthesis, figure 9.14 shows the predicted axial variation of sound pressure level after control, together with the predicted levels of the $(0,1), (0,2)$, $(\pm 3, 1)$ and $(\pm 4, 1)$ modes in the duct.

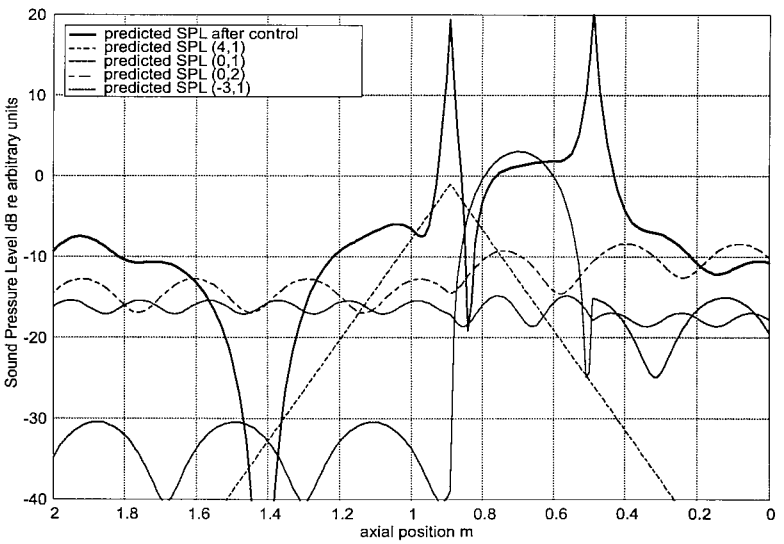

Figure 9.14: *The predicted level of the modes after control at 885Hz*

Note that the $(4,1)$ and $(-3,1)$ modes have identical magnitude at the plane of the error

sensors, as do the $(0,1)$ and the $(0,2)$ modes. The figure shows that the rate of decay of sound pressure reduction close to the secondary source array roughly follows the decay of the $(4,1)$ evanescent mode. Furthermore, the level of the sound field between the inlet and the error sensors is dictated by the level of the $m = 0$ mode after control. It appears that the level of the evanescent modes $m = \pm 4$ are much lower than that of the propagating axi-symmetric mode at the error sensors. These propagating modes will therefore dominate the pressure, and therefore, the sound power at the duct termination. It is clear, however, that at higher frequencies (but below its cut-off frequency) the $m = \pm 4$ modes will decay more slowly and may adversely affect control performance. Both of these situations will be investigated later in the chapter.

The axial variation of the $(-3,1)$ 'buzz-saw' mode follows closely the behaviour described in chapter 5, even though extraneous modes are present. It was shown in chapter 5 that the level of the dominant 'buzz-saw' mode is only reduced forward of the secondary source array. Between the secondary source array and the exhaust termination the buzz-saw mode radiated backward from the secondary sources will be unattenuated. As described in section 5.2.6 the control system in the time-domain controls subsequent reflections setting up a standing wave field in this region of the duct.

9.8 Variation in sound pressure reduction around the duct wall in the plane of the error sensors

The sound pressure level was measured before and after control at positions along the circumference of the duct wall between two adjacent error sensors. Measurements were taken at increments of approximately 3cm. Whilst the predicted pressure at the error sensor is zero, the measured reductions are limited to 16dB in this case. Furthermore, the minimum reductions at the wall differ by approximately 20dB. Nevertheless, both measurement and predicted reductions indicate variation in SPL that are slightly skewed 'to the right', due to a particular combination of interfering spinning modes.

According to the DFT argument proposed in chapter 5, in the absence of aliased modes,

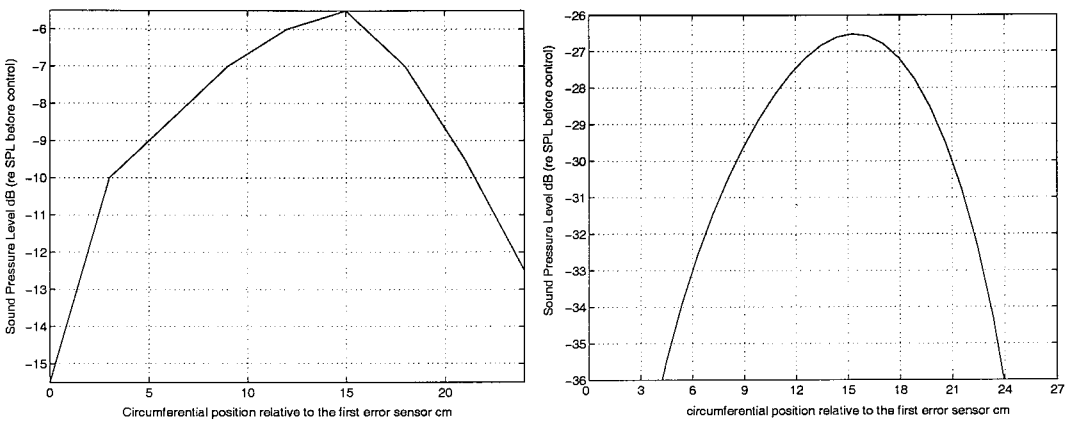

(a) (b)

Figure 9.15: *measured (a) and predicted (b) pressure reductions at circumferential positions between two adjacent error sensors*

the pressure along the duct wall is predicted to be roughly constant and equal to the level at the error sensor. However, at circumferential positions away from the error sensors, the measured sound pressure reduction varies by as much as 10dB. This further suggests the presence of aliased higher order modes. These modes were identified in the previous section as the $m = \pm 4$ spinning mode, which is inadvertently excited by the secondary actuators.

9.9 Sound power reduction with varying source-sensor separation distance

In this section we investigate the variation of power reduction with varying source-sensor separation distance. Figure 9.7(a) presents the mode amplitudes at the error sensors after control and shows that at 885Hz the level of $m = 0$ modes dominate the sound field at the error sensors. The levels of these modes therefore determine the sound pressure, and therefore, the sound power after control. This suggests that, with only propagating modes determining the sound power after control, control performance should not be significantly affected by increasing the distance between the source and sensor array. This situation contrasts that in chapter 5 when extraneous modes were ignored and the power reduction

was shown to be fundamentally limited by the level of the cut-off radial mode associated with $m = m_B$.

9.9.1 Control mechanism at $885Hz$

In order to gain insight into the effect on control performance of increasing the source-sensor separation distance Δx, the sound pressure level was measured before and after control along the full length of the duct, in 5cm increments. These measurements were repeated with the error microphones positioned at the four sensor measurement locations: $x = 1.4m, 1.55m, 1.7m$ and $1.85m$. The measured reduction in sound pressure level along the duct wall was compared with predictions obtained from the model. The measured and predicted sound pressure level reductions are compared in figures 9.16(a) to 9.16(d) for the four error sensor positions listed above.

Excellent qualitative agreement is generally observed between the measured and predicted sound pressure reductions. Particularly good agreement is obtained with the error sensors at $x_e = 1.55m$ in figure 9.16(b). The characteristic 'decay' close to the secondary source array is clearly observed. The pressure is driven to a minimum at the error sensor array which then settles to a reduction in level of approximately 20dB between the error sensor array and the duct termination. Comparing this with the predicted reduction observed in figure 9.16(a), reveals an improvement of 10dB over the control system with the error sensors at $x_e = 1.4m$. This seems to suggests that control performance may be improved by moderate levels by increasing the source-sensor separation distance, with the best control performance being obtained with the error sensors positioned at $x_e = 1.85m$.

The agreement between measured and predicted sound pressure level reduction is poorest with $x_e = 1.7$ in figure 9.16(c). This is likely to be due to poor reduction in pressure at the error sensors caused by inaccuracies in the transfer function estimates at this sensor position. The predicted sound pressure reduction suggests that the control performance has improved since the pressure reduction predicted at the 'inlet' termination is lower than with the sensors positioned at $x_e = 1.55m$. However, the measured pressure reduction at

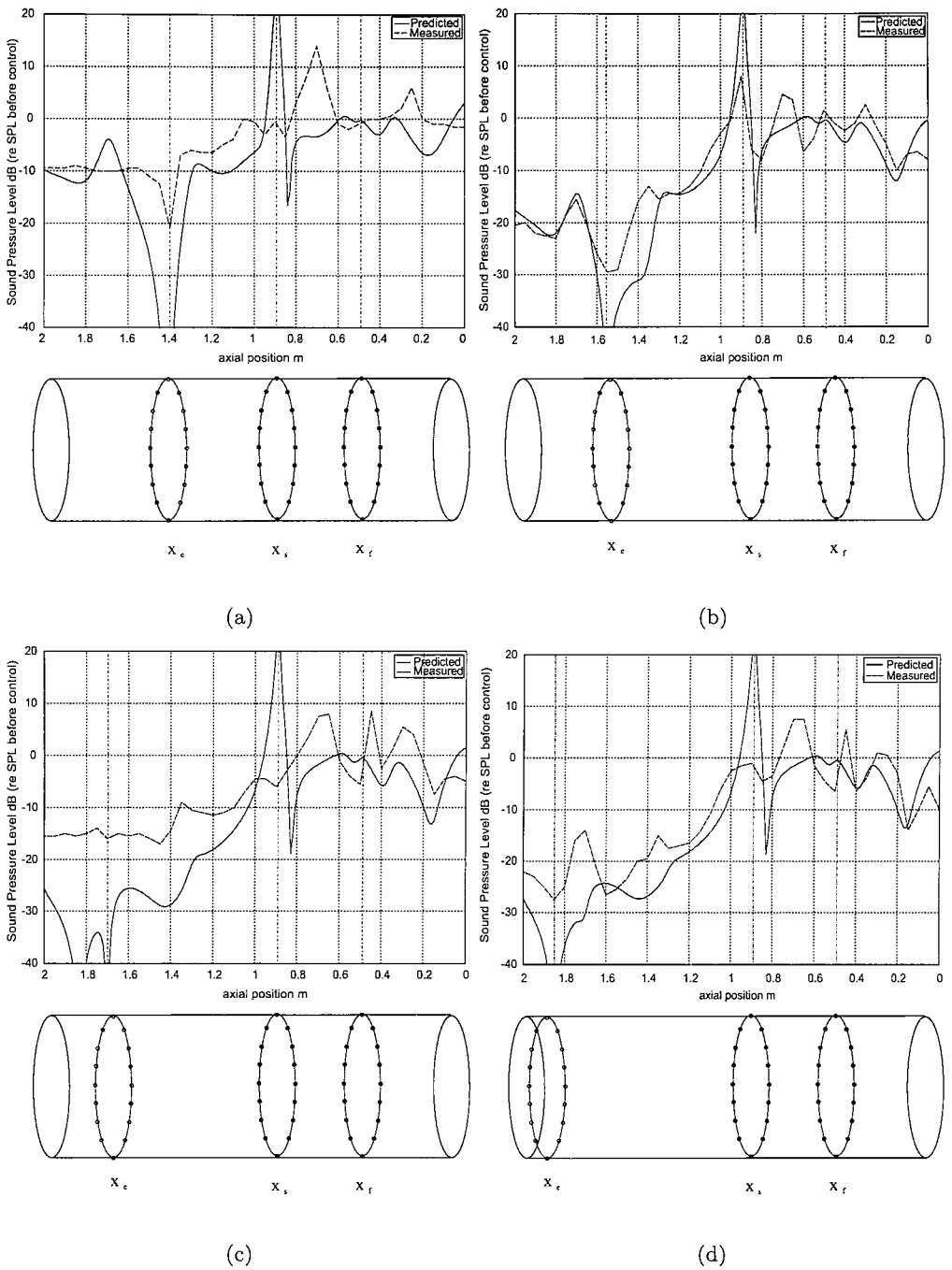

Figure 9.16: *Sound Pressure Reduction with varying axial position 885Hz* $x_e = 1.4m$ *(a), 1.55m (b), 1.7m (c) and 1.85 (d)*

the termination which controls the sound power reduction is greatest in figure 9.16(d) corresponding to the largerst source-sensor separation distance.

Figures 9.17(a) to 9.17(d) present the predicted mode amplitudes after control for the four cases above. They demonstrate that as the sensors and sources are moved further apart, the axisymmetric modes excited by the secondary sources steadily reduces, which as we have shown, ultimately determines the level of sound power reduction in this experimental rig.

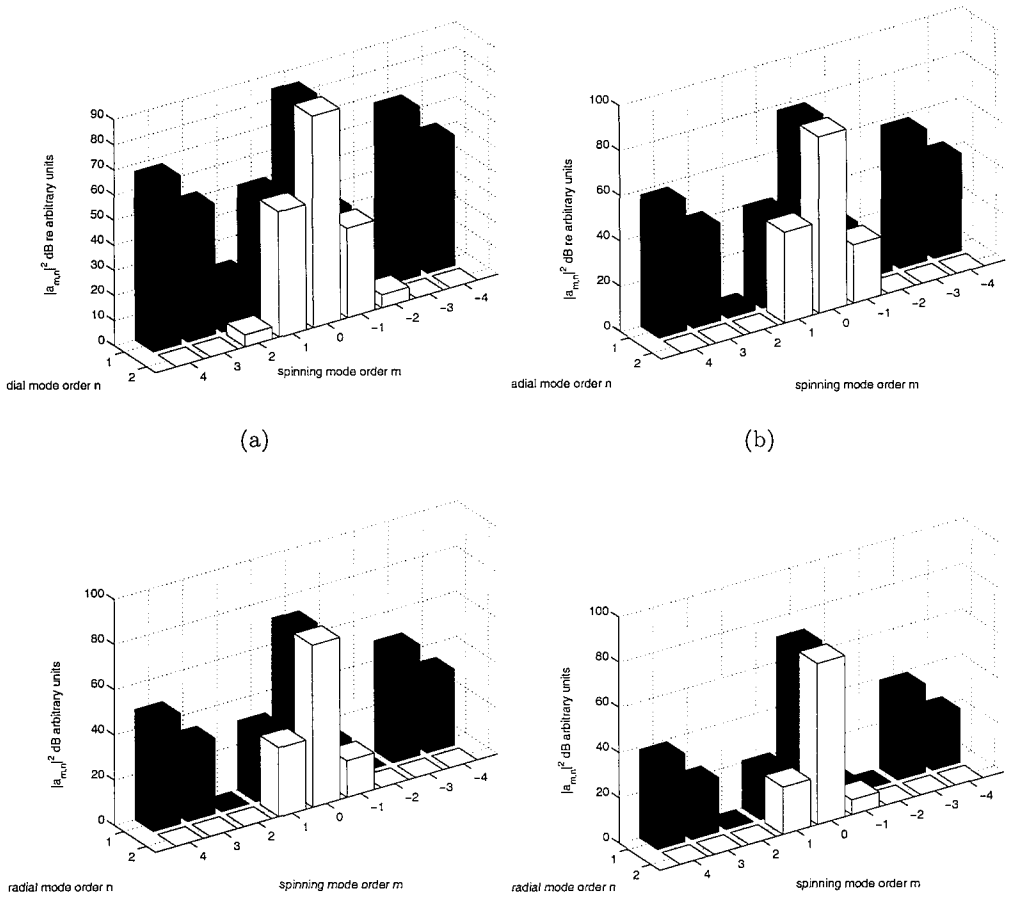

Figure 9.17: *Individual mode amplitudes after control at the error sensor array at 885Hz* x_e *= 1.4m (a), 1.55m (b), 1.7m (c) and 1.85m (d)*

In an attempt to explain this Δx-dependence, a simple analytical model is now developed

for the sound power reduction versus Δx for the case of our experimental rig.

9.9.2 Analytic model for the sound power after control at 885Hz

In this section a simple analytical model is presented for the sound power reduction versus source-sensor separation distance Δx at frequencies sufficiently below $f_{4,1}$ that the contribution to the pressure at the error sensors from the (4,1) mode may be neglected.

Chapter 5 has shown that the spinning mode amplitudes at the duct wall can be driven to zero when sufficient numbers of sources and sensors are used (i.e. no aliased modes) and the pressure is driven to zero at the error sensors. As discussed earlier, only the $m = 0$ mode comprises two radial modes with all other modes comprising only one. These two modes cannot be individually cancelled, but only their sums. We can therefore write,

$$\hat{a}_0(x_e) = a_{0,1}(x_e) + a_{0,2}(x_e) = 0 \tag{9.6}$$

where

$$\begin{aligned} a_{0,1}(x_e) &= a_{p_{0,1}}(x_e) + Q_0 z_{0,1}(x_s, x_e) \\ a_{0,2}(x_e) &= a_{p_{0,2}}(x_e) + Q_0 z_{0,2}(x_s, x_e) \end{aligned} \tag{9.7}$$

Q_0 being the modal source strength defined in chapter 5 and $z_{0,1}$ and $z_{0,2}$ being the modal transfer impedances between the source ring and the amplitudes of the axi-symmetric radial modes defined in equation 5.25. Substituting equation 9.7 into 9.6 gives

$$\hat{a}_0(x_e) = a_{0,1_p}(x_e) + a_{0,2_p}(x_e) + Q_0 \left[z_{0,1}(x_s, x_e) + z_{0,2}(x_s, x_e) \right] = 0 \tag{9.8}$$

The modal source strength Q_0 is given by the 'DC' component of the secondary source ring (see equation 5.23),

$$Q_0 = \frac{1}{7}\sum_{m=1}^{7} q(\theta_m) \tag{9.9}$$

Equation 9.8 can be used to obtain an expression for the modal source strength Q_0 in terms of the amplitudes of the modes before control, $a_{p_{0,1}}, a_{p_{0,2}}$, and the modal transfer impedances $z_{0,1}$ and $z_{0,2}$,

$$Q_0 = \frac{-a_{p_{0,1}}(x_e) + a_{p_{0,2}}(x_e)}{z_{0,1}(x_s, x_e) + z_{0,2}(x_s, x_e)} \tag{9.10}$$

Note that $z_{0,1}(x_s, x_e) + z_{0,2}(x_s, x_e)$ can be interpreted as the combined modal impedance of the $m = 0$ mode.

Substituting equation 9.10 into equation 9.7 one obtains the following expressions for the radial mode amplitudes at the error sensors after control,

$$a_{0,1}(x_e) = \frac{a_{p_{0,1}}(x_e) z_{0,2}(x_s, x_e) - a_{p_{0,2}}(x_e) z_{0,1}(x_s, x_e)}{z_{0,1}(x_s, x_e) + z_{0,2}(x_s, x_e)} \tag{9.11}$$

and

$$a_{0,2}(x_e) = \frac{a_{p_{0,2}}(x_e) z_{0,1}(x_s, x_e) - a_{p_{0,1}}(x_e) z_{0,2}(x_s, x_e)}{z_{0,1}(x_s, x_e) + z_{0,2}(x_s, x_e)} \tag{9.12}$$

Assuming that the sound power from all other modes can be neglected, the sound power can be determined from

$$W(x_e) = |a_{0,1}(x_e)|^2 \gamma_{0,1}(x_e) + |a_{0,2}(x_e)|^2 \gamma_{0,2}(x_e) \tag{9.13}$$

From equation 9.6, $|a_{0,1}| = |a_{0,2}|$ and thus the power after control can be simply expressed as

$$W(x_e) = \left| \frac{a_{p_{0,1}}(x_e) z_{0,2}(x_s, x_e) - a_{p_{0,2}}(x_e) z_{0,1}(x_s, x_e)}{z_{0,1}(x_s, x_e) + z_{0,2}(x_s, x_e)} \right|^2 (\gamma_{0,1}(x_e) + \gamma_{0,2}(x_e)) \tag{9.14}$$

Equation 9.14 can be used to obtain a simple expression for the variation of sound power reduction with sensor position.

In the absence of reflections and mean flow, the modal transfer impedance of equation 4.2 can be written as

$$z_{m,n}(x_s, x_e) = \frac{\rho c}{2 S \alpha_{m,n}} e^{i k_{x_{m,n}} (x_e - x_s)} \tag{9.15}$$

and the power factors of equation 9.14, $\gamma_{0,1}$ and $\gamma_{0,2}$, are equal to $\frac{S}{2\rho c}$ and $\frac{S\alpha_{0,2}}{2\rho c}$ respectively. Substituting these results into equation 9.14 and for simplicity assuming that $|a_{p_{0,1}}|^2 = |a_{p_{0,2}}|^2$ we obtain a simple expression for the sound power in the form

$$\frac{W}{W_p} = \frac{1 + |\alpha_{0,2}|^2 - 2\alpha_{0,2} \cos((\Delta k_x)(x_f - x_s))}{1 + |\alpha_{0,2}|^2 - 2\alpha_{0,2} \cos(\Delta k_x \Delta x)} \tag{9.16}$$

where $\Delta k_x = k_{x_{0,1}} - k_{x_{0,2}}$ and $\Delta x = x_e - x_s$ and W_p is the sound power before control given by

$$W_p = \frac{|a_{p_{0,1}}|^2 S}{2\rho c} \left[1 + |\alpha_{0,2}|^2\right] \tag{9.17}$$

Three predictions for the sound power after control versus Δx for the experimental rig at 885Hz are plotted in figure 9.18. The three curves show the prediction obtained using the full model of chapter 3, the analytical model given by equation 9.14 and the simplified model of equation 9.16 using the exact expression for the modal impedances. Excellent agreement is obtained between the analytical model and the full prediction for $\Delta x > 0.2m$.

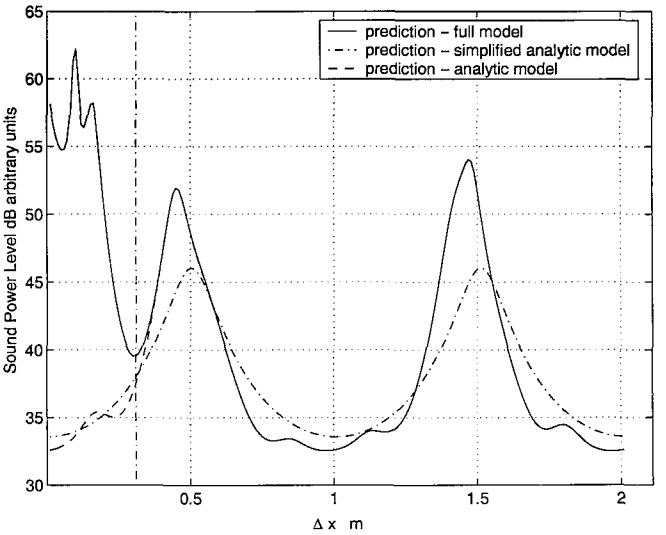

Figure 9.18: *The predicted sound power level after control at 885Hz with varying sensor position*

The general behaviour is also closely predicted by using the simple expression of equation 9.16 which assumes no reflections.

The maxima in this figure, corresponding to separation distances $\Delta x_n = 0.45m$ and $1.47m$ of smallest power reduction, occur where $\Delta k_x \Delta x_n = n\pi$. These positions correspond to source/sensor separation distances at which the combined impedance, $z_{0,1}(x_s, x_e) + z_{0,2}(x_s, x_e)$, is a minimum and hence the secondary source ring is least well coupled to the error sensors. At these separation distances the modes cannot be driven to be in anti-phase without being excited to a high level. Equation 9.16 predicts that the maxima in this figure increase as the frequency increases above the cut-off frequency of the $(0, 2)$ mode as $\alpha_{0,2}$ approaches unity.

Poor agreement for $\Delta x < 0.2m$ is due to the presence of the evanescent $m = \pm 4$ modes, which dominate the sound field at these close separation distances, and which are not included in the simple model. At higher frequencies this mode will decay more slowly and so may affect control performance. The control mechanism at higher frequencies will be discussed in section 9.9.3.

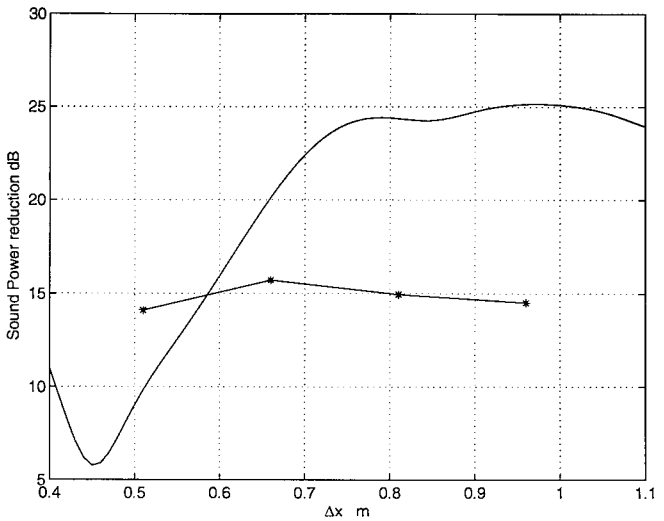

Figure 9.19: *Comparison between measured and predicted variation of sound power reduction with source/sensor separation distance at 885Hz*

Figure 9.19 shows a comparison between the measured sound power reduction for the four error sensor positions, and the predicted reduction obtained using the full numerical model. The prediction is seen to overestimate the measured power reduction by approximately 10dB. The main reason for this difference therefore, is that the prediction assumes zero pressure at the errors sensors whereas the pressure is only reduced by approximately 20-30dB in the experiment. A high level of cancellation between the two radial modes is necessary to achieve the high sound power level reduction predicted in figure 9.19.

9.9.3 Control mechanism at $f \geq 900Hz$

In this section we investigate the mechanism of control at frequencies greater than 900Hz. The important difference here compared with the results presented in section 9.9.1 is that the $m = \pm 4$ modes are significantly less cut-off, and hence make a significant contribution to the pressure at the error sensors.

Figures 9.20(a) to 9.20(d) show the predicted mode amplitudes after control for the four sensor positions. At this higher frequency the evanescent $m = \pm 4$ modes are observed to

have a higher amplitude than the axi-symmetric modes at the error sensor array. There are insufficient sources and sensors to detect and control this mode without affecting lower order modes. As discussed in section 9.5 The control system therefore excites the modes such that $\hat{a}_{\pm 3} + \hat{a}_{\mp 4} = 0$.

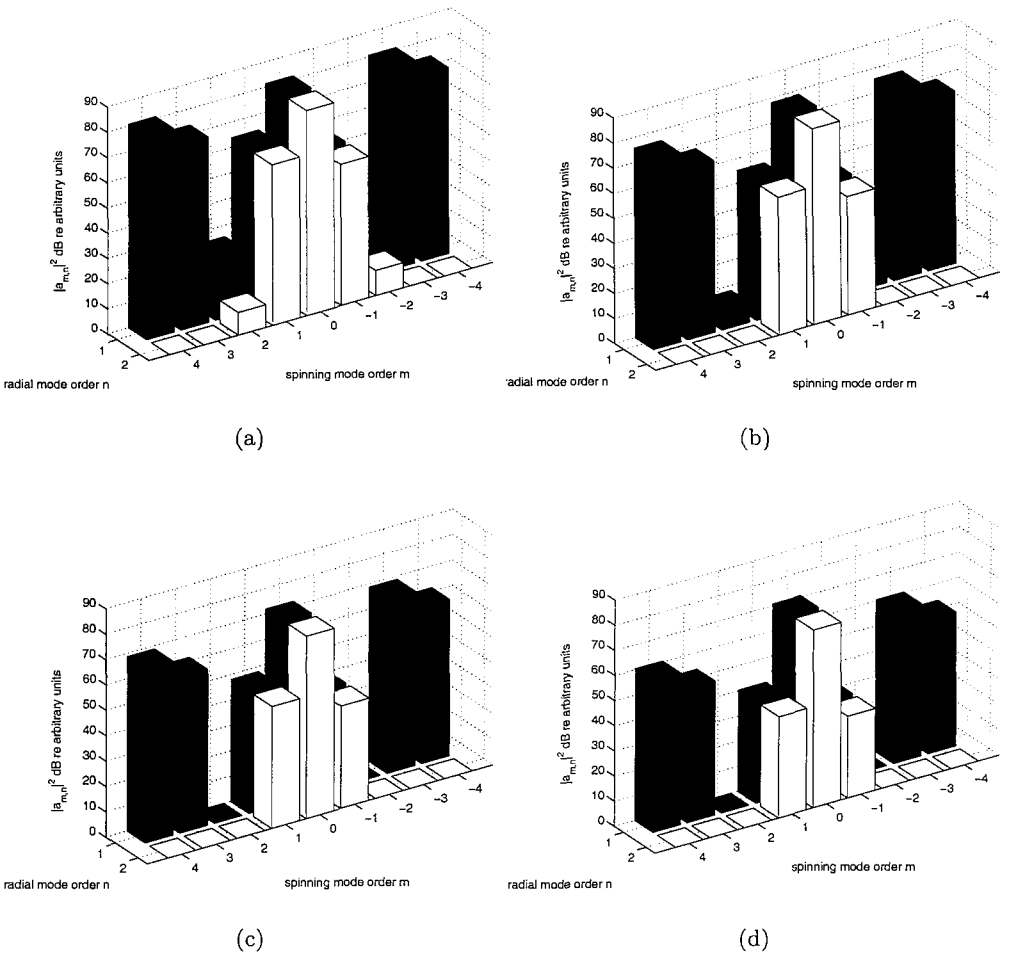

Figure 9.20: *Predicted mode amplitudes after control at the error sensor array at 920Hz $x_e = 1.4m$ (a), 1.55m (b), 1.7m (c) and 1.85m (d)*

With the error sensor array positioned at $x_e = 1.4m$, figure 9.20(a) shows that the level of the $m = \pm 4$ modes is larger than that of the $m = 0$ mode. The $m = \pm 3$ modes will therefore be excited in order to cancel with this mode, and will therefore dominate the sound power after control. Global control performance is therefore degraded. The level of the evanescent mode reduces as the source-sensor separation distance is increased.

With the error sensors positioned furthest from the source array at $x_e = 1.85m$ the evanescent mode has decayed to a level lower than that of the axi-symmetric mode. The $m = \pm 4$ modes will therefore no longer affect control performance at these high separation distances. The decay in SPL between sources and sensors of the evanescent mode can be determined from

$$\Delta SPL = -8.7\frac{2\pi}{c}\Delta x\sqrt{f_{4,1}^2 - f^2} \qquad (f < f_{4,1}) \tag{9.18}$$

At 920Hz, with the error sensors positioned at $x_e = 1.4$ the $m = \pm 4$ mode will decay by 24dB before reaching the error sensor array. The decay is increased to 32dB at the lower frequency of 885Hz.

Figures 9.21(a) to 9.21(d) show a comparison between the measured and predicted sound pressure reduction along the length of the duct for the four error sensor positions at this higher frequency of 920Hz. At each error sensor position, the decay of the evanescent mode between the secondary source array and the error sensors can be observed in all cases. Agreement between the measured and predicted pressure reduction levels are not as good as at 885Hz in figure 9.16, however, the qualitative agreement remains good, with many of the features being closely predicted. Once again, the likely reason for the difference between prediction and measurement is that the model assumes zero pressure at the error sensors whilst in practice reduction are limited to about 20dB. It follows, therefore, that in order to reduce the effect of the evanescent mode on control performance, the distance between the secondary source and sensor array should be increased.

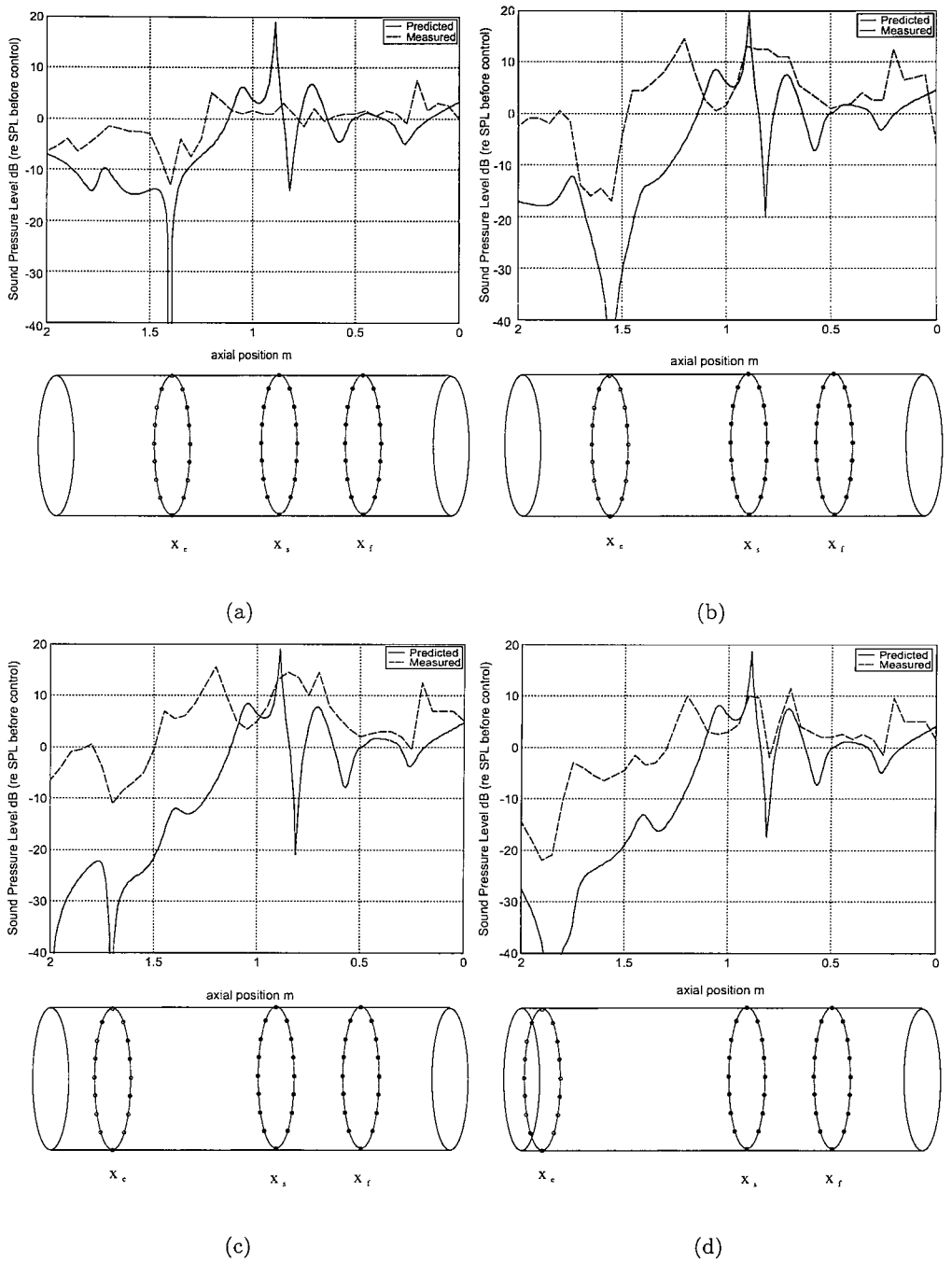

Figure 9.21: *Sound Pressure Reduction with varying axial position 920Hz $x_e = 1.4m$ (a), 1.55m (b), 1.7m (c) and 1.85 (d)*

Figure 9.22 shows a comparison between the predicted variation in sound power reduction with varying separation distance using the theoretical model and the measured sound power reduction. In both prediction and measurement, increasing the separation distance between the sources and sensors is observed to increase the sound power reduction. Whilst the prediction and measurement follow the same trend, the latter is roughly 5dB less than that predicted. Again, this is due to imperfect cancellation of the pressure at the error sensors.

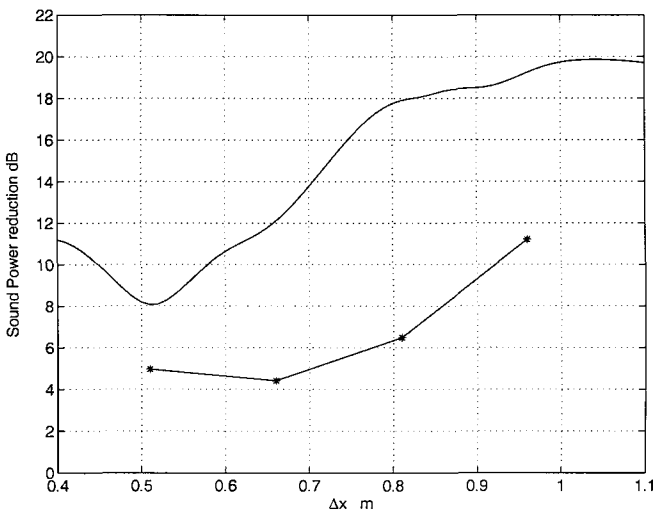

Figure 9.22: *Variation of sound power reduction with source/sensor separation distance*

In order to illustrate the effect of increasing source-sensor separation on control performance over the entire frequency range, figure 9.23 shows the measured sound power reduction at all frequencies with the error sensors positioned at $x_e = 1.4$ (dashed line) and at $x_e = 1.85$ (dash/dot line). With the error sensors positioned at $x_e = 1.85$ a measurement could not be obtained at 765Hz due to noisy transfer function measurements causing the control system to become unstable. This is likely to be because at this frequency there is a null in the primary field pressure close to $x_e = 1.85m$. Also plotted are the predicted sound power reductions, assuming that the primary source axi-symmetric mode amplitudes are equal.

Comparing the predicted sound power reductions, at the lowest frequencies, there is little improvement in the sound power reduction. At frequencies above 850Hz, the sound power

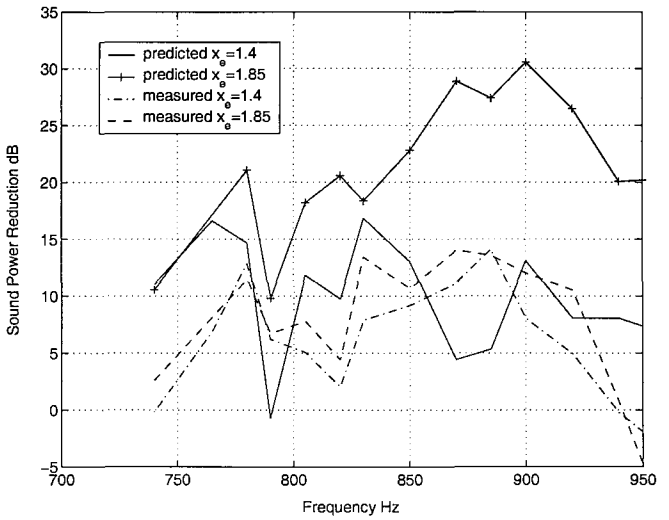

Figure 9.23: *Measured and Predicted sound power reduction with the error sensors positioned at* $x_e = 1.4m$ *and* $x_e = 1.85m$

reduction improves by up to 25dB at some frequencies. In the prediction where the pressure is driven to zero, we have seen that at the lower frequencies, the sound power reduction is dependent on the coupling between the sensors and the axi-symmetric $m = 0$ modes. It is difficult therefore to distinguish between the frequencies at which the sound power reduction is dominated by the axi-symmetric modes and those at which the sound power reduction is affected by the $(4, 1)$ evanescent mode.

In the measured frequency dependence, there is little difference between the sound power reductions below 885Hz, as we have seen in figure 9.4 that in the actual system the axi-symmetric modes only partially cancel. However, at 900Hz and 920Hz, where it is expected that the $m = \pm 4$ modes will affect the sound power reduction. An increase in sound power reduction of 5dB is observed at the frequency of 920Hz.

9.10 Conclusions

- A single frequency control system to control the $(-3, 1)$ mode has been implemented. It has been shown that by minimising the sum of the squared pressures at the error sensor array one can achieve reductions of up to 14dB in the sound power radiated

from the duct.

- The model developed in chapter 3 was shown to give qualitatively good agreement with the measured pressure variation along the duct both before and after control. Predictions of sound power reductions were generally overestimated. This is likely to be because in the model the pressure is driven to zero, whereas in reality the pressure is only reduced by between 10 and 30dB.

- Using the theoretical model, the sound power after control at the lower frequencies was seen to be dominated by the level of the axi-symmetric modes after control. An analytical model was developed to predict the sound power reduction. Poor agreement was seen with measurements, however results do indicate that this control mechanism exists.

- At frequencies close to the cut-on frequency of the $(4,1)$ mode, aliasing of this evanescent mode occurs which degrades control performance. This mode will dominate the control mechanism at these higher frequencies. It was shown that as the separation distance is increased, control performance increases the most at higher frequencies.

Chapter 10

Conclusions and Further Work

10.1 Conclusions

In this chapter we shall summarise the conclusions drawn from previous chapters and suggest possibilities for further study.

Chapter 1 demonstrated that although a great deal of research has been undertaken into the active control of aircraft engine noise, it has predominantly focussed on the attenuation of rotor-stator interaction noise. There has been no publication of research into the application of active control to control buzz-saw noise, which is much simpler in modal composition and lower in frequency.

The modal structure of buzz-saw noise was described in chapter 2. The passive liner sections currently used in aircraft engine nacelles to attenuate noise have insufficient thickness to effectively attenuate its very low frequency components. At the tip speeds associated with take-off, the low EO buzz-saw tones which dominate the sound field have a very simple modal structure. At each 'engine order' (EO), the sound field is dominated by a single mode with azimuthal mode order $m = m_B = EO$. At the frequencies associated with these low engine orders, only a single radial mode can propagate in the engine inlet. Thus, at each frequency only a single mode must be controlled.

A model for the propagation of buzz-saw noise in a finite-length duct is developed in chapter 3. The model uses a simple method for the estimation of modal reflection. It is based on a modification of Zorumski's [63] generalised impedance method to account for mean flow effects. It was shown that these modal reflection coefficients are consistent with energy conservation when the definition of energy in flow by Morfey [43] is used.

The two active control objectives to be studied in chapter 5 and 7 are described in chapter 4. These include a pressure control objective whereby the sum of the squared pressures are minimised at the error sensor array, and a pragmatic modal control algorithm whereby the sum of the square spinning mode amplitudes measured at the duct walls are minimised. It was shown in this chapter that the transfer impedance matrix which relates the pressure at the error sensors to the source strengths may become badly conditioned depending on the number of sources and sensors in the control system. A badly conditioned control system is one in which the presence of a small amount of noise at the error sensors causes comparatively large increases in the source strengths required for control. The source strengths can be limited by introducing a regularisation parameter into the cost function. This is achieved at the expense of a smaller reduction in the cost function. The use of Hansen's L-curve [23] technique is applied to identify the optimal regularisation parameter which simultaneously gives the largest reduction in pressure using the smallest value for the source strengths.

In chapter 5 the theoretical model developed in chapter 3 was used to predict the sound power reduction achieved by minimising the sum of the squared pressures at the error sensor array. Noise and extraneous modes were assumed to be absent. This control objective was studied due to its simplicity and relative ease of implementation. The primary sound field in this case is assumed to comprise a single buzz-saw mode ($m = EO, n = 1$). It was shown that sound power reductions could be achieved provided that the number of sources and sensors satisfies the Nyquist sampling criterion, whereby the number of sources and sensors must exceed $2|m_{max}|+1$ where m_{max} is the highest spinning mode order which can propagate in the duct. A more practical sampling criterion of $2|m_{max}|+3$ was suggested to avoid aliasing problems and hence modal spillover. Aliasing is due to higher order azimuthal mode orders which are close to cut-on and therefore have

a significant amplitude at the sensor array.

In the absence of noise, the sound power reduction achievable was found to be fundamentally limited by the level at the error sensors of the $(m = EO, n = 2)$ evanescent mode excited by the secondary sources. This finding was used to develop an analytical model for the sound power reduction after control which is in close agreement with the exact calculation. Strong reflections associated with modes close to cut-off are shown to influence control performance. A modal interpretation of the control mechanism is described. It has been shown that after control there are two standing wave regions in the duct. High amplitude standing waves are present between the secondary sources and the 'exhaust' termination, and a weaker set of standing waves are observed between the sensor array and 'inlet' whose amplitude is determined by the presence of the evanescent $(m_B, 2)$ mode.

Substantially greater control performance has been shown to be possible by the use of an additional ring of sources and sensors. The two-ring system is able to independently control two radial mode orders, thus it can attenuate the second evanescent radial and control will be significatly improved.

The effect on control performance of two types of noise are examined in chapter 6. The control mechanism is examined with respect to the spatial DFT relationship between the pressure at the error sensors and the spinning mode amplitudes at the duct wall proposed in chapter 5. It has been shown that when 'extraneous' modes are present in the primary field, and as long as the Nyquist criterion is satisfied, the pressure can be driven to zero which results in the spinning mode amplitudes being driven to zero. The single-ring control system ensures that the spinning mode amplitudes are driven to zero by arranging that the amplitudes of higher order radial modes are excited such that they destructively interfere. The spinning modes with higher order radial modes are therefore not individually driven to zero and will therefore dominate the sound power after control.

When 'local' noise is present at the error sensor array, the control system 'observes' a broad modal spectrum and thus aliasing of the higher spinning mode orders, and hence spillover will occur. In the presence of noise, the pressure at the error sensors (and hence the spinning modes) are not driven to zero, causing a deterioration in control performance.

The degradation of sound power reduction is not as great as when extraneous modes with the same level are present. It was also shown in chapter 4 that when the number of sources is larger than the number of spinning mode orders the condition number of the transfer impedance matrix $\mathbf{Z}$ is large, resulting in large source strengths being required to cancel the pressure. The source strengths can however be limited by applying a regularisation parameter β to the $\mathbf{Z}$ matrix. In practice this is equivalent to introducing a leakage term in the FXLMS algorithm.

Chapter 7 concerns an investigation into control performance when minimising the sum of the square spinning mode amplitudes at the duct wall. The control performance was found to be identical to that predicted when minimising the sum of the squared pressures. However, weighting the cost function such that control focusses only on the buzz-saw mode was found to yield significant improvements in control performance with noise at the error sensors.

The design and implementation of an active control system to control a low order spinning mode in a no-flow duct was described in chapters 8 and 9. An $m = -3$ mode was generated using a mode synthesiser ring and this spinning mode was controlled using seven sources and seven error sensors. Sound power reductions of up to 14.5dB were measured at the duct face when minimising the sum of the squared pressures at the error sensors using a single frequency FXLMS algorithm. The control mechanism was examined using the theoretical model developed in chapter 3. It was seen that the level of the axi-symmetric $m = 0$ modes dominate the sound power after control, and hence sound power reduction was found to be significantly less than the pressure reduction at the error sensors. However, it was also found that, because the number of sensors was equal to $2|m_{max}| + 1$ in the experiment, aliasing of the evanescent $m = \pm 4$ modes also causes degradation in control performance at the higher frequencies in which these cut-off modes contribute significantly to the pressure at the error sensors.

10.2 Suggestions for further work

Experimental results verify that sound power reduction can be achieved by minimising the sum of the squared pressure at the error sensors. Suggestions for further work include making modifications to the experimental rig in order to further verify the theoretical results.

- The active control could be repeated in a fan-rig facility with the fan as the sound source. The measurement of the transfer functions in the no-flow duct was a simple procedure, however, in the presence of flow it may be more difficult to gain an accurate plant model and hence control performance may be degraded.
- Due to cost and time factors the number of sources and sensors were chosen to be equal to $2|m_{max}| + 1$ in the experiment. More sources and sensors could be used to eliminate the problems caused by the aliasing of cut-off modes. The use of an overdetermined system where there are more sensors than sources could also be investigated.
- Control has been implemented at a single frequency and applied to a single spinning mode. Further research is required to identify any problems associated with the simultaneous control of multiple tones.
- Finally, more research is needed into the use of practical modal algorithms to control the sound field. In order to focus control on the buzz-saw mode, one would need to design a controller which could identify in real-time the dominant mode and synthesise the same mode using the secondary source array. The error could then be minimised using a conventional FXLMS algorithm.

The theoretical and experimental results presented in this thesis suggest that active control is a feasible approach to attenuate the low frequency components of buzz-saw noise. Provided the actuators used are able to produce sufficiently high levels linearly and that the transfer functions can be accurately measured in a real engine inlet in the presence of flow, it is likely that active noise control will afford substantial noise control benefits.

Appendix A

Derivation of the primary pressure expression

Equation 3.6 gives the acoustic pressure at the error sensors $p(x, r, \theta)$ in terms of the reflection coefficients at the duct terminations $R^{\pm}$,

$$p_{m,n}(x, r, \theta) = \frac{a_{p_0}[e^{ik^+_{x_{m,n}}(x-x_f)} + R^+_{m,n}e^{i(k^+_{x_{m,n}}-k^-_{x_{m,n}})L - ik^+_{x-m,n}x_f + ik^-_{x_{m,n}}x}]\psi(r,\theta)}{1 - R^+_{m,n}R^-_{m,n}e^{i(k^+_{x_{m,n}}-k^-_{x_{m,n}})L}} \quad , \quad \text{(A.1)}$$

where the reflection coefficients are defined in terms of the complex reflectivity coefficients $\phi^{\pm}_{m,n}(x)$

$$R^+_{m,n} = e^{2i\phi^+(L)} = e^{2i\left(\phi^+_0 - \frac{\alpha_{m,n}kL}{1-M_x^2}\right)} \quad \text{(A.2)}$$

$$R^-_{m,n} = e^{-2i\phi^-(0)} = e^{-2i(\phi^-_0)} \quad \text{(A.3)}$$

In these equations, the complex reflectivity factors $\phi^{\pm}_{m,n}(x)$ can be defined as below in equations 3.9 and 3.10,

$$\phi^{+}_{m,n}(x) = \frac{\ln R^{+}_{m,n}(L)}{2i} + \frac{\alpha_{mn} k(L-x)}{1-M_x^2} \tag{A.4}$$

$$\phi^{-}_{m,n}(x) = \frac{-\ln R^{-}_{m,n}(0)}{2i} + \frac{\alpha_{mn} k(-x)}{1-M_x^2} \tag{A.5}$$

Substituting A.2 and A.3 into equation A.1 and noting that the axial wavenumber $k^{\pm}_{x_{m,n}}$ is defined

$$k^{\pm}_{x_{m,n}} = \left(\frac{\pm\alpha_{m,n} - M_x}{1-M_x^2} \right) k \tag{A.6}$$

one obtains the expression

$$\begin{aligned} p_{m,n}(x,r,\theta) \;=\; & a_{p_0} \left[e^{\frac{i\alpha_{m,n}k(x-x_s)}{1-M_x^2} - \frac{iM_x k(x-x_s)}{1-M_x^2}} \right. \\ & \left. + e^{2i\phi_0^{+} - \frac{2i\alpha_{m,n}kL}{1-M_x^2} + \frac{2i\alpha_{m,n}kL}{1-M_x^2} - \frac{i\alpha_{m,n}k(x+x_f)}{1-M_x^2} - \frac{iM_x k(x-x_f)}{1-M_x^2}} \right] \\ & \times \frac{\psi_{m,n}(r,\theta)}{1-e^{2i(\phi_0^{+}-\phi_0^{-})}} \end{aligned} \tag{A.7}$$

which reduces to

$$p_{m,n}(x,r,\theta) = \frac{a_{p_0} e^{\frac{-iM_x k(x-x_s)}{1-M_x^2}} \left[e^{\frac{i\alpha_{m,n}k(x-x_f)}{1-M_x^2}} + e^{2i\phi_0^{+} - \frac{i\alpha_{m,n}k(x+x_f)}{1-M_x^2}} \right] \psi_{m,n}(r,\theta)}{1-e^{2i(\phi_0^{+}-\phi_0^{-})}} \tag{A.8}$$

Multiplying the numerator and denominator of the right hand side of this equation by $e^{i(\phi_0^{-}-\phi_0^{+})}$ one obtains

$$p_{m,n}(x,r,\theta) = \frac{a_{p_0} e^{\frac{-iM_x k(x-x_f)}{1-M_x^2}} \left[e^{i\left(\phi_0^- - \phi_0^+ + \frac{\alpha_{m,n} k(x-x_f)}{1-M_x^2}\right)} + e^{i\left(\phi_0^+ + \phi_0^- - \frac{i\alpha_{m,n} k(x+x_f)}{1-M_x^2}\right)} \right] \psi_{m,n}(r,\theta)}{e^{i(\phi_0^- - \phi_0^+)} - e^{-i(\phi_0^- - \phi_0^+)}} \tag{A.9}$$

Noting that

$$\phi^-(x_f) = \phi_0^- - \frac{\alpha_{m,n} k(x_f)}{1-M_x^2} \tag{A.10}$$

and

$$\phi^+(x) = \phi_0^+ - \frac{\alpha_{m,n} k(x)}{1-M_x^2} \tag{A.11}$$

equation A.9 can be written

$$p_{m,n}(x,r,\theta) = \frac{a_{p_0} e^{\frac{-iM_x k(x-x_f)}{1-M_x^2}} \left[e^{i(\phi_{m,n}^-(x_f) - \phi_{m,n}^+(x))} + e^{-i(\phi_{m,n}^-(x_f) - \phi_{m,n}^+(x))} \right] \psi_{m,n}(r,\theta)}{e^{i(\phi_0^- - \phi_0^+)} - e^{-i(\phi_0^- - \phi_0^+)}} \tag{A.12}$$

and using Euler's formula equation A.12 can be written in terms of sine and cosine terms

$$p_{m,n}(x,r,\theta) = \frac{a_{p_0} e^{\frac{-iM_x k(x-x_f)}{1-M_x^2}} e^{i\phi_{m,n}^-(x_f)} \cos\phi_{m,n}^+(x) \psi_{m,n}(r,\theta)}{i \sin(\phi_0^- - \phi_0^+)} \tag{A.13}$$

If we now use the indentity $(\phi_{m,n}^-(x_f) - \phi_{m,n}^+(x_f)) = (\phi_0^- - \phi_0^+)$ we can begin to rearrange the denominator such that it is in the same form as Morfey's expression [43]:

$$p_{m,n}(x,r,\theta) = \frac{a_{p_0} e^{\frac{-iM_x k(x-x_f)}{1-M_x^2}} e^{i\phi_{m,n}^-(x_f)} \cos\phi_{m,n}^+(x) \psi_{m,n}(r,\theta)}{i(\sin\phi_{m,n}^-(x_f)\cos\phi_{m,n}^+(x_f) - \cos\phi_{m,n}^-(x_f)\sin\phi_{m,n}^+(x_f))} \quad ; \tag{A.14}$$

taking $\cos\phi^{+}_{m,n}(x_f)$ outside the brackets in the denominator

$$p_{m,n}(x,r,\theta) = \frac{ia_{p_0}e^{\frac{-iM_x k(x-x_f)}{1-M_x^2}}e^{i\phi^{-}_{m,n}(x_f)}\cos\phi^{+}_{m,n}(x)\psi_{m,n}(r,\theta)}{\left(\frac{\cos\phi^{-}_{m,n}(x_f)\sin\phi^{+}_{m,n}(x_f)}{\cos\phi^{+}_{m,n}(x_f)} - \sin\phi^{-}_{m,n}(x_f)\right)\cos\phi^{+}_{m,n}(x_f)} \tag{A.15}$$

and dividing top and bottom by $\cos\phi^{-}_{m,n}(x_f)$ gives the final expression

$$p_{m,n}(x,r,\theta) = \frac{a_{p_0}\psi_{m,n}(r,\theta)ie^{i\phi^{-}_{m,n}(x_f)}\sec\phi^{-}_{m,n}(x_f)}{\left(\tan\phi^{+}_{m,n}(x_s) - \tan\phi^{-}_{m,n}(x_f)\right)}\frac{\cos\phi^{+}_{m,n}(x)}{\cos\phi^{+}_{m,n}(x_f)}e^{\frac{-iM_x k\left(x-x_f\right)}{1-M_x^2}} \tag{A.16}$$

Appendix B

Obtaining complex signals from microphone measurements

The voltage signal measured at the microphone $v(t)$ can be represented as a Fourier series.

$$v(t) = \sum_{\mathrm{n}=0}^{\mathrm{n}T} A_n \cos(2\pi f \mathrm{n}T + \phi_{\mathrm{n}}) \tag{B.1}$$

$$= \sum_{\mathrm{n}=0}^{\mathrm{n}T} A_n \left(a_n \cos \omega \mathrm{n}T + b_n \sin \omega \mathrm{n}T\right) \tag{B.2}$$

where f is the frequency in Hertz, n is the sample number and T is the sampling period $1/f_s$. Expanding equation B.1

$$v(t) = \sum_{\mathrm{n}=0}^{t} A_n \left(\cos \omega \mathrm{n}T \cos \phi_n - \sin \omega \mathrm{n}T \sin \phi_n\right) \tag{B.3}$$

Therefore the coefficients a_n and b_n are defined

$$a_n = A_n \cos \phi \tag{B.4}$$

$$b_n = -A_n \sin\phi \tag{B.5}$$

and thus the magnitude A_n and the phase ϕ_n of the signal can be determined

$$A_n = \sqrt{a_n^2 + b_n^2} \tag{B.6}$$

$$\phi = \arctan\left(\frac{-b_n}{a_n}\right) \tag{B.7}$$

The values of the coefficients can be determined from the measured signals by numerically integrating over a number of samples n

$$a_n = \frac{2dt}{\mathrm{n}T} \sum_{0}^{\mathrm{n}T} v(\mathrm{n}) \cos 2\pi f \mathrm{n}T \tag{B.8}$$

$$b_n = \frac{2dt}{\mathrm{n}T} \sum_{0}^{\mathrm{n}T} v(\mathrm{n}) \sin 2\pi f \mathrm{n}T \tag{B.9}$$

References

[1] Anon. Axial-flow fan compressor noise generating mechanisms. *Engineering Sciences Data Unit, Data Items*, (N), 1975. English.

[2] Stephen Barnett. *Matrices - Methods and Applications.* Clarendon Press - Oxford, 1990.

[3] J.P. Battaner-Moro. *A computational method for the determination of the reflection coefficients in circular ducts.* Msc, Southampton, 1999.

[4] Julius S. Bendat and Allan G. Piersol. *Measurement and analysis of random data.* Wiley - New York, 1966.

[5] M. J. Benzakein, S. B. Kazin, S. Savkar, and C. T. Savell. Multiple pure tone noise generation and control. *Prog Astronaut Aeronaut*, 38:57–72, 1973. AIAA Aero-Acoust Spec Conf, Aeroacoust, Fan, STOL, and Boundary Layer Noise, Sonic Boom Oct 1973 Aeroacoust Instrum 8 Refs.

[6] D Berge, E Bouty, and J.M. Cailleau. Active noise control of a jet engine at low frequency radiation : B.e.m. for predicting far-field noise reduction. In *15th Aeroacoustics Conference*, Long Beach, 1993. AIAA.

[7] M. S. Bohn and E. E. Zukoski. Effect of flow on the acoustic reflection coefficient at a duct inlet. *J Acoust Soc Am*, 59(6):1497–1499, 1976.

[8] C.C. Boucher, S.J. Elliott, and P.A. Nelson. Effect of errors in the plant model on the performance of algorithms for adaptive feedforward control. *IEE Proceedings F - Radar and Signal Processing*, 138(4):313–319, 1991.

[9] A. J. Bullmore, P. A. Nelson, and S. J. Elliott. Theoretical studies of the active control of propeller-induced cabin noise. *Journal of Sound and Vibration*, 140(2):191–217, 1990.

[10] R. A. Burdisso, C. R. Fuller, and J.P. Smith. Experiments on the active control of a turbofan inlet noise using compact, lightweight inlet control and error transducers. In *AIAA/CEAS Aeroacoustics Conference*, Munich, 1995. AIAA.

[11] T.M. Chan. *Active Control of Sound in Ducts.* Phd, University of Southampton, 1997.

[12] A. R. D. Curtis, P. A. Nelson, S. J. Elliott, and A. J. Bullmore. The active suppression of acoustic resonances. *Journal of the Acoustical Society of America*, 81:624–631, 1987.

[13] Marvin E.Goldstein. *Aeroacoustics.* McGraw Hill, 1976.

[14] F. F. Ehrich. Acoustic resonance and multiple pure tone noise in turbomachinery inlets. Journal ref: ASME-Paper 69-GT-2, , (1969) Mar 9-13 1969.

[15] S. J. Elliott and L. Billet. Adaptive control of flexural waves propagating in a beam. *Journal of Sound and Vibration*, 163(2):295–310, 1993. Univ of Southampton, Southampton, Engl 0022-460X JA 26 Refs. English.

[16] S. J. Elliott, P. A. Nelson, I. M. Stothers, and C. C. Boucher. In-flight experiments on the active control of propeller-induced cabin noise. *Journal of Sound and Vibration*, 140(2):219–238, 1990.

[17] S.J. Elliott. *Signal Processing for Active Control.* London: Academic Press, 1st edition, 2000.

[18] S.J. Elliott, C.C. Boucher, and P.A. Nelson. The behaviour of a multiple channel active control system. *IEEE transactions on signal processing*, 40(5):1041–1052, 1992.

[19] S.J. Elliott, I.M. Stothers, and P.A. Nelson. A multiple error lms algorithm and its application to the active control of sound and vibration. *IEEE transactions on acoustics, speech and signal processing*, ASSP-35(10):1423–1434, 1987.

[20] Stephen J. Elliott, Christopher C. Boucher, and Philip A. Nelson. The behavior of a multiple channel active control system. *IEEE Transactions on Signal Processing*, 40(5):1041–1052.

[21] E Fruteau, P.F Joseph, and P.A. Nelson. Final report on the reduction of aircraft noise by nacelle treatment and active control (ranntac). Technical Report 00/36, ISVR, December 2000.

[22] Carl H. Gerhold. Active control of fan-generated tone noise. *AIAA Journal*, 35(1):17–22, 1997. NASA Langley Research Cent, Hampton, VA, USA JA 16 Refs. English.

[23] P.C. Hansen. *Rank-Deficient and Discrete Ill-Posed Problems - Numerical Aspects of Linear Inversion.* SIAM, 1998.

[24] D. Hawkings. Multiple tone generation by transonic compressors. *J Sound Vib*, 17(2):241–50, 1971.

[25] D.A.K Hewlett. *The Radiation from Acoustic Sources within a Finite Length Circular Duct Immersed in Water.* Phd, University of Southampton, 1995.

[26] F.V. Hutcheson, C. R. Fuller, and M.H. Dunn. An investigation of active control of ultra high bypass turbofan noise using a boundary integral equation method. In *6th AIAA/CEAS Aeroacoustics Conference*, Lahaina, Hl, 2000.

[27] Uno Ingard and Vijay K. Singhal. Effect of flow on the acoustic resonances of an open-ended duct. *J Acoust Soc Am*, 58(4):788–793, 1975. 17 Refs.

[28] Tatsuya Ishii, Hiroshi Kobayashi, and Hideshi Oinuma. Modal technique for active control of tones radiated from a ducted fan. *Journal of Aircraft*, 35(5):754–760, 1998.

[29] J.M.Tyler and T.G.Sofrin. Axial flow compressor noise studies. *SAE transactions*, 70:309–332.

[30] G. W. Johnston and K. Ogimoto. Sound radiation from a finite length unflanged circular duct with uniform axial flow em dash 1. theoretical analysis. *Journal of the Acoustical Society of America*, 68(6):1858–1870, 1980. 0001-4966 15 Refs.

[31] P.F Joseph, E Fruteau, and P. A. Nelson. Design rules and sensing strategies for the active control of turbofan engine noise. In *7th AIAA/CEAS Aeroacoustics Conference*, Maastricht, 2001.

[32] P.F Joseph, P. A. Nelson, and M. J. Fisher. Active control of turbofan radiation using an in-duct error sensor array. In *Active 97*, Budapest, Hungary, 1997. OPAKFI.

[33] P.F Joseph, P.A. Nelson, and M.J. Fisher. Active control of fan tones radiated from turbofan engines i. external error sensors. *Journal of the Acoustical Society of America*, 106(2):766–778, 1999.

[34] P.F Joseph, P.A. Nelson, and M.J. Fisher. Active control of fan tones radiated from turbofan engines ii. in-duct error sensors. *Journal of the Acoustical Society of America*, 106(2):779–786, 1999.

[35] J.D. Kester. Generation and supression of combination tone noise from turbofan engines. In *AGARD Fluid Dynamics Panel and Propulsion and Energetics Panel*, Saint-Louis, France, 1969. AGARD.

[36] Kenneth A. Kousen and Joseph M. Verdon. Active control of wake blade-row interaction noise. *AIAA Journal*, 32(10):1953–1960, 1994. United Technologies Research Cent, East Hartford, CT, USA 0001-1452 AIAA Washington, DC, USA JA, JA 16 Refs. English.

[37] R.E. Kraft and K.B. Kontos. Theoretical implications of active noise control for turbofan engines. In AIAA, editor, *15th AIAA Aeroacoustics Conference*, Long Beach, 1993. AIAA.

[38] S.M. Kuo and D.R. Morgan. *Active Noise Control Systems:Algorithms and DSP Implementations.* Wiley Series in Telecommunications & Signal Processing. John Wiley & Sons Inc.

[39] M. Kurosaka. Note on multiple pure tone noise. *J Sound Vib*, 19(4):453–462, 1971. 10 Refs.

[40] S. Laugesen. Active control of multi-modal propagation of tonal noise in ducts. *Journal of Sound and Vibration*, 195(1):33–56, 1996.

[41] R Maier, J Zillman, A Roure, M Winninger, L Enghardt, U Tapken, W Neise, H Antoine, and E Bouty. Active control of fan tone noise from aircraft engines. In *7th AIAA/CEAS Aeroacoustics Conference*, Maastricht, 2001.

[42] A. McAlpine and M. J. Fisher. On the prediction of 'buzz-saw' noise in aero-engine inlet ducts. *Journal of Sound and Vibration*, 248(1):123–149, 2001. Inst. of Sound and Vibration Res. University of Southampton, Southampton SO17 1BJ, United Kingdom 0022-460X JA 15 Refs. English.

[43] C. L. Morfey. Sound transmission and generation in ducts with flow. *J Sound Vibr*, 14(1):37–55, 1971. 22 Refs.

[44] C. L. Morfey and M. J. Fisher. Shock-wave radiation from supersonic ducted rotor. *Aeron J*, 74(715):579–85, 1970. 10 Refs.

[45] P.A. Nelson and S.J. Elliott. *Active Control of Sound.* London: Academic Press, 1992.

[46] P.A. Nelson and S.H. Yoon. Estimation of acoustic source strength by inverse methods: Part I: Conditioning of the inverse problem. Technical report, ISVR, 1998.

[47] A.N. Norris and I.C. Sheng. Acoustic radiation from a circular pipe with an infinite flange. *Journal of Sound and Vibration*, 135(1), 1989.

[48] M. G. Philpot. Buzz-saw noise generated by a high duty transonic compressor. Journal ref: ASME Pap, , (1970) May 24-28 1970 8 Refs.

[49] Gordon F Pickett. Prediction of the spectral content of combination tone noise. *Journal of Aircraft*, 9(9):658–663, 1972.

[50] C Pitelet. *Flow Control For Fan Noise Reduction.* PhD thesis, University of Southampton.

[51] E.R. Rademaker, P Sijtsma, and B.J. Tester. Mode detection with an optimised array in a model turbofan engine intake at varying shaft speeds. In *7th AIAA/CEAS Aeroacoustics Conference*, Maastricht, Netherlands, 2001. AIAA.

[52] J.D. Risi, R. A. Burdisso, and C. R. Fuller. Analytical investigation of active control of radiated inlet fan noise. *Journal of the Acoustical Society of America*, 99(1):408–416, 1996.

[53] J.C. Simonich. A review of actuators for active noise control in gas turbines. In *AIAA/CEAS Aeroacoustics Conference*, Munich, 1995. AIAA.

[54] J.P. Smith and R. A. Burdisso. Active control of inlet noise from a turbofan engine using inlet wavenumber sensors. In *5th AIAA/CEAS Aeroacoustics Conference*, Seattle, 1999. AIAA.

[55] J.P. Smith, R. A. Burdisso, and C. R. Fuller. Experiments on the active control of inlet noise from a turbofan jet engine using multiple circumferential control arrays. In *2nd AIAA/CEAS Aeroacoustics conference*, State College, PA, 1996.

[56] S.D. Snyder and C.H. Hansen. The effect of transfer function estimation errors on the filtered-x lms algorithm. *IEEE Transactions on Signal Processing*, 42(4):950–953, 1994.

[57] S.W.Rienstra and A Hirschberg. *An Introduction to Acoustics.* unpublished, 2002.

[58] R. H. Thomas, R. A. Burdisso, C. R. Fuller, and W. F. O'Brien. Preliminary experiments on active control of fan noise from a turbofan engine. *Journal of Sound and Vibration*, 161(3):532–537, 1993. Virginia Polytechnic Inst and State Univ, Blacksburg, VA, USA 0022-460X JA 8 Refs. English.

[59] P.G. Vaidya. Multiple pure tone generation in aeroengine fans at subsonic and supersonic relative tip speeds. *AIAA Journal*, 22(10):1366–1374, 1984.

[60] Bruce Walker. Sensitivity issues in active control of circular duct modes using axially-spaced actuator arrays. *Noise Control Engineering Journal*, 49(1):6–14, 2001.

[61] K.S. Wang and T.C. Tszeng. Propagation and radiation of sound in a finite length duct. *Journal of Sound and Vibration*, 93(1):57–79, 1984.

[62] Anthony C. Zander and Colin H. Hansen. A comparison of error strategies for the active control of duct noise. *Journal of the Acoustical Society of America*, 94(2):841–848, 1993.

[63] William E Zorumski. Generalized radiation impedances and reflection coefficients of circular and annular ducts. *Journal of the Acoustical Society of America*, 54(6):1667–1673, 1973.